Motion Correction and Pharmacokinetic Analysis in Dynamic Positron Emission Tomography

by

Hassan Mohy-ud-Din

A thesis submitted to The Johns Hopkins University in conformity with the requirements for the degree of Doctor of Philosophy.

Baltimore, Maryland

February, 2015

Abstract

This thesis will focus on two important aspects of dynamic Positron Emission Tomography (PET): (i) Motion-compensation , and (ii) Pharmacokinetic analysis (also called parametric imaging) of dynamic PET images. Both are required to enable fully quantitative PET imaging which is increasingly finding applications in the clinic.

Motion-compensation in Dynamic Brain PET Imaging: Dynamic PET images are degraded by inter-frame and intra-frame motion artifacts that can affect the quantitative and qualitative analysis of acquired PET data. We propose a Generalized Inter-frame and Intra-frame Motion Correction (GIIMC) algorithm that unifies in one framework the inter-frame motion correction capability of Multiple Acquisition Frames and the intra-frame motion correction feature of (MLEM)-type deconvolution methods. GIIMC employs a fairly simple but new approach of using time-weighted average of attenuation sinograms to reconstruct dynamic frames. Extensive validation studies show that GIIMC algorithm outperforms conventional techniques producing images with superior quality and quantitative accuracy.

Parametric Myocardial Perfusion PET Imaging: We propose a novel frame-

ABSTRACT

work of robust kinetic parameter estimation applied to absolute flow quantification in dynamic PET imaging. Kinetic parameter estimation is formulated as nonlinear least squares with spatial constraints problem where the spatial constraints are computed from a physiologically driven clustering of dynamic images, and used to reduce noise contamination. The proposed framework is shown to improve the quantitative accuracy of Myocardial Perfusion (MP) PET imaging, and in turn, has the long-term potential to enhance capabilities of MP PET in the detection, staging and management of coronary artery disease.

Thesis Committee

Dr. Arman Rahmim,

Departments of Electrical and Computer Engineering and Radiology (primary reader)

Dr. John Goutsias,

Department of Electrical and Computer Engineering (secondary reader)

Dr. Howard Weinert,

Department of Electrical and Computer Engineering

Dr. Sridevi Sarma,

Department of Biomedical Engineering

Dr. Amy Foster,

Department of Electrical and Computer Engineering

Acknowledgments

I would like to thank Almighty Allah (God) for all the blessings, making me worthy to achieve whatever little I could and to His beloved Prophet Hazrat Muhammad (PBUH) who has been sent as a mercy to all the worlds.

I would like to thank my PhD supervisor and mentor Professor Arman Rahmim for showing faith in me and providing the space and freedom to explore ideas and opportunities that inspired me during my research study. He always encouraged my participation in various conferences, seminars and summer schools during my stay at Hopkins. We always had the most fascinating discussions on stimulating topics in the field of Positron Emission Tomography and Molecular Imaging. I would like to thank Professor Johns Goutsias and Professor Howard Weinert for being an integral part of my qualifying exam committee, graduate board oral exam committee, and thesis defense committee. Professor Goutsias taught an influential course on Image Processing and Analysis and Professor Weinert taught an important course on Filtering and Smoothing. I also had the privilege of assisting Professor Goutsias in Image Processing and Analysis for three successive years. I also conducted one

credit hour course on Digital Signal Processing for MATLAB under the supervision for Professor Weinert for three successive years. I would like to thank Professor Amy Foster for being a part of my thesis committee. She has been an amazing person to interact with and has always appreciated my work and presentation.

I would like to acknowledge pivotal contributions of Professor Pablo Iglesias and Professor Sridevi Sarma. Professor Iglesias has shown tremendous faith in me and advocated me in department meetings. Professor Sarma has been a constant source of guidance. Every advice shared from day one has been extremely useful and gave me a sense of perspective and focus. She also taught an interesting course on Dynamical Systems; an intensive course made simpler and exciting. She was also a member of my graduate board oral exam committee. I hope to have lived up to there expectations.

I would like to thank Professor Martin Lodge, Professor Dean F. Wong, Professor Richard L. Wahl, Professor Thomas Schindler, Professor Yun Zhou, Professor Susan Resnick, and Dr. Abdel Tahari for being wonderful collaborators on various research projects. Professor Lodge chaired my graduate board oral exam and has deep insights in clinical aspects of emission tomography. I would like to thank Professor Benjamin Tsui, Professor Eric Frey, and Professor Ken Taguchi for conducting an informative journal club at the Division of Medical Imaging Physics and Professor Rene Vidal for conducting an extremely engaging seminar series at the Center of Imaging Science.

I would like to thank Professor Daniel Robinson for supervising my thesis on *Minimizing Nonconvex Quadratic Functions Subject to Bound Constraints* at the De-

partment of Applied Mathematics and Statistics and serving on my graduate board oral exam committee. He also accepted my suggestion to conduct a weekly journal club where we would discuss selected papers. The whole process of research and collaboration was extremely fruitful and engaging. He has always been patient, helpful, and cooperative. I would like to thank him for all the guidance and support extended to me.

I would like to thank Professor Laurent Younes for giving me an opportunity to instruct an intersession course on MATLAB at the Department of Applied Mathematics and Statistics. I would also like to thank Professor Dennice Gayme for giving me an opportunity to assist her in the course on Energy System Analysis at the Department of Mechanical Engineering.

I would like to thank residents-come-friends at the Johns Hopkins Hospital: Dr Elcin Zan, Dr. Riham El-Khouli, Dr Esther Mena Gonzales, and Dr. Abdel Qadir for teaching me how to read clinical images on state-of-the-art softwares. I am extremely grateful for a fruitful friendship and collaboration provided by Dr. Anil Mathur, Dr. Jennifer Coughlin, Dr. Jim Brasic, Dr. Olivier Roussett, Andy Crabb, Corina Voicu, Heather Valentine, Rebecca Pilgrim, Jean Reyes, and Alexis at the Department of Radiology and Radiological Sciences.

I am extremely grateful to Debbie Race, Barbara Sullivan, Janel Johnson, and Felicia Roane at the Department of Electrical and Computer Engineering, Tammy Thompson and Christine LaPonzina at the Department of Radiology, and Kristin

ACKNOWLEDGMENTS

Bechtel at the Department of Applied Mathematics and Statistics for being the go-to people in all situations at all times. Tammy and Christine has been my mentors and guide in innumerable situations. They are always welcoming and full of happiness and joy. Debbie, Barbara, and Kristin have been a steady support since I joined Hopkins. Every now and then, I have pestered them with questions and issues and they always have been patient listeners and solution providers.

I would like to thank JHU Admin, Blue Jay Shuttle, and JHU Tax Office for making every difficult situation easier and seamless. I am extremely grateful to the Department of Electrical and Computer Engineering for bestowing me with a PhD fellowship that allowed me to become a part of Johns Hopkins University and pursue my interests.

I would like thank Dr. Asadullah who has been a source of constant support during my stay in USA, Professor Abubakr Muhammad and Professor Sabieh Anwar at the LUMS School of Science and Engineering, and Dr. Sabahat Zahra Siddiqui at the Government College University Lahore for there fruitful advice and mentorship. I always consult them in almost every matter of academic and personal life.

Finally, I would to thank my friends and colleagues I met during my graudate studies. I call them *The* 100 (without ranking, Figure 0.1).

Figure 0.1: *The* 100: friends and colleagues I met during my graduate studies.

Dedication

I have always believed that the biggest seat of learning is home. I owe almost everything to my family. My parents, Mr. Abdul Hafeez Siddiqui and Ms. Saleema Hafeez, and my sisters, Ms. Aroosa Kiran Fatima, Ms. Zeenat Ayesha Adnan, and Dr. Sabahat Zahra Siddiqui for being a great source of energy and joy. They managed to provide an intellectual environment which was multi-dimensional. I developed a penchant for poetry, philosophy, theology, sports, music and literature. Nature was more stimulating then technology. Family relationships made me realize that whatever I do effects everyone. It infused confidence, self-control and simplicity. I learned the power of words and speech which enticed me to pursue a career in academics and research. I was advised to be steady in tough times and be grounded in prosperity. I was taught to be vulnerable and robust. The constitution was based on ethics, virtue, and morality. Thank You so much for everything. A little token for your life's investment.

Contents

List of Tables

List of Figures

Chapter 1

Introduction

Nature has inspired numerous groundbreaking discoveries in mathematics and applied sciences. Isaac Newton observed the falling apple (Figure 1.1 (a)) which motivated him to discover and establish the foundations of gravity. The Wright brothers studied the aerodynamics of birds to make fix winged powered flight plausible (Figure 1.1 (b)). Likewise, objects casting shadows is a universally observed and understood phenomenon (Figure 1.1 (c)) that has inspired several landmark scientific discoveries. This simple observation i.e. *every 3-D object*[1] *casts a shadow in a low dimensional space* raises the following deep and interesting question:

[**Inverse Problem: Shape Reconstruction**]

Can we reconstruct 3-D shapes from shadows?

[1] in this thesis we focus on objects in $\mathbb{R}^3$

Figure 1.1: (a) Isaac Newton contemplating about gravitational force, (b) Wright brothers fanciful flying in the air, and (c) flock of birds casting shadows on the ground. Images taken from www.google.com.

A general answer to this question is *Yes*. Aristotle was, perhaps, the first one to use this insight to conclude that the Earth is spherical in shape. He carefully studied lunar eclipse which occurs when the Sun, the Earth, and the Moon are almost collinear with the Earth in the middle (Figure 1.2). He observed that the shadow of the Earth on the Moon is always a circular arc which can only happen if the Earth is spherical in shape. This was a powerful indirect reasoning to conclude about the shape of the Earth from its shadows.

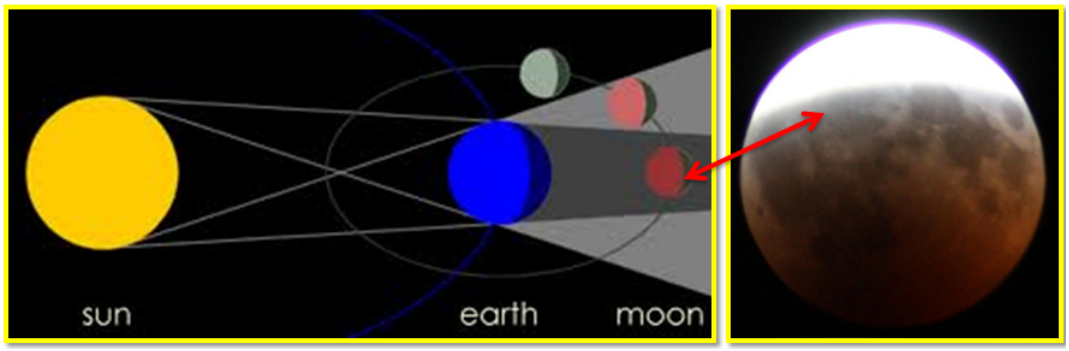

Figure 1.2: Lunar eclipse. Image taken from www.google.com. An interesting talk by Terence Tao on the *Cosmic Distance Ladder*[2] also expounds on this insight.

[2] http://terrytao.wordpress.com/2010/10/10/the-cosmic-distance-ladder-ver-4-1/

Figure 1.3 shows a simple setup to acquire shadows of an object from multiple views. A 3-D object is placed over a turntable and illuminated from one side by a light source. The object occludes the light rays and in the process casts a shadow on a translucent panel. The shadow image is recorded by a camera placed on the opposite side of the light source. As the turntable rotates, shadows of the objects from multiple views are collected. The collected set of 2-D shadows are used to reconstruct the 3-D shape of the object by a technique called *Shadow Carving* [1, 2].

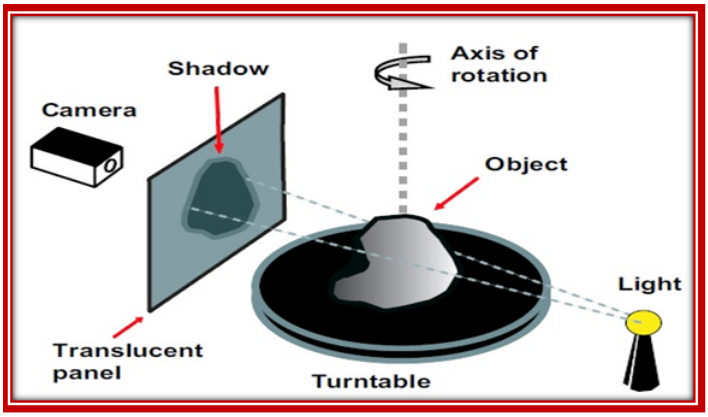

Figure 1.3: Reconstruction of 3-D shapes from silhouettes [1].

With a feasible approach to reconstruct shapes from shadows, a logical extension would be to ask the following question:

[**Inverse Problem: Tomography**]

Can we image/visualize the inner structure of a 3-D object without physically slicing it?

The most complex known object in the world is the human body and we are

interested in imaging the internal structure (organs) of the human body. We cannot proceed with the previous approach as shadows only carry information about the outer structure of the object. To answer the previous question in the affirmative, we need penetrating light (e.g. in optical imaging [3]), sound (e.g. ultrasound imaging [4]) or matter (e.g. emission tomography [5]) to capture the internal structures of the object. Figure 1.4 shows an experimental setup to acquire multiview projection data using (penetrating) X-rays. A collimated X-ray source emits parallel X-rays that are attenuated as they penetrate the internal structures of the object (e.g. Shepp-Logan phantom [6]) before being detected by an array of detectors at the opposite end. The intensity profile recorded by the array of detectors is called a *projection profile*, $P(r, \theta)$, which is a function of detector position, r, and projection angle, θ.

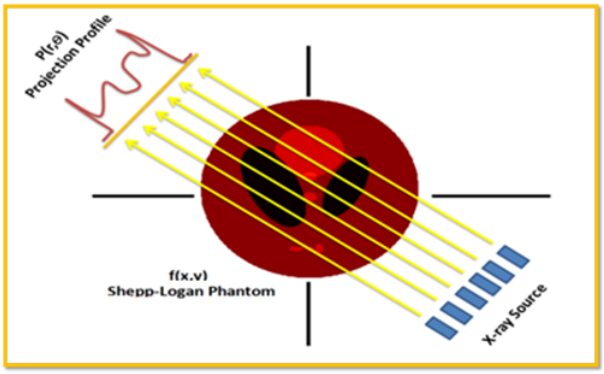

Figure 1.4: Tomographic reconstruction experimental setup [7]. The mathematical object being imaged is a Shepp-Logan phantom [6] which contains ellipses of different sizes and intensities mimicking internal structures (organs) of a human body. Source-detector pairs are rotated to collect multiview projection data.

The physics of the process is described by the Beer-Lambert law [8]:

$$\begin{aligned} I &= I_0 e^{-\int \mu(x,y)dy} \\ -\ln \frac{I}{I_0} &= \int \mu(x,y)dy \end{aligned} \tag{1.1}$$

where I_0 is the incident intensity of X-ray source, I is the detected (attenuated) intensity of X-rays, and $\mu(x,y)$ is the 2-D attenuation distribution of the object under study[3]. $\mu(x,y)$ encodes all information about the internal structures of the object and needs to be estimated from the projection data. Hence, the problem can be mathematically stated as follows:

[**Inverse Problem: Tomographic Reconstruction**]

Solve the following integral equation for $\mu(x,y)$:

$$P(r,\theta) = \int_{-\infty}^{\infty}\int_{-\infty}^{\infty} \mu(x,y)\delta(x\cos\theta + y\sin\theta - r)\,dx\,dy \tag{1.2}$$

where $\{P(r,\theta)\}$ is the multiview projection data for $\theta \in [0, 2\pi)$.

The R.H.S of equation 1.2 is called the Radon transform [9] of $\mu(x,y)$ i.e. $\mathcal{R}\{\mu(x,y)\} = \int_{-\infty}^{\infty}\int_{-\infty}^{\infty} \mu(x,y)\delta(x\cos\theta + y\sin\theta - r)\,dx\,dy$. Radon transform collects line integrals (or projection data) at multiple views of the underlying object where the line is described by $r = x\cos\theta + y\sin\theta$. For the forward model, the discretized Radon

[3] generalizations to 3-D attenuation distribution is pretty straightforward

transform is called the *forward projection operator* and for the inverse model, the adjoint of the discretized Radon transform is also called the *backprojection operator*. The forward projection operator generates projection data and the backprojection operator reconstructs the object from the projection data. Projection data is stacked in a 2-D matrix called *sinogram* where the columns index the projection angles or views (i.e. θ) and the rows index the detector position (i.e. r). Figure 1.5 shows a small program to simulate tomographic reconstruction in MATLAB. Figure 1.6 shows original phantom image, noise-free sinogram, and the reconstructed image obtained from the MATLAB code.

```
>> % Define a phantom
>> I = phantom('Modified Shepp-Logan',256);
>> % Generate projection data
>> theta = 0:180;
>> P = radon(I,theta);
>> % Reconstruct using backprojection
>> Irecon = iradon(P,theta);
>> % Generate backprojection movie
>> h = figure(1);
>> aviobj = avifile('bkproj.avi','compression','None');
>> for k = 2:numel(theta)
       Irecon = iradon(P(:,1:k),theta(1:k));
       imshow(Irecon,[]); axis('off'); colorbar;
       F = getframe(h);
       aviobj = addframe(aviobj,F);
   end
>> close(h);
>> aviobj = close(aviobj);
```

Figure 1.5: MATLAB code for 2-D image reconstruction from projection data.

Problem 1.2 is ill-posed in the sense of Hadamard[4] [10, 11] if the multiview projection data set is noisy and incomplete which is usually the case in reality.

[4] A problem is *well-posed* if (1) the solution exists, (2) the solution is unique, and (3) the solution continuously depends on data. Problems that are not well-posed in the sense of Hadamard are ill-posed. Inverse problems are usually ill-posed.

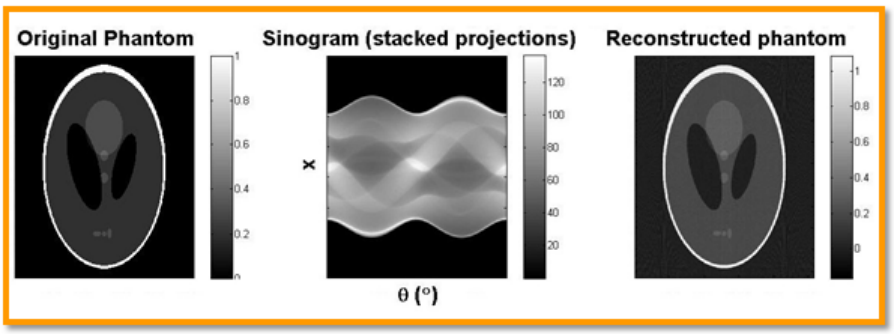

Figure 1.6: *(Left)* Original image of Shepp-Logan phantom, *(Middle)* Noise-free sinogram, and *(Right)* Reconstructed image from 2-D sinograms

3-D reconstruction of objects from 2-D multiview projection data finds numerous applications in various disciplines e.g. medical imaging [12–14], computer vision [15], shape theory [16], pure and applied mathematics (solution of hyperbolic PDEs, reconstruction of functions from integrals e.g. Minkowski-Funk) [17–19], radar imaging (SAR image reconstruction, reflection seismology) [20], and many more.

1.1 Imaging Modalities

In a human body, we are interested in studying the structural or morphological aspects of the organs of interests and/or the functional or biochemical processes taking place inside the organs of interest. For structural or morphological imaging, the primary imaging modalities are computed tomography (CT), magnetic resonance imaging (MRI), and ultrasound, and for functional or molecular imaging, the primary imaging modalities are positron emission tomography (PET), single photon emission tomography (SPECT), optical imaging, and functional magnetic resonance imaging (fMRI). Figure 1.7 shows a pictorial representation of these imaging modalities.

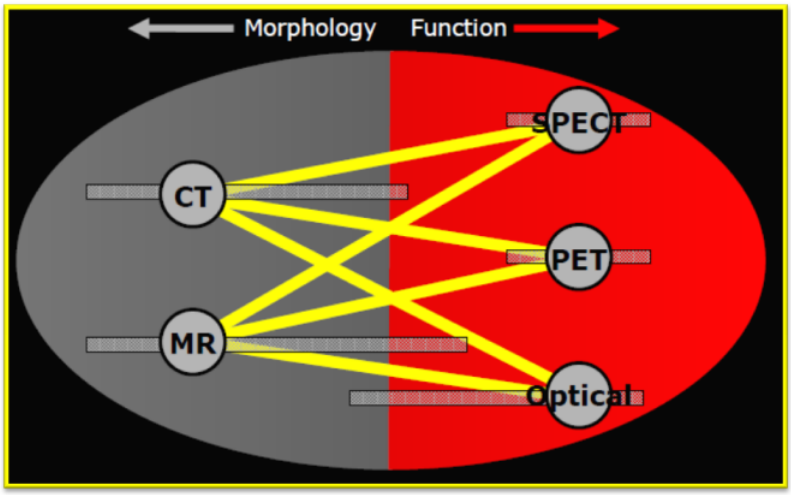

Figure 1.7: Morphological and functional imaging modalities. Image is borrowed from Jeff Siewerdsen's talk on *Multi-Modality Imaging: Technologies, Applications, and Future Directions*[5]. Yellow bars show the combinations of anato-functional imaging modalities for multi-modality imaging e.g. PET-CT, PET-MR, SPECT-MR etc.

In this thesis, we are primarily interested in functional imaging via positron emission tomography (PET). However, for accurate tomographic reconstruction of functional images, correction for attenuation due to anatomical structures has to be made. In this respect, tomographic imaging can be subdivided into two broad classes: (1) transmission tomography [21], and (2) emission tomography [5]. In transmission tomography (e.g. CT), the transmission source emits low energy X-rays that penetrate the object of interest getting attenuated by anatomical structures with varying attenuation coefficients, $\mu(x, y)$, along the way. The attenuated X-rays are ultimately recorded by a detector array placed diametrically opposite to the source array. The source-detector array is rotated around the object to collect multiview projection data. The transmission or attenuation image is estimated from the multiview projec-

[5] http://www.aapm.org/meetings/amos2/pdf/35-9794-56056-401.pdf

tion data set by solving discretized version of Problem 1.2.

In emission tomography (e.g. PET, expounded in Section 1.2), a radionuclide is injected into the blood stream and it redistributes itself in the body depending on the molecular process under study. The unstable radionuclide disintegrates by emitting γ-rays which are recorded by a detector array surrounding the object of interest. Functional image is also reconstructed from the collected multiview projection data set by solving the discretized version of Problem 1.2 ($\mu(x, y)$ is replaced by $f(x, y)$). Figure 1.8 summarizes the differences between transmission and emission tomography.

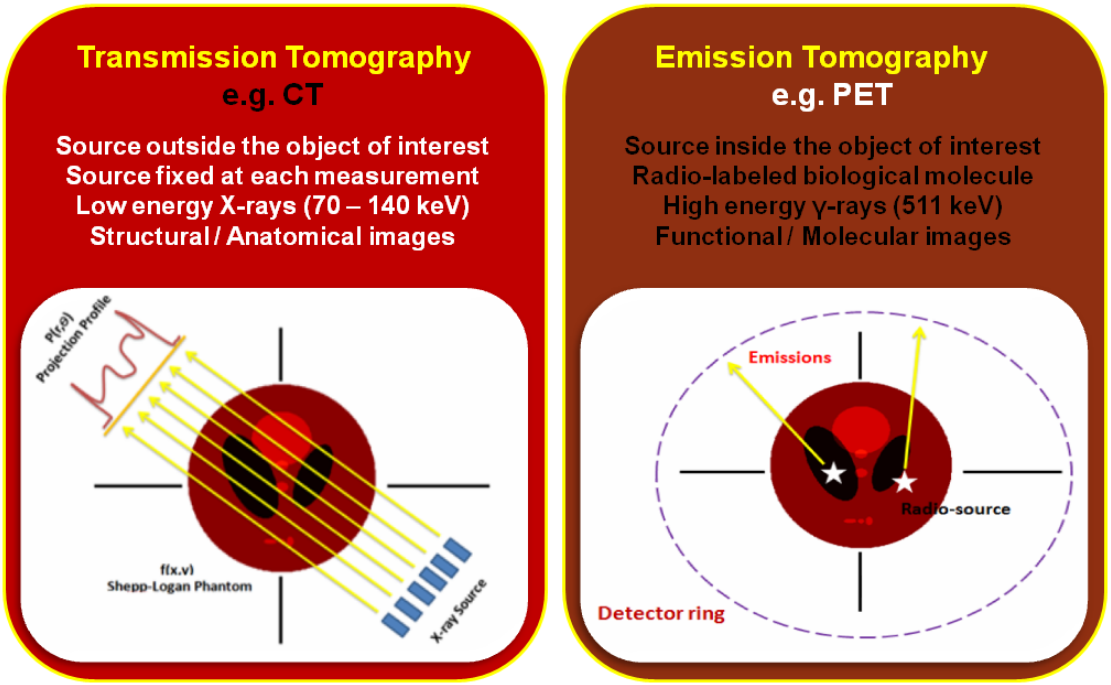

Figure 1.8: Comparison of transmission vs emission tomography

1.2 Positron Emission Tomography

Positron Emission Tomography has emerged as a powerful non-invasive imaging technique enabling in vivo measurements of neurochemistry and physiology [22]. In this section we will first motivate the need of having an imaging modality like PET in Section 1.2.1. This is followed by a basic description of the PET process in Section 1.2.2 and PET image reconstruction in Section 1.2.3. We elaborate on the image degradation factors in Section 1.2.4 and conclude this section with clinical applications of PET imaging in Section 1.2.6. Our exposition will be at a basic level and direct the interested readers to references [5, 8, 23, 24] for in-depth reading on various instrumentation and image generation, reconstruction, and quantification aspects of PET imaging. Another interesting resource is a video talk by Dr. Osama Mawlawi on the *Fundamentals of Positron Emission Tomography*[6].

1.2.1 Motivation

The goal is to image and study the functional or biochemical processes of various organs of interest. Functional processes of interest include blood flow, glucose metabolism, receptor density etc [25–34]. A promising approach involves injection of radiolabeled compounds with site specific uptake in the blood stream followed by tracking the compound as it traverses through the biological pathway and gets distributed in the target region. Positron emission tomography, as the name suggests,

[6] http://hstalks.com/main/view_talk.php?t=1877&c=252

uses positron emitters to label site specific compounds. The advantage of PET over other functional imaging modalities is that many positron emitters like ^{11}C, ^{18}F, ^{13}N, ^{15}O occur naturally in biological molecules. Hence, depending on the molecular process under study (e.g. blood flow), a biological molecule is labeled with a radioactive isotope as shown below:

[**Radiolabeling of Biological Molecule**]

$$\underbrace{H_2O^{16}}_{\text{Biological Molecule}} \xrightarrow[\text{for blood flow}]{\text{Radiolabeling}} \underbrace{H_2O^{15}}_{\text{Radiolabeled Molecule}} \tag{1.3}$$

Compared to biological compounds, positron emitters have smaller molecular weights. Moreover, radiolabeled compounds are administered in smaller quantities (i.e. tracer amounts[7]) without impacting the chemical behavior of the biological molecules in the body. Table 1.1 lists positron emitting radiopharmaceuticals and their biomedical applications.

1.2.2 The PET Process

Figure 1.9 shows a simplistic diagram of the PET process. The radiotracer is intravenously injected into the blood stream and is redistributed in the patient body based on its biochemical fate. The unstable radionuclide decays to a stable energy state by

[7] hence, radiolabeled compounds are also called radiotracers.
[8] reproduced from [24].

Table 1.1: Biomedical applications of positron emitting radiopharmaceuticals[8].

radiotracer	Radiopharmaceutical	Examples of Biomedical Applications
^{15}O	oxygen	oxygen metabolism
^{15}O	carbon monoxide	blood volume
^{15}O	carbon dioxide	blood flow
^{15}O	water	blood flow
^{13}N	ammonia	blood flow
^{18}F	FDG	glucose metabolism
^{18}F	FDOPA	pre-synaptic dopaminergic activity
^{18}F	FMISO	hypoxic cell tracer
^{11}C	DTBZ	vesicular monoamine transporter VMAT2
^{11}C	raclopride	dopamine D2 receptor
^{11}C	methylphenidate (MP)	dopamine membrane transporter DAT
^{11}C	SCH23390	dopamine D1 receptor
^{11}C	flumazenil	benzodiazepine receptor

proton decay which is governed by the following equation:

$$p^+ \rightarrow n + \beta^+ + \nu \tag{1.4}$$

where p^+ is a proton, n is a neutron, β^+ is a positron, and ν is neutrino. For a general radionuclide, X, the proton decay process can be described as follows:

$${}^{M}_{Z}X \rightarrow {}^{M}_{Z-1}X + \beta^+ + \nu \tag{1.5}$$

where M is the total number of protons and neutrons, and Z is the number of protons. Positrons are emitted with a continuous spectrum of energies and Table 1.2 lists the maximum energy in MeV of commonly used positron emitting radiotracers.

[9] reproduced from [24].

Table 1.2: Properties of commonly used radiotracers in PET Imaging[9].

radiotracer	$T_{\frac{1}{2}}$ (min)	E_{max} (MeV)	Positron range in Water (mm)
^{18}F	109.8	0.64	1.0
^{11}C	20.3	0.96	1.1
^{13}N	9.97	1.19	1.4
^{15}O	2.03	1.70	1.5
^{68}Ga	67.8	1.89	1.7
^{82}Rb	1.26	3.15	2.7

The emitted positrons loose their kinetic energy via Coulomb interactions with electrons while propagating through the surrounding medium before reaching thermal energy levels. When positrons reach thermal energy levels they annihilate with an electron transferring their mass into energy which appears as two *almost* anti-parallel γ-rays of 511 keV each. The emitted γ photons are detected by a detector ring surrounding the patient body. Since the γ photons are isotropically emitted, projection data is simultaneously collected from multiple projection views and stored as a sinogram[10].

1.2.3 PET Image Reconstruction

Images of activity distribution are reconstructed from projection data by solving the discretized version of Problem 1.2. Image reconstruction algorithms can be classified into two categories: (1) analytical reconstruction methods [5, Chapter 20], [24, Chapter 2], and (2) statistical reconstruction methods [5, Chapter 21], [24, Chapter $2-4$].

[10] projection data can also be saved in a list-mode format. We direct the reader to reference [24, Chapter 1] for further reading.

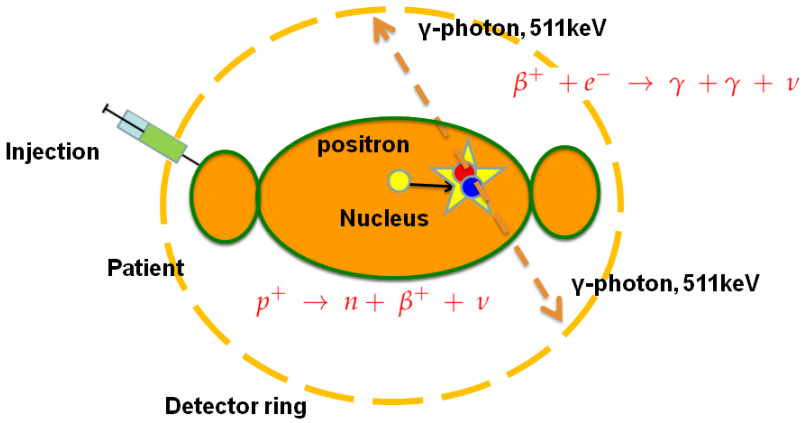

Figure 1.9: PET data acquisition process

In this thesis, we focus on statistical reconstruction methods which have demonstrated superior performance over analytical methods. Statistical methods allow accurate modeling of statistical noise, complex detector geometries, and the detection process to correct for image degrading effects (Section 1.2.4) [35, 36]. We next elaborate on the mathematics of image reconstruction in PET.

Let Y_i $(i = \{1, \cdots, M\})$ denote the elements of the sinogram matrix (projection data) where M is the number of sinogram bins. $\{Y_i\}_{i=1}^{M}$ are well-modeled as independent Poisson random variables:

$$Y_i \sim \text{Poisson}\{\overline{y_i}\} \tag{1.6}$$

Let $\mathbf{y} = [y_1 \quad y_2 \quad \cdots \quad y_M]^T$ and $\overline{\mathbf{y}} = [\overline{y}_1 \quad \overline{y}_2 \quad \cdots \quad \overline{y}_M]^T$ denote column vectors of measured counts and expected counts. Expected counts are related to the unknown

activity distribution, $\mathbf{x} \in \mathbb{R}^N$, by an affine transform:

$$\overline{\mathbf{y}} = \mathbf{P}\mathbf{x} + \mathbf{r} \tag{1.7}$$

where $\mathbf{P} \in \mathbb{R}^{M \times N}$ is the detection probability matrix (or forward projection operator, Page 5) with the (i, j) element equal to the probability of detecting an event from the j^{th} voxel at the i^{th} detector pair, and $r \in \mathbb{R}^M$ is the contribution of scatter and random events (Section 1.2.4.2, 1.2.4.3) in the projection data. The log-likelihood function for the Poisson distributed projection data can be written as follows:

$$L(\mathbf{y}|\mathbf{x}) = \sum_{i=1}^{M} y_i \log \overline{y}_i - \log \overline{y}_i - \log y_i! \tag{1.8}$$

The image reconstruction task can now be framed as an optimization problem which is solved using the maximum likelihood expectation maximization algorithm (MLEM [37, 38]). MLEM algorithm has proven convergence properties, and easily incorporates non-negativity constraints in the sense that if the initial estimate is non-negative, image estimates at every iteration are non-negative.

[**Inverse Problem: Maximum Likelihood Estimate**]

$$\hat{\mathbf{x}} = \underset{\mathbf{x} \geq 0}{\operatorname{argmax}}\, L(\mathbf{y}|\mathbf{x}) \tag{1.9}$$

$$\mathbf{x}^{n+1} = \frac{\mathbf{x}^n}{\mathbf{P}^T \mathbf{1}_M} \mathbf{P}^T \frac{\mathbf{y}}{\mathbf{P}\mathbf{x}^n} \tag{1.10}$$

where $\mathbf{x}^n$ is the image estimate at the n^{th} iteration, $\mathbf{P}^T$ is the backprojection operator (Page 5), and $\mathbf{1}_M$ is a column vector of ones.

An accelerated version of MLEM, called the ordinary subset expected maximization algorithm (OSEM [39]), uses subsets of projection data to iteratively update the estimated image. The speed-up factor is equal to the number of subsets used in the block-iterative updates. Unlike MLEM algorithm, the OSEM algorithm is not necessarily convergent, though convergent variation of it has been proposed [40–44].

Since the tomographic reconstruction problem is ill-posed, ML estimates are extremely noisy and need to be regularized to obtain more meaningful estimates of activity distribution [45, 46]. Instead of maximizing the log-likelihood function, one maximizes the penalized log-likelihood function, $\Phi(\mathbf{x})$ (1.11), where $R(\mathbf{x})$ is a penalty function that encourages smooth solutions (e.g. quadratic penalty) and β is the tuning parameter that controls the resolution-noise properties of image estimates [45, 47–49]. The penalty function may be obtained by taking the logarithm of the *a priori* distribution on the estimated image i.e $p(x) = \frac{1}{Z}e^{-\beta R(x)}$, where Z is a normalizing constant. In this case, the penalized log-likelihood estimate is also called *maximum a posteriori estimate* (MAP) [50–54]. The penalized log-likelihood function is optimized using *one-step late* (OSL) algorithm [55, 56].

[**Inverse Problem: Penalized Maximum Likelihood Estimate**]

$$\hat{\mathbf{x}} = \underset{\mathbf{x}\geq 0}{\operatorname{argmax}}\, \Phi(\mathbf{x}) \triangleq L(\mathbf{y}|\mathbf{x}) - \beta R(\mathbf{x}) \tag{1.11}$$

$$\mathbf{x}^{n+1} = \frac{\mathbf{x}^n}{\mathbf{P}^T\mathbf{1}_M - \beta\nabla_{\mathbf{x}} R(\mathbf{x})|_{\mathbf{x}=\mathbf{x}^n}}\mathbf{P}^T\frac{\mathbf{y}}{\mathbf{P}\mathbf{x}^n} \tag{1.12}$$

In equation 1.7, the system matrix is the detection probability matrix $\mathbf{P}$. However, as mentioned before, statistical reconstruction methods allow modeling of physical degradation factors (discussed Section 1.2.4) in the reconstruction framework. The system matrix can be factorized as follows [57]:

$$\mathbf{P} = \mathbf{P}_{\text{det. sens.}}\mathbf{P}_{\text{det. blur.}}\mathbf{P}_{\text{attn.}}\mathbf{P}_{\text{geom.}}\mathbf{P}_{\text{pos. range.}} \tag{1.13}$$

where $\mathbf{P}_{\text{pos. range.}}$ models positron range blurring in the image space, $\mathbf{P}_{\text{geom.}}$ is the detection probability matrix, $\mathbf{P}_{\text{attn.}}$ is a diagonal matrix of attenuation correction factors, $\mathbf{P}_{\text{det. blur.}}$ models detector blurring in the sinogram space, and $\mathbf{P}_{\text{det. sens.}}$ is a diagonal matrix containing normalization factors. We describe these various degradation factors next.

1.2.4 Degradation Factors in PET

Several physical factors can degrade the qualitative and quantitative accuracy of PET images. Appropriate correction methods can be adopted for each one of them

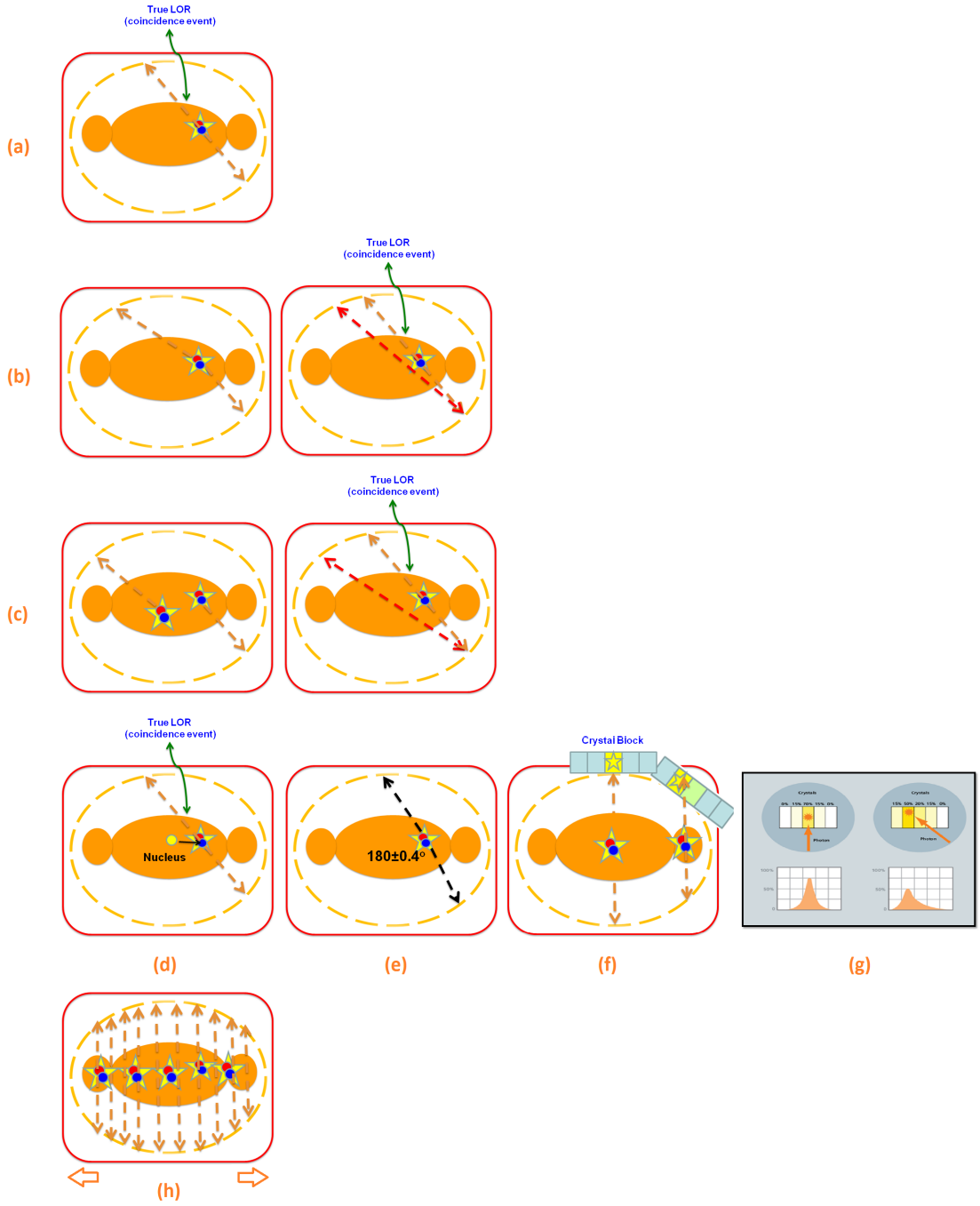

Figure 1.10: Degradation factors in PET: (a) true LOR (coincidence event), (b) mispositioned LOR due to scatter (red arrow), (c) mispositioned LOR due to random (red arrow), (d) positron range, (e) photon non-collinearity, (f) depth of interaction, (g) detector response function, and (h) geometric correction

to ensure an accurate reconstruction of the underlying radiotracer distribution in the organ of interest. Before we list the degradation factors, we need to have a clear understanding of what constitutes a *true event* (also called *true coincidence*).

As mentioned in Section 1.2.2, a positron annihilates with an electron producing two anti-parallel γ photons. In a degradation free system, these photons will travel in straight lines before being detected at the detector ring. To localize the annihilation event along this *line of response* (LOR), γ photons must be detected in *coincidence* which implies that the arrival times of the photons fall within a *coincidence time window* ($6-12$ ns). An annihilation event detected within a coincidence time window is called a true event or true coincidence. Figure 1.10 (a) shows a true LOR. Now we are able to discuss various degradation factors in PET.

1.2.4.1 Attenuation

γ photons interact with matter while traveling through the medium. Interactions are primarily of two types: (1) photoelectric absorption, and (2) Compton scattering. Photoelectric absorption is the dominant photon-matter interaction in human tissues for photon energies below 100 keV, whereas, Compton scattering is dominant for photon energies between 100 keV and 2 MeV [58, 59]. Compton scattering is the main source of photon-matter interaction in PET and the probability of occurrence of a Compton effect is given by the Klein-Nishina equation [60].

Compton scattering occurs when a γ photon interacts with a valence shell electron.

The photon looses part of its kinetic energy to the loosely bound electron and is scattered at an angle away from the "true" LOR as shown in Figure 1.11. The energy of the scattered photon is given by the following equation:

$$E_{sc} = \frac{E_0}{1 + \frac{E_0}{0.511}(1 - \cos\theta)} \tag{1.14}$$

where E_0 is the energy of the γ photon before interaction and θ is the scattering angle.

Compton effect may result in a γ photon being scattered out of the field of view (FOV) or be detected at another detector outside the coincidence time window. Either of these cases results in a loss of LOR, a phenomenon termed as attenuation.

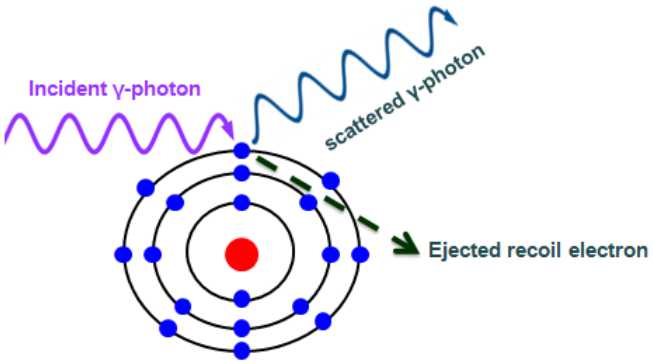

Figure 1.11: Compton scattering of γ photon.

Attenuation effects needs to be incorporated in the image reconstruction process to avoid under-estimation of the radiotracer distribution. Attenuation factor (AF) is computed from the survival probability of a photon which is defined as the probability that a photon propagates through an attenuating medium (with attenuation

coefficient μ) without interacting with matter.

$$AF = e^{-\mu d} \tag{1.15}$$

In PET, a photon pair needs to be detected in coincidence to be counted as a true event. Hence, AF is a product of the survival probabilities of the photons being detected by a detector pair.

$$AF_{PET} = e^{-\mu d} e^{-\mu(D-d)} = e^{-\mu D} \tag{1.16}$$

where D is the distance between the two detector's surfaces. Therefore, AF in PET is independent of the spatial position of the annihilation event which makes attenuation correction straightforward compared to SPECT imaging which has depth dependent AF. AF can also be obtained from blank scan and tranmission scans and transmission image segmentation methods [24, Section 1.6.1].

1.2.4.2 Scattered Events

One or both of the γ photons after undergoing Compton scattering may still be detected by a detector pair within a coincidence time window. In this scenario, although the coincidence event is counted as a true event, the annihilation event is localized along an incorrect LOR as shown in Figure 1.10 (b). Hence, annihilation events localized to an incorrect LOR due to Compton scattering are termed as scattered

events. Mis-positioning of LOR degrades the spatial resolution of the underlying activity distribution. In 2-D PET, scatter fractions range from 10 % to 20 % depending on the scanner geometry, size of the object, and the energy threshold. In 3-D PET, scatter fractions increase three folds to $30 - 50$ % range [61–63]. Scatter correction can be achieved using convolution-subtraction methods [64, 65], dual-energy window acquisition methods [66], comparisons of 2-D and 3-D distributions [67], and direct calculation of scatter distribution using Klein-Nishina equation [68, 69].

1.2.4.3 Random Events

Two γ photons originating from two distinct annihilation events may be detected within a coincidence time window. This category of true events are called random events (also called accidental coincidences). Random events also localize the annihilation event along an incorrect LOR as shown in Figure 1.10 (c). Detection of one of the γ photons from an annihilation event is called a *single event*. Two independent single events detected within a coincidence time window constitute a random event. Single events happen when the other γ photon (from the same annihilation event) undergoes either of these phenomena:

1. is scattered out of the FOV.

2. passes through the detectors without being detected.

3. is not incident on any detector due to the orientation of the annihilation event, or

4. undergoes photoelectric absorption (< 1 % in PET).

Given a detector pair (i, j), the rate of random events along a LOR, R_r, is defined by the following equation:

$$R_r = \tau S_i S_j \tag{1.17}$$

where S_i and S_j are the singles rate for the detector pair and τ is the coincidence time window. Randoms rate is reduced for narrower coincidence time windows and increases proportionally with the singles rate. Singles rate is directly proportional to the injected activity and, hence, randoms rate is proportional to the square of the injected activity [70]. Randoms correction can be achieved using image-based convolution-subtraction method [65], incorporating an estimated distribution of random events in the image reconstruction framework [71], or delayed-window methods [72]. Distribution of random events can be estimated from the singles rate [73] or analytically computed from the transmission and emissions images [74].

1.2.4.4 Positron Range

Positron range is defined as the distance a positron travels in the medium before annihilating with an electron as depicted in Figure 1.10 (d). Positron range depends on the kinetic energy of the positrons and is tracer dependent. Table 1.2 shows the positron range of commonly used radiotracers in PET. Positron range also introduces spatial blurring in reconstructed images [75]. For ^{18}F radioisotope, positron range is smaller than the intrinsic resolution of the scanner and is often ignored. However, for

^{82}Rb radiotracer used in myocardial perfusion PET or ^{68}Ga used in cancer imaging, positron range is large and may be corrected to remove blurring effects from reconstructed images. Positron range is usually modeled as an image-space blurring kernel which can be incorporated in the image reconstruction framework or removed using deconvolution methods [76–81].

1.2.4.5 Photon Noncollinearity

Positron and electron have non-zero kinetic energy before annihilation. When the two particles annihilate, conservation of momentum can make the annihilation photons deviate from the straight line trajectory as shown in Figure 1.10 (e). The deviation is around 0.4° full width at half maximum (FWHM) [82]. The resolution loss due to photon noncollinearity is a function of the diameter of FOV:

$$FWHM = 0.0022D \tag{1.18}$$

where D is the diameter of the FOV. The larger the FOV (i.e. large D) the larger the mispositioning of the LOR. Photon noncollinearity can be modeled as a sinogram blurring kernel in the image reconstruction framework [83].

1.2.4.6 Depth of Interaction

Figure 1.10 (f) shows that γ photons from coincidence events away from the center of the FOV have increasingly higher probability of penetrating through the detectors

(i.e. enter one detector but penetrate in the adjacent detector). It happens due to the decrease in the detector size subtended by the curvature of the scanner. This spill-over or penetration of photons in the neighboring detectors is called depth of interaction (DOI). DOI results in non-stationary resolution along the radial direction due to mispositioning of LORs [84]. DOI effects can be resolved by computing the detector response function (DRF), as shown in Figure 1.10 (g), and incorporating it in the image reconstruction framework. This approach is called *point spread function* recovery [85–89].

1.2.4.7 Inter-crystal Scattering

γ photons incident on a detector crystal may undergo Compton scattering and/or photo-electrical absorption. Inter-crystal scattering refers to the scattering of incident γ photons in the neighboring crystals. This also results in a mispositioning of LOR [90]. Inter-crystal scattering at the center of the FOV still results in an event being detected along an incorrect LOR. On the contrary, γ photons incident on the edge crystals maybe scattered outside the detector block and lost forever.

1.2.4.8 Detector Sensitivity

Another factor affecting the LOR measurements are variations in the efficiency of the detector elements. The efficiency of the detector elements depends on the angle of incidence of the photons on the crystal surface, effective surface area of the crys-

tal, depth-of-interaction, crystal imperfections, light guide variations, variations in the gains of the photo-multiplier tubes (PMT) and the associated electronics. These variations in the LORs can be compensated by incorporating detector sensitivity factors in the reconstruction process. Detector sensitivity factors, also called normalization coefficients (NCs), can be obtained from a normalization scan which is acquired by illuminating all LORs with an isotropic source [24, Section 1.6.4].

1.2.4.9 Geometric Correction

Circular detector geometry in PET results in non-uniform sampling of LOR in a projection profile. LOR are denser (or narrowly spaced) away from the center of the FOV where they are widely spaced as shown in Figure 1.10 (h). Non-uniform sampling can be resolved by applying a simple geometric correction factor:

$$\triangle r = \triangle d \sqrt{1 - \frac{2r}{D}} \tag{1.19}$$

where $\triangle d$ is the detector width, r is the position of the LOR, D is the diameter of the FOV, and $\triangle r$ is the correction factor [91, Page $516 - 517$].

1.2.4.10 Detector Dead Time

Dead time is the time it takes to process an event. During this time the detector is unable to process incoming events resulting in loss of counts [92]. With higher count rates (corresponding to higher injected dose), a large fraction of counts are lost due

to dead time effects which limits the amount of administered dose [8]. Dead time correction involves scaling the counts by dead time correction factors which can be measured from singles rate [8, Pages 178 – 183].

1.2.4.11 Radioactive Decay

Positron emitting radioisotopes are unstable and undergo radioactive decay. The emitted positrons annihilate with electrons to produce γ photons. With the passage of time, due to radioactive decay, the number of disintegrations per second (dps) decrease resulting in fewer annihilation photons. Decay correction is achieved by rescaling the image counts with decay correction factors which depend on the radionuclide used in the study. Table 1.2 lists the half-lives of commonly used radiotracers in PET.

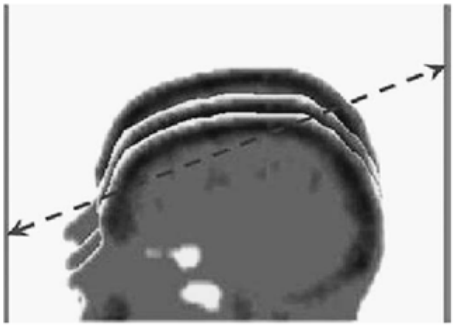

Figure 1.12: Patient motion modifies AFs for individual LOR [93, Figure 2].

1.2.4.12 Patient Motion

High resolution PET imaging has allowed image acquisitions with a spatial resolution of $2-5$ mm FWHM range [94]. Despite enhanced spatial resolution, PET images can

be severely degraded by patient motion thereby undermining the high resolution imaging capability of the scanner. Equation 1.20 relates the effective resolution of a PET image, $FWHM_{\text{effective}}$, with the intrinsic resolution of the scanner, $FWHM_{\text{tomograph}}$, and the $FWHM$ of the distribution of patients motion, $FWHM_{\text{motion}}$ [95]. Resolution degradation is evident when $FWHM_{\text{tomograph}}$ is comparable to $FWHM_{\text{motion}}$.

$$FWHM_{\text{effective}} = \sqrt{FWHM^2_{\text{tomograph}} + FWHM^2_{\text{motion}}} \tag{1.20}$$

Figure 1.12 schematically shows how patient motion modifies AFs for individual LOR and Figure 1.13 shows motion artifacts in reconstructed transmission and emission images for multi-frame PET study.

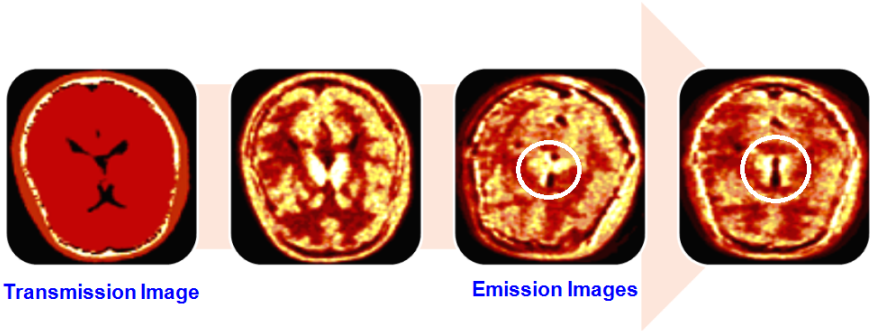

Figure 1.13: Motion artifacts in reconstructed transmission and emission images for multi-frame PET study. White ellipses highlight artifacts due to motion.

Chapter 2 provides an extensive discussion on motion correction in brain PET imaging and proposes a new approach for inter-frame and intra-frame motion correction in dynamic brain PET imaging [96–98].

1.2.5 Pharmacokinetic Analysis in PET Imaging

Reconstructed PET images show radiotracer distribution in the organ(s) of interest. The next step is to relate this activity distribution to the underlying physiological or biochemical processes. This can be achieved by modeling the biological processes of interest, a field called *tracer kinetic modeling* [99–105]. In this thesis, we will focus on compartmental models of tracer kinetics and direct the readers to references [106, 107] for other modeling approaches [104, Section 1].

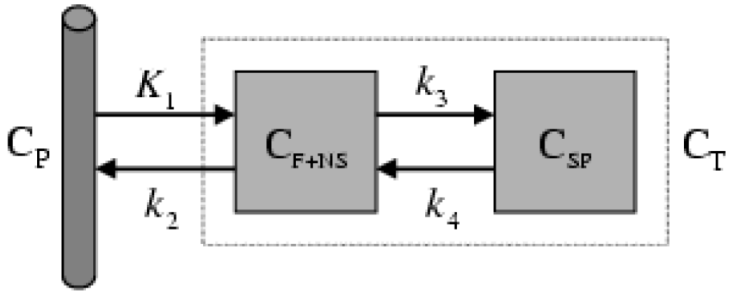

Figure 1.14: Two-tissue compartmental model for PET radiotracers [104, Figure 1]. $C_P(t)$ is the activity concentration time-course in plasma, $C_{F+NS}(t)$ is the activity concentration time-course for free and non-specific binding, and $C_{SP}(t)$ is the activity concentration time-course for specific binding. K_1, k_2, k_3, and k_4 are the transport rate constants.

Figure 1.14 shows a two-tissue compartmental model for PET radiotracers (e.g. ^{18}F-FDG). Tracer dynamics can be described by a system of first-order ordinary differential equations (ODEs) whose coefficients are transport rate constants:

$$\begin{aligned} \frac{\mathrm{d}C_{F+NS}(t)}{\mathrm{d}t} &= K_1 C_P(t) + k_4 C_{SP}(t) - (k_2 + k_3) C_{F+NS}(t) \\ \frac{\mathrm{d}C_{SP}(t)}{\mathrm{d}t} &= k_3 C_{F+NS}(t) - k_4 C_{SP}(t) \end{aligned} \tag{1.21}$$

The solution of ODE (1.21) is given by:

$$C_{F+NS}(t) = \frac{K_1}{\alpha_2 - \alpha_1}[(k_4 - \alpha_1)e^{-\alpha_1 t} + (\alpha_2 - k_4)e^{-\alpha_2 t}]u(t) \otimes C_P(t) \quad (1.22)$$

$$C_{SP}(t) = \frac{K_1 k_3}{\alpha_2 - \alpha_1}[e^{-\alpha_1 t} - e^{-\alpha_2 t}]u(t) \otimes C_P(t) \quad (1.23)$$

where $\otimes$ denotes convolution, $\alpha_1, \alpha_2 = \frac{k_2+k_3+k_4}{2} \mp \frac{\sqrt{(k_2+k_3+k_4)^2 - 4k_2k_4}}{2}$, and $u(t)$ is the unit step function.

The measured PET signal, $C_{PET}(t)$ is the cumulative concentration time-course from the free and non-specific binding compartment, specific binding compartment, and blood plasma in the tissue of interest.

$$C_{PET}(t) = \eta\Big(C_{F+NS}(t) + C_{SP}(t)\Big) + (1-\eta)C_P(t) \quad (1.24)$$

$$C_{PET}(t) = \eta C_{tissue}(t) + (1-\eta)C_P(t) \quad (1.25)$$

where $C_{tissue}(t) = C_{F+NS}(t) + C_{SP}(t)$, and η is the blood volume fraction in the tissue of interest. We are now in a position to formulate the inverse problem in pharmacokinetic analysis which may be solved using iterative techniques e.g. Levenberg-Marquardt algorithm [108, 109]:

[**Inverse Problem: Parametric Imaging**]

Given the measured noisy PET signal $C_{meas}(t)$ and the two-tissue compartment model

of the PET signal, C_{PET} (1.24), solve the following optimization problem

$$\min_{\boldsymbol{\beta}} \|C_{meas}(t) - C_{PET}(t;\boldsymbol{\beta})\|^2_{\boldsymbol{W}} \tag{1.26}$$

where $\boldsymbol{\beta} = [K_1\ k_2\ k_3\ k_4\ \eta]^T$ and $\boldsymbol{W}$ is a diagonal matrix of weighting factors.

Transport rate constants, also called microscopic parameters, and functions of microscopic parameters, called macroscopic parameters, have immense physiological importance and quantitatively capture the physiological and chemical kinetics of the processes under study e.g. relative blood flow [110], glucose metabolism [111], receptor content [112] etc. These quantitative parameters of interest are also called *biomarkers*.

In Chapter 3, we provide a robust approach of estimating quantitative parameter of interest in cardiac PET imaging called *myocardial blood flow* which is a function of uptake rate, K_1.

1.2.6 Clinical Applications of PET

Positron emission tomography (PET) finds numerous applications in clinical oncology [113], brain tumor imaging and quantification [114], myocardial blood flow and flow reserve imaging and quantification in cardiology [115], and molecular drug discovery and development [116, 117].

1.3 Main Contributions

Motion-compensation in Dynamic Brain PET Imaging: We present a frame-based motion correction algorithm referred to as Generalized Inter-frame and Intra-frame Motion Correction (GIIMC) that compensates for motion in a dynamic PET study. Faber et. al. 2009 [118] employed a Richardson-Lucy deconvolution approach [119, 120] to compensate for motion in brain PET imaging. The method was applied to single frame static PET acquisition. We extend this work to enable application to multi-frame dynamic PET acquisition where inter-frame and intra-frame motion compensation are both performed. Another issue not quantified in Faber et. al. 2009 [118] that we carefully study is the occurrence of attenuation artifacts that arise from transmission-emission mismatches. We study this issue elaborately, and show that these mismatch artifacts can become significant in the presence of increasing intra-frame motion. At the same time, we propose a fairly simple approach of using time weighted average of motion transformed transmission images for reconstruction, that alleviates this issue. We validated the proposed approach on extensive simulations with real patient motion profile.

Parametric Myocardial Perfusion PET Imaging: We propose a novel framework of robust kinetic parameter estimation applied to absolute flow quantification in dynamic PET imaging. Kinetic parameter estimation is formulated as a non-linear least squares with spatial constraints problem (NLLS-SC) where the spatial

constraints are computed from a physiologically driven clustering of dynamic images, and used to reduce noise contamination. The proposed methodology makes use of the physiological similarity of voxels to penalize deviation of voxel kinetics from physiological partners. The proposed approach is validated with simulated data (transmural and non-transmural perfusion defect) and clinical studies.

Chapter 2

Motion Correction in Dynamic Brain PET Imaging

Frame-acquired (dynamic) PET images suffer from inter-frame and intra-frame motion artifacts that can degrade the qualitative and quantitative analysis of PET data in the following ways: (1) Patient motion introduces transmission-emission mismatches which leads to an incorrect scatter and attenuation correction in the reconstruction process. As a result, the reconstructed dynamic images carry erroneous estimates of radioactivity distribution [121, 122]. (2) Patient motion modifies the Time Activity Curves (TACs) at a voxel or ROI level resulting in an erroneous estimate of kinetic parameters [123]. (3) Patient motion causes a loss of contrast due to motion-blurring artifacts leading to a poor discernibility of small structures like lesions [124] or small brain structures of neurochemical interests like ventral striatum.

This calls for an appropriate motion correction technique to considerably reduce (ideally eliminate) inter-frame and intra-frame motion artifacts in dynamic PET images. It is important to note that intra-frame motion correction is less readily addressed in comparison to inter-frame motion correction which is commonly incorporated in the various algorithms summarized in Table 2.1.

Dynamic brain PET imaging sessions (e.g. for applications like neuroreceptor mapping and quantification) are typically very long ($\sim 60-120$ mins) making it unreasonable to assume that even very cooperative patients remain static for the entire acquisition duration [125]. This assumption is even worse if the patient is suffering from neurological or psychological disorders resulting in involuntary motion e.g. restless-leg syndrome and epilepsy [126,127], or Tourette's syndrome [128]. Voluntary head movements due to coughing, leg crossing, etc. are also commonly observed in PET scans [129].

Existing motion correction techniques may be grouped into two broad categories [124]: A) algorithms that exploit motion information acquired from optical tracking apparatus [118, 130], and B) algorithms that realign reconstructed PET frames and co-register them to a template (reference) frame [122,124,131,132]. Table 2.1 attempts to summarize motion correction approaches in brain PET imaging. It highlights the pearls and pitfalls of the algorithms used for motion correction in brain PET imaging.

In particular, the method of Multiple Acquisition Frames (MAF) [130] corrects inter-frame motion artifacts by removing average motion from all the independently

Table 2.1: Pearls and pitfalls of motion correction algorithms in brain PET Imaging.

Methods	Pearls	Pitfalls
Head Restraints [127, 133]	• Reduces head movements by fixing the head with the head-rest using thermoplastic masks or neoprene caps.	• Does not eliminate motion. • Relative motion between head-restraint and skull due to coughing, sneezing, leg crossing etc.
Event Driven Correction [127, 134–142]	• Compensates individual lines of response (LORs) based on measured motion information.	• Requires access to list-mode acquired data. • Can lead to artifacts unless careful normalization is performed.
Multiple Acquisition Frames (MAF) [123, 130, 143]	• Corrects for inter-frame artifacts by realigning the independently reconstructed frames to a reference (template) frame.	• Low motion threshold results in acquisition of low-statistics frames and higher reconstruction times. • High motion threshold results in substantial intra-frame motion artifacts. • Increasing the number of frames proportionally increases reconstruction times.
Image Registration Methods [122, 124, 131, 132]	• Provides motion-corrected attenuation correction of PET data with task-related motion. • Corrects for misalignment between transmission and emission scans. • Reduced noise, false-positives and false-negatives.	• It depends on acquired PET data with poor spatial information. • Realignment may occur several times per second instead of realigning long (duration) frames.
System Matrix Modeling [93]	• Incorporates known-motion into system response function used in MLEM. • Does not require list-mode acquisitions.	• Requires access to, and the ability to modify, the system matrix used for reconstruction.
Kernel-based Deconvolution [135]	• Motion-defined deconvolution of motion-blurred reconstructed images. • Theoretically well-behaved for noisless data.	• Deconvolution amplifies noise in PET data. • Spatially variant deconvolution operators required for significant rotations. This augments computational costs and adds potential artifacts.
Iterative Richardson-Lucy Deconvolution [118, 144]	• Incorporates iterative Richardson-Lucy Deconvolution. • Allows spatially variant or nonlinear deblurring kernels. • Does not require list-mode acquisitions. • Can incorporate complex movements.	• Applies only to single-frame PET acquisition. • Attenuation artifacts from misregistration of emission-transmission data. • Transmission-emission mismatches significant with increasing intra-frame motion.

reconstructed frames. The drawback is that a high motion threshold neglects considerable intra-frame motion. By contrast, a low motion threshold results in acquisition of low-statistic frames, thereby, degrading image quality and increasing the number of frames which proportionally increases reconstruction time [95].

Another approach for motion compensation in PET imaging is to employ the Richardson-Lucy (R-L) algorithm [119], [120], as proposed by Faber et al. [118], and further implemented, optimized and validated by Raghunath et al. [144]. The approach was applied to single-frame static PET acquisition (which we extend in the present work to enable application to multi-frame dynamic PET acquisition). Another issue not quantified was the occurrence of attenuation artifacts that arise from transmission-emission mismatches. We study this issue elaborately, and show that these mismatch artifacts can become significant in the presence of increasing intra-frame motion.

An alternative solution to eliminate transmission-emission mismatch artifacts is to correct the individual lines of response (LORs) for motion [134], [127]. This approach is more invasive as it requires access to, and processing of, the acquired list-mode data. More importantly, it has been shown by our group [22, 139] as well as others [137–139, 141] that mere motion compensation of LORs can lead to artifacts, and must be accompanied by modifying probabilities of detection due to motion, posing additional algorithmic and computational complexity to the problem. We have discussed these issues in a review article on motion compensation methods [95].

By contrast, the present work builds upon the straightforward and feasible approach by Faber et al. [118, 144], including extension to dynamic PET acquisition in a framework we refer to as Generalized Inter-frame and Intra-frame Motion Correction (GIIMC) [96], [97]. At the same time, an important component of the present work is to shed light upon and characterize the limitations of the overall R-L framework as applied to motion compensation, and to seek means to alleviate these limitations. As a short summary, the GIIMC algorithm aims to better address the following issues:

- Incorporate inter-frame and intra-frame motion correction in one framework and preserve the desired dynamic framing sequence.
- Reduce transmission-emission mismatches by reconstructing the individual frames with a time-weighted average of motion transformed transmission images for each frame.
- Suppress noise propagation in iterative deconvolution process by performing inter-iteration smoothing.

2.1 Methods and Materials

2.1.1 Inter-frame Motion Correction

In brain PET imaging, patient motion is modeled as a 3-D rigid body motion and, thus, follows the 3-D rigid body kinematics. 3-D rigid body motion can be completely

characterized by a set of 4×4 transformation matrices of the form:

$$\left\{ \begin{pmatrix} \boldsymbol{R} & \boldsymbol{v} \\ \mathbf{0} & 1 \end{pmatrix} \middle| \; \boldsymbol{R} \in SO(3),\ \boldsymbol{v} \in \mathbb{R}^3 \right\} \tag{2.1}$$

where $\boldsymbol{R}$ is a 3×3 rotation matrix and $\boldsymbol{v}$ is a 3×1 translation vector. This forms a Special Euclidean Group, $SE(3)$, which is a 6-D manifold (3 rotation and 3 translation parameters). $SO(3)$ is the group of 3-D rotational matrices defined as follows:

$$SO(3) = \{\boldsymbol{R} \in GL(3) :\ \boldsymbol{R}\boldsymbol{R}^T = I,\ |det(\boldsymbol{R})| = 1\} \tag{2.2}$$

where $GL(3)$ is a set of 3×3 non-singular matrices (Generalized Linear Group). These constraints together with the identification of antipodal points, i.e. points that generate the same rotation matrix, completely characterizes the topology of $SO(3)$ [145, 146].

The first step to correct for inter-frame motion is to compute average motion in each independently reconstructed frame. This is equivalent to computing a transformation matrix which gives the average (mean) motion in each frame. A point that merits close attention is that mere averaging (in a Euclidean sense) of the elements of transformation matrices loses the geometric properties of the individual transformations (except in few exceptions e.g. pure translations) and, hence, is not a valid transformation matrix [91], [147].

Algorithm 1 outlines a procedure for estimating time-weighted mean transformation with a fast convergence rate. The time-weights of each motion transformation for individual frames are derived from the motion file acquired by a Polaris Motion Tracking device during a PET study (Section 2.1.4.2). The details on the necessary and sufficient conditions for the existence, uniqueness and convergence of Algorithm 1 are contained in references [148], [149]. An alternative approach of independently averaging the quaternion and translation components is also possible and yielded comparable results.

Algorithm 1 Manton's weighted mean transformation.

Given: $\{T_i, w_i\}_{i=1}^{N}$, and $\delta > 0$.
input: $K \leftarrow T_i$ for any $i \in \{1, \cdots, N\}$.
Compute: $M \leftarrow \frac{1}{N} \sum_{i=1}^{N} w_i \cdot exp^{-1}(K^{-1}T_i)$.
if $\|M\| < \delta$ **then**
    Set $T_{\text{mean}} \leftarrow K$. **return**
else
    Update $K \leftarrow Kexp(M)$.
    Update $M \leftarrow \frac{1}{N} \sum_{i=1}^{N} w_i \cdot exp^{-1}(K^{-1}T_i)$.
end if
Output: T_{mean}.

2.1.2 Transmission-Emission Alignment Strategies

Subject motion results in spatial misalignment between transmission and emission scans, leading to inaccurate attenuation and scatter correction in the reconstruction process. A common solution to this is to align the transmission image to some "average" position of the emission object within the particular frame of interest. Example of this "average" position includes the mean motion transform or the median motion

transform (Section 2.1.2.1). However, we have observed in the present work that in the case of considerable intra-frame motion, these approaches are sub-optimal, and that an alternative approach is considerably more rewarding. There is a difference between mapping by an average motion transform, versus averaging of images mapped by different motion transforms. We propose using time-weighted average of attenuation sinograms to reconstruct individual dynamic frames. Also proposed is a computationally faster approach of forward projecting a time-weighted average of motion transformed transmission images for reconstruction with comparable results. The mathematical notation used in this section is as follows:

- $\boldsymbol{\mu_0}$ transmission image (μ-map)
- $\boldsymbol{A_0}$ attenuation sinogram obtained from the μ-map
- $T_{i,j}$ i^{th} motion transformation for dynamic frame j
- N_j number of motion transformations in frame j
- $w_{i,j}$ time-weight of i^{th} motion transformation for dynamic frame j

We subdivide the alignment strategies into conventional methods and proposed methods:

2.1.2.1 Conventional Methods

Transmission Image transformed by $T_{1,j}$

$\boldsymbol{\mu_0}$, is transformed by the first (intra-frame) motion-transformation of frame j and then forward projected to generate attenuation sinogram, $\boldsymbol{A_{1,j}}$, which is used to

reconstruct dynamic frame j.

$$\boldsymbol{\mu_{1,j}} = T_{1,j}\{\boldsymbol{\mu_0}\} \tag{2.3}$$

$$\boldsymbol{A_{1,j}} = e^{-fwdproj\{\boldsymbol{\mu_{1,j}}\}} \tag{2.4}$$

Transmission Image transformed by $T_{\mathbf{median},j}$:

The set of intra-frame motion transformations for frame j, $\{T_{i,j}\}_{i=1}^{N_j}$, are sorted chronologically (based on time-stamps) and the median motion transformation, $T_{\text{median},j}$, is computed. $\boldsymbol{\mu_0}$ is transformed by $T_{\text{median},j}$ and then forward projected to generate attenuation sinogram, $\boldsymbol{A}_{\text{median},\boldsymbol{j}}$, which is used to reconstruct dynamic frame j.

$$T_{\text{median},j} = \text{median}\{T_{1,j}, T_{2,j}, \cdots, T_{N_j,j}\} \tag{2.5}$$

$$\boldsymbol{\mu}_{\text{median},\boldsymbol{j}} = T_{\text{median},j}\{\boldsymbol{\mu_0}\} \tag{2.6}$$

$$\boldsymbol{A}_{\text{median},\boldsymbol{j}} = e^{-fwdproj\{\boldsymbol{\mu}_{\text{median},\boldsymbol{j}}\}} \tag{2.7}$$

Transmission Image transformed by $T_{\mathbf{mean},j}$:

Algorithm 1 is used to compute time-weighted mean of intra-frame motion transformations $\{T_{i,j}\}_{i=1}^{N_j}$, for frame j, denoted by $T_{\text{mean},j}$. Then $\boldsymbol{\mu_0}$ is transformed by the single transformation $T_{\text{mean},j}$ and forward projected to generate attenuation sinogram,

$\boldsymbol{A}_{\text{mean},\boldsymbol{j}}$, which is used to reconstruct dynamic frame j.

$$T_{\text{mean},j} = \text{mean}\{T_{1,j}, T_{2,j}, \cdots, T_{N_j,j}\} \tag{2.8}$$

$$\boldsymbol{\mu}_{\text{mean},\boldsymbol{j}} = T_{\text{mean},j}\{\boldsymbol{\mu_0}\} \tag{2.9}$$

$$\boldsymbol{A}_{\text{mean},\boldsymbol{j}} = e^{-fwdproj\{\boldsymbol{\mu}_{\text{mean},\boldsymbol{j}}\}} \tag{2.10}$$

2.1.2.2 Proposed Method

Time-weighted average of attenuation sinograms:

$\boldsymbol{\mu_0}$ is transformed by each of the N_j intra-frame motion-transformation, $\{T_{i,j}\}_{i=1}^{N_j}$, and then forward projected to generate a set of attenuation sinograms, $\{\boldsymbol{A_{i,j}}\}_{i=1}^{N_j}$. A time-weighted average of $\{\boldsymbol{A_{i,j}}\}_{i=1}^{N_j}$ is computed and used to reconstruct dynamic frame j.

$$\boldsymbol{\mu_{i,j}} = T_{i,j}\{\boldsymbol{\mu_0}\} \tag{2.11}$$

$$\boldsymbol{A_{i,j}} = e^{-fwdproj\{\boldsymbol{\mu_{i,j}}\}} \tag{2.12}$$

$$\boldsymbol{A}^{\boldsymbol{p}}_{\text{mean},\boldsymbol{j}} = \sum_{i=1}^{N_j} w_{i,j}\boldsymbol{A_{i,j}} \tag{2.13}$$

One shortcoming of this approach is that it involves N_j forward projection operations for each frame j.

Time-weighted average of Transmission Images:

$\boldsymbol{\mu_0}$ is transformed by each of the N_j intra-frame motion-transformation, $\{T_{i,j}\}_{i=1}^{N_j}$,

to generate a set of motion-transformed transmission images, $\{\boldsymbol{\mu_{i,j}}\}_{i=1}^{N_j}$. A time-weighted average of $\{\boldsymbol{\mu_{i,j}}\}_{i=1}^{N_j}$ is computed and forward projected to generate mean attenuation sinogram, $\boldsymbol{A}^{\boldsymbol{q}}_{\text{mean},\boldsymbol{j}}$, for reconstruction of dynamic frame j.

$$\boldsymbol{\mu_{i,j}} = T_{i,j}\{\boldsymbol{\mu_0}\} \tag{2.14}$$

$$\boldsymbol{\mu}_{\text{mean},\boldsymbol{j}} = \sum_{i=1}^{N_j} w_{i,j}\boldsymbol{\mu_{i,j}} \tag{2.15}$$

$$\boldsymbol{A}^{\boldsymbol{q}}_{\text{mean},\boldsymbol{j}} = e^{-fwdproj\{\boldsymbol{\mu}_{\text{mean},\boldsymbol{j}}\}} \tag{2.16}$$

This approach is computationally faster than the previous one as it performs a single forward projection operation for each frame j.

To see this better, we note that for an object f_{T_i} at a time/position with motion transformation T_i ($i = \{1, \cdots, N\}$), the projected data $\mathbf{Y}$ (prior to adding noise), is given by:

$$\mathbf{Y} = \sum_{i=1}^{N} w_i \boldsymbol{A}_{T_i}\mathbf{P}f_{T_i} \tag{2.17}$$

where $w_i = \triangle T_i/T$ is the time weight for each motion transformation, $\mathbf{P}$ denotes the projection matrix including everything (e.g. image-space blurring, geometric projection and normalization, equation 1.13) except for the effect of attenuation, which, because of the fact that the transmission image is itself also moving, is modified with each motion, and is given by $\boldsymbol{A}_{T_i}$. For a given frame with mean motion $\overline{T}$,

conventional methods assume the following approximation:

$$\mathbf{Y} = \sum_{i=1}^{N} w_i \boldsymbol{A}_{\overline{T}} \mathbf{P} f_{T_i} = \boldsymbol{A}_{\overline{T}} \mathbf{P} \left(\sum_{i=1}^{N} w_i f_{T_i} \right) \tag{2.18}$$

thus arriving at a single sinogram $\boldsymbol{A}_{\overline{T}}$ for attenuation correction of the motion-degraded frame. By contrast, the proposed method effectively assumes the following:

$$\mathbf{Y} = \left(\sum_{i=1}^{N} w_i \boldsymbol{A}_{T_i} \right) \mathbf{P} \left(\sum_{i=1}^{N} w_i f_{T_i} \right) = \overline{\mathbf{A}_T} \mathbf{P} \left(\sum_{i=1}^{N} w_i f_{T_i} \right) \tag{2.19}$$

where $\overline{\boldsymbol{A}_T}$ denotes the overall attenuation sinogram obtained by time-weighted averaging. A fast method to approximate $\overline{\boldsymbol{A}_T}$ is to actually perform time-weighted averaging of the transmission images, followed by forward-projection to obtain mean attenuation sinogram, as opposed to the computationally intense approach of performing individual forward-projections of motion-transformed transmission images, followed by averaging. In fact, we observed both approaches to produce images of very comparable quantitative performance, and as such, pursued the computationally faster approach in what follows.

2.1.3 The GIIMC Algorithm

Algorithm 2 outlines the procedure for the GIIMC Algorithm in multi-frame PET Imaging. Figure 2.1 shows a flowchart of the algorithm.

Algorithm 2 Generalized Inter-frame and Intra-frame Motion Correction Algorithm.

1: **Given:** $\{\mathbf{Y}_j\}_{j=1}^{M}$, $\{T_{i,j}, w_{i,j}\}_{i=1,j=1}^{N_j,M}$, and $\sum_{i=1}^{N_j} w_{i,j} = 1,\ \forall j$.
2: **Compute:** $T_{\text{mean},j}$ for each frame j using Algorithm 1.
3: **Compute:** $\boldsymbol{A}_j$, for each frame j using one of the methods from Section 2.1.2.
4: **Reconstruct:** emission image, $\mathbf{I}_j$ using $\mathbf{Y}_j$ and $\boldsymbol{A}_j$ for each frame j (Section 1.2.3).
5: **Compute:** residual motion transformations, $T_{i,j}^{res} = T_{\text{mean},j}^{-1} \cdot T_{i,j}$ for each frame j.
6: **Inter-frame motion correction:** $\mathbf{Q}_j = T_{\text{mean},j}^{-1}\{\mathbf{I}_j\}$ for each frame j.
7: **Intra-frame motion correction:** R-L iterative deconvolution for each frame j

$$\boldsymbol{\lambda}_j^{n+1} = \frac{\boldsymbol{\lambda}_j^n}{\sum_{i=1}^{N_j} w_{i,j} \cdot T_{i,j}^{res^{-1}}\{\mathbf{1}\}} \sum_{i=1}^{N_j} w_{i,j} \cdot T_{i,j}^{res^{-1}} \left\{ \frac{\boldsymbol{Q}_j}{\sum_{i=1}^{N_j} w_{i,j} \cdot T_{i,j}^{res}\{\boldsymbol{S}(\boldsymbol{\lambda}_j^n)\}} \right\}$$

where n is the iteration number, and $\boldsymbol{S}$ is an inter-iteration smoothing operator (e.g. Gaussian filter with $FWHM = 2$ mm).
8: **Output:** motion compensated multi-frame images $\{\boldsymbol{\lambda}_j\}_{j=1}^{M}$.

2.1.4 Experimental Methods

2.1.4.1 Tomograph

PET data was acquired on the second generation High Resolution Research Tomograph (HRRT) [150]. The detector heads in the octagonal design consist of a double 10 mm layer of LSO/LYSO for a total of 119,808 detector crystals (crystal size $2.1 \times 2.1 \times 10$ mm^3). The total number of possible LORs is 4.486×10^9. The dimensions of the reconstructed image is $256 \times 256 \times 207$ and the voxel volume is $1.219 \times 1.219 \times 1.219$ mm^3. The images were reconstructed using the OSEM algorithm (10 iterations, 16 subsets).

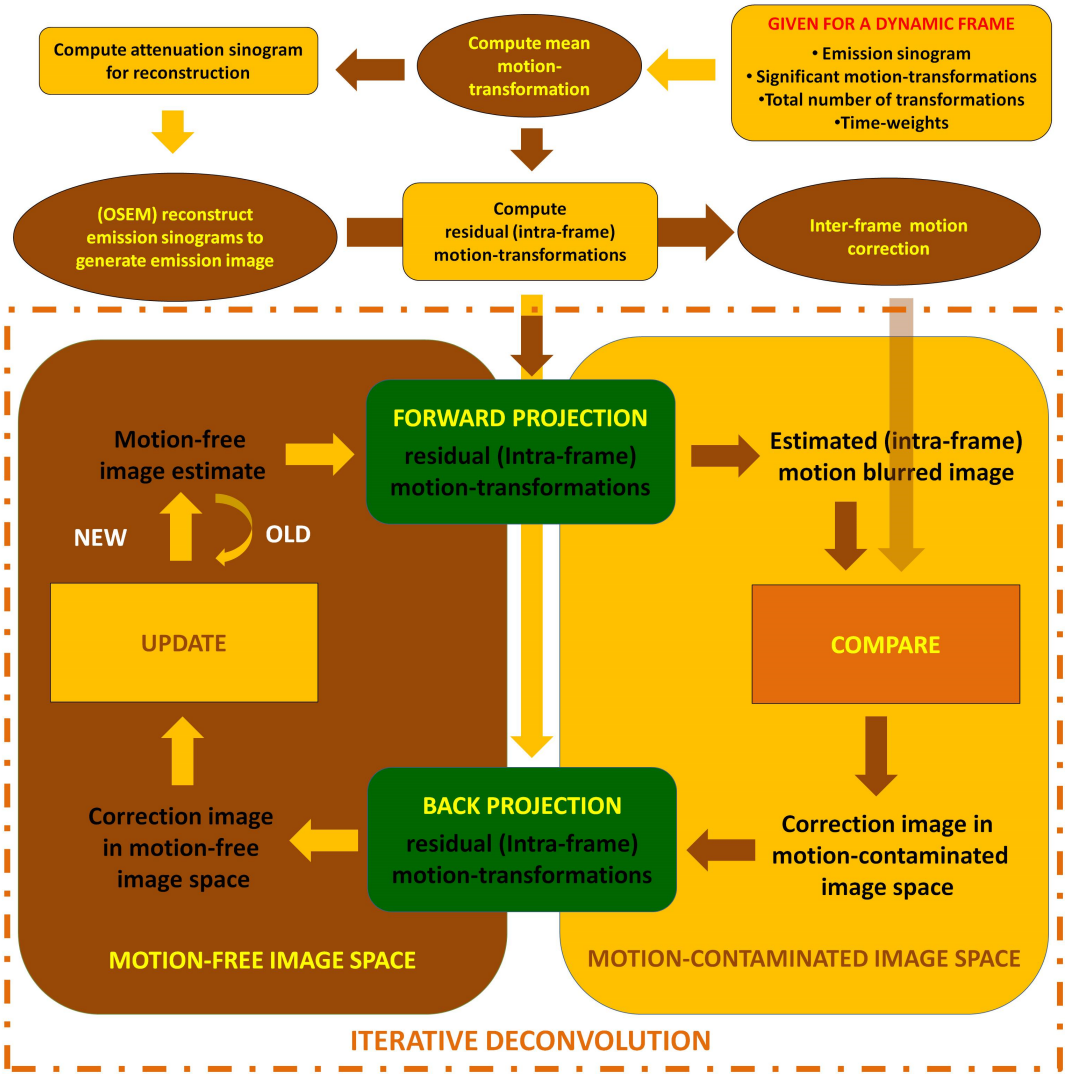

Figure 2.1: Flowchart of GIIMC Algorithm.

2.1.4.2 Polaris Motion Tracking and Calibration

GIIMC algorithm exploits motion information acquired during a PET study using external motion tracking device. In particular, we used Polaris Vicra to track head motion [129, 151]. Polaris Vicra is a high resolution (< 0.1 mm) infra-red (IR) optoelectronic system that uses 4 IR retro-reflective spheres in a known geometry. In

a human study it is fixed to the head via an elastic swimming cap. The 4 spheres face the Polaris inside the gantry which in turn acquires motion-transformations at 30 ms resolution. The Polaris system is synchronized with the PET acquisition using a TCL (Tool Command Language) script and the program generates a motion file containing time-stamped motion parameters (4 quaternion and 3 translation parameters). Polaris motion tracking is insensitive to lighting conditions, uses significantly less disk space for data storage (in comparison to saving optical image sequences) and is commercially available and economical [95].

Polaris-to-Tomograph transformation, $[P2T]_{4\times4}$, was computed via a series of calibration experiments performed simultaneously with Polaris and transmission scan measurements [142], [151]. The Polaris tool was placed in a static position in the scanner and the coordinates of its center along with its orientation (quaternion and translation vectors) were determined by Polaris. Given the knowledge of the relative positions of the 4 spheres, the 3-D positions of the spheres were extracted. During this time, a 10 min transmission scan of the tracking tool was also obtained. From the reconstructed transmission image, the coordinates of the 4 spheres were determined by first isolating the 4 spheres from the clamp-plate and then fitting a 3-D Gaussian to the center of each sphere. This entire process was repeated 10 times to increase the accuracy of the calibration. $[P2T]_{4\times4}$ was obtained by employing a least squares fit to the Polaris and tomograph measurements [152]. $[P2T]_{4\times4}$ is later applied during the post-reconstruction motion compensation procedure.

The motion file generated by the Polaris Vicra consists of motion-transformations in the form of a quaternion vector, $[q_0\ q_1\ q_2\ q_3]$, and a translation vector, $[t_x\ t_y\ t_z]$ i.e. 7 numbers. We first average the motion-transformations accumulated over 1 sec intervals to reduce Polaris measurement noise. This gives us motion-transformations corresponding to each second of PET acquisition. Subsequently we applied a combination of motion threshold $(0.3 - 1$ mm) and a time threshold of 15 seconds duration to get significant motion transformations. The motion threshold (of 1 mm) was set to be one-third of the PET system resolution at the center of the field of view [153]. A time threshold of 15 seconds was empirically chosen to eliminate impulsive motion; i.e. movements that last for very short durations. In Algorithm 2 the significant motion-transformation were represented by $\{T_{i,j}\}_{i=1,j=1}^{N_j\ M}$ and the time-stamps gives us the time weights, $\{w_i\}_{i=1,j=1}^{N_j\ M}$, where M is the total number of frames and N_j is the number of significant motion-transformations obtained for each frame j.

2.1.5 Simulations

We used a Mathematical Brain Phantom (MB-Phantom) [142] to conduct simulation studies based on real-patient motion profile acquired by the Polaris Vicra during subject PET studies. The MB-Phantom is constructed using subdivision surfaces [154]. Subdivision surfaces enable efficient modeling of arbitrary topological structures like brain, skull, muscle tissue, and vasculature. The details on surface modeling are contained in [142] and the references therein. Figure 2.2 shows the transaxial, coronal and

saggital slices of the MB-Phantom. The activity-numbers in the MB-phantom were derived from an FDG study. We then performed analytical simulations incorporating attenuation, normalization and realistic Poisson noise.

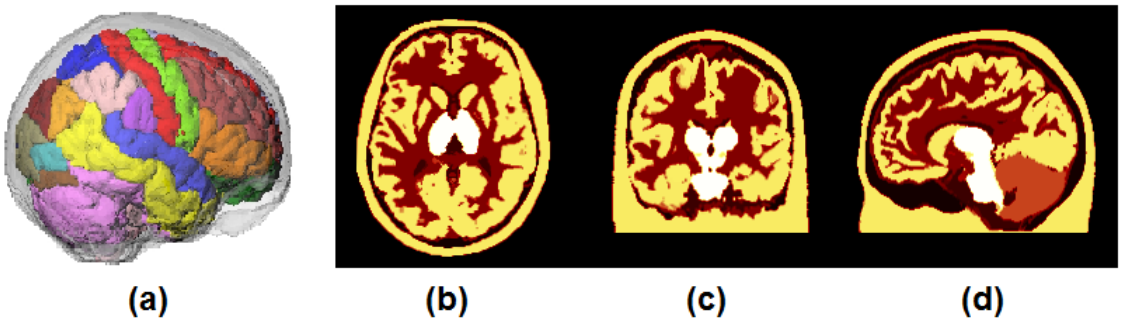

Figure 2.2: (a) Mathematical Brain Phantom. (b)-(d) Transaxial, Coronal, and Saggital slices of the brain phantom.

2.1.6 Subject Study

A human subject was recruited to be scanned on the HRRT scanner following a clinical (non-research) FDG PET scan. The patient was consented and enrolled under a JHU IRB approved research protocol and monitored for safety by a study physician during participation. No adverse events were observed or reported. The Polaris Vicra and PET acquisition system were synchronized with a master clock using TCL scripts. The tracking tool was fixed to the patient's head via an elastic swimming cap. Before scanning, appropriate measures were taken to minimize relative motion between the tracker and the patient's head and to ensure that the tracker did not slip away during scanning. The patient was injected with $\sim$ 20 mCi of FDG 1.75 hrs prior to scanning. A transmission scan was performed for the first 6 mins followed

by a 25 mins emission scan. The patient was asked to remain very still during the transmission scan and the first 5 mins of the emission scan to acquire a reference image with minimal motion. The patient was asked to make a number of movements and move freely for the rest of the study. The Polaris Vicra generated a motion file from which significant motion-transformations for individual frames were extracted. Figure 2.3 shows motion profile of a scanned patient. The markers, ■, show the frame time points (9 frames in total). The framing sequence is 1×300 secs, 8×150 secs. The first 5 mins frame clearly show minimal motion and, hence, is used as a reference frame for qualitative and quantitative analysis. We performed experiments, based on the conventional and proposed methodologies, on the acquired real-patient data and validated our findings from the phantom simulations. We cannot use a hypothetical approach with real-patient PET data as it is an impossible physics scenario. As the patient moves during PET acquisition, the μ-map changes accordingly.

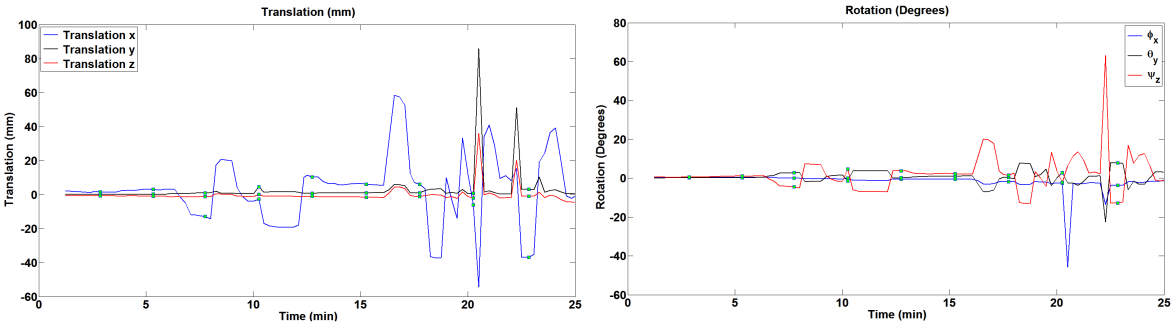

Figure 2.3: Motion profile acquired during a 25 mins emission scan. Row 1 shows the translation profiles and Row 2 shows the rotation profiles in x, y, and z axial-directions wrt to the transmission scan. We see significant translational motion in the x axial-direction and significant rotational motion in the z axial-direction as expected. Markers, ■, shows the frame time points (9 frames in total). The framing sequence is 1×300 secs, 8×150 secs.

Figure 2.4 shows motion-trajectory of a reference point located in the brain for a 150 sec frame duration. The magnitude of intra-frame motion is quantified by mean displacement, $\overline{Disp}$, elaborated in Section 2.1.7. Frame 3 has $\overline{Disp} = 5.92$ mm.

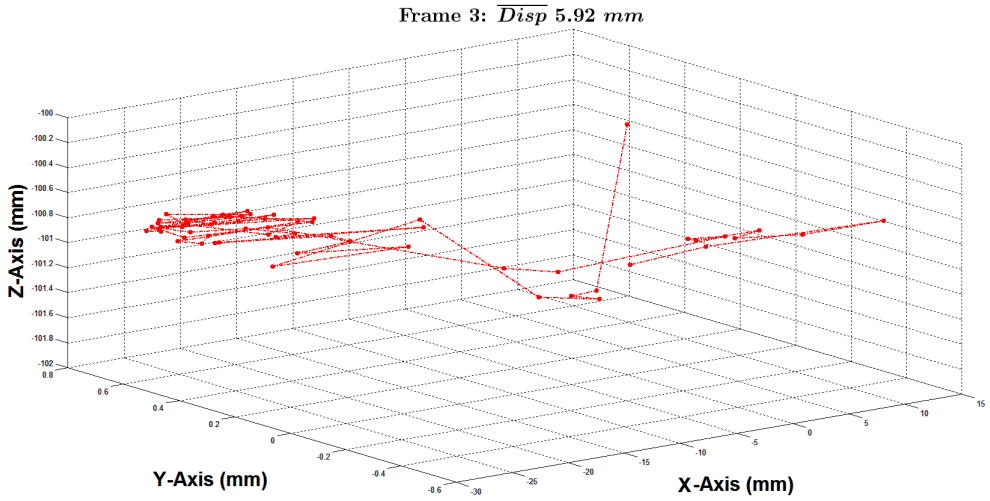

Figure 2.4: Motion trajectory of a reference point located in the brain during a 150 seconds frame. The origin is at the center of the scanners FOV. The magnitude of intra-frame motion is 5.92 mm.

2.1.7 Quantitative Metrics

This section elaborates upon the quantitative metrics used to analyze the motion compensated images. The reference image used in these computations corresponded to the first five minutes of emission scan that contained minimal motion (see Figure 2.3). We preferred it over the original true phantom as the latter does not contain partial volume effects (PVE).

Error-norm:

The error norm is a voxel-wise comparison between the reference image, R, and

the motion compensated PET image, I. It is defined as follows:

$$\|I, R\| = \sum_{i=1}^{N} |I[i] - R[i]| \tag{2.20}$$

Mean Displacement:

We use the time-weighted mean displacement, $\overline{Disp}$, to quantify motion in a dynamic PET image. For each dynamic frame, $\overline{Disp}$ is calculated with respect to the mean motion transformation in that frame, $\overline{T}$:

$$\overline{Disp} = \sum_{i=1}^{V} \sum_{j=1}^{N} w_j \cdot \|T_j[i] - \overline{T}[i]\| \tag{2.21}$$

where V is the total number of voxels in the masked image, N is the total number of significant motion transformations in each frame, w_j is the time-weight for the j^{th} motion transformation, and $T[i]$ denotes the spatial coordinates of voxel i under the motion transformation T.

Noise and Bias:

We quantitatively analyzed different regions of interest (ROIs): white matter, caudate, putamen, cingulate, thalamus, globus pallidus, frontal-orbital gyrus, and occipitotemporal gyrus. For noise-bias analysis, we computed regional bias, RB, and

regional normalized standard deviation, $RNSD$, for each ROI:

$$RB^r = \frac{|\lambda^r - \mu^r|}{\mu^r} \tag{2.22}$$

$$RSND^r = \frac{\sqrt{\frac{1}{L^r-1}\sum_{\beta\in r}(\lambda^\beta - \lambda^r)^2}}{\lambda^r} \tag{2.23}$$

where r indexes the ROIs, λ^r denotes mean reconstructed activity of ROI r in the motion compensated image, μ^r denotes mean activity of ROI r in the reference image, L^r is the total number of voxels in ROI r and $\beta \in r$ indexes them.

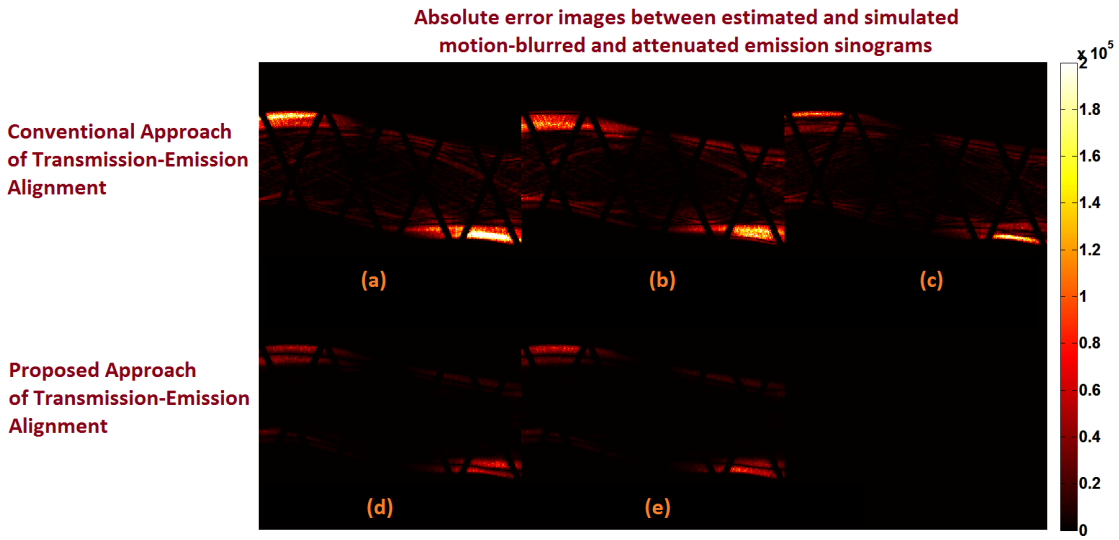

Figure 2.5: Absolute error images between the estimated and simulated motion-blurred and attenuated emission sinogram. (a) uses attenuation sinogram $\boldsymbol{A}_{1,j}$, (b) uses attenuation sinogram $\boldsymbol{A}_{\text{median},j}$, (c) uses attenuation sinogram $\boldsymbol{A}_{\text{mean},j}$, (d) uses attenuation sinogram $\boldsymbol{A}^p_{\text{mean},j}$, and (e) uses attenuation sinogram $\boldsymbol{A}^q_{\text{mean},j}$.

2.2 Results

2.2.1 Comparison of Transmission-Emission Alignment Strategies

We now compare transmission-emission alignment strategies discussed in Section 2.1.2. For quantitative evaluation, we used the following error metric, $E(\boldsymbol{A})$, which is a function of the attenuation sinogram, $\boldsymbol{A}$, used to reconstruct the emission images:

$$E(\boldsymbol{A}) = \left| \sum_{i=1}^{N} w_i \boldsymbol{A}_{T_i} \mathbf{P} f_{T_i} - \boldsymbol{A} \sum_{i=1}^{N} w_i \mathbf{P} f_{T_i} \right| \tag{2.24}$$

Figure 2.5 shows the absolute difference sinogram, $E(\boldsymbol{A})$. The proposed approach is seen to outperform conventional methods by substantially reducing transmission-emission misalignment (order of magnitude improvement).

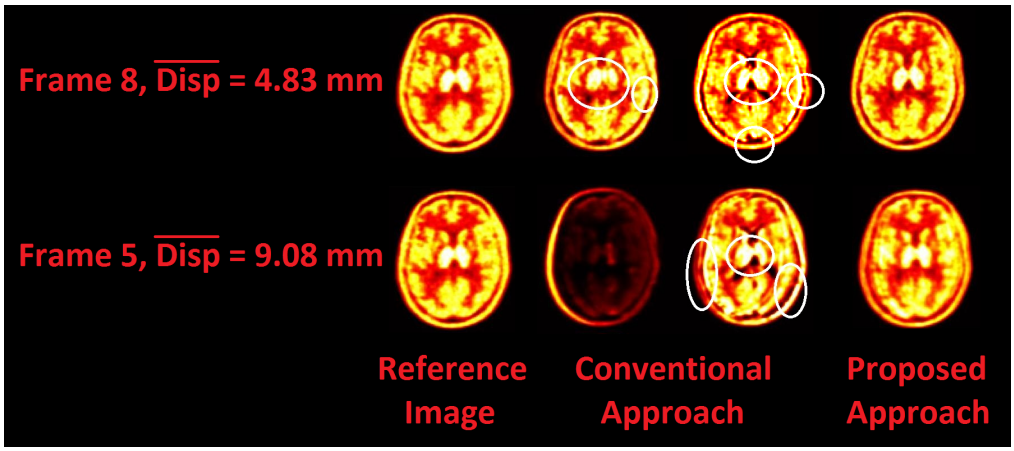

Figure 2.6: (Rows 1 and 2: L-to-R) (a) reference image, motion compensated image using the transmission image transformed by (b) median and (c) mean motion transformation, and (d) the proposed approach of using time-weighted motion transformed transmission images respectively. White ellipses highlight the artifacts in motion compensated images using conventional approach of transmission-emission alignment.

Qualitative and quantitative comparisons of various motion compensated reconstructed images are depicted in Figures 2.6 and 2.7, respectively (Frame 8 with $\overline{Disp} = 4.83$ mm and Frame 5 with $\overline{Disp} = 9.08$ mm). It is seen that the proposed approach of transmission-emission alignment considerably reduced mismatch artifacts and produced images with superior quality compared to conventional methods. With increased intra-frame motion (higher $\overline{Disp}$), transmission-emission mismatch becomes increasingly significant, and the motion compensated images from conventional methods degraded severely. The proposed approach showed substantial improvement even for motion magnitude of ~ 9 mm. From here on, the results from simulations and subject study will focus only on using the transmission image transformed by the mean (not median) motion $\overline{T_j}$, for each frame j, for conventional approach and using time-weighted average of motion transformed transmission images for the proposed approach.

2.2.2 Qualitative and Quantitative Analysis of Phantom Simulations

Figure 2.8 depicts motion compensated images obtained from phantom simulations. We depict results from Frame 5 and Frame 8 with $\overline{Disp} = 4.83$ mm and $\overline{Disp} = 9.08$ mm respectively. We show motion compensated images with inter-frame motion correction only, as well as additional intra-frame motion correction (with deconvolution iterations 8 and 15 respectively), employing conventional and proposed approaches of transmission-emission alignment.

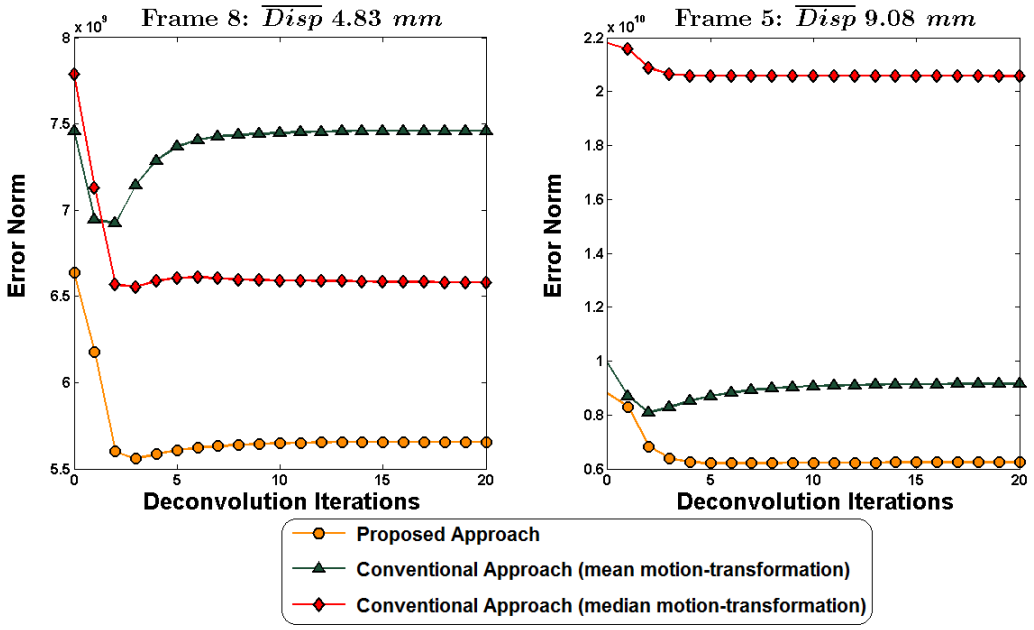

Figure 2.7: Error norm curves from simulations using different transmission-emission alignment strategies. The proposed approach of using time-weighted motion transformed transmission images clearly outperforms conventional methods for minimizing mismatch artifacts in motion compensated images.

Our proposed approach is seen to considerably remove inter-frame and intra-frame motion artifacts. The results are consistent across different levels of intra-frame motion. The conventional approach produced images that are visibly degraded by transmission-emission mismatch artifacts, even with small movements. These artifacts are amplified with increased deconvolution iterations and motion levels. We concluded from this qualitative analysis that the proposed approach produced motion compensated images with superior quality. We now substantiate this assessment through quantitative analysis of motion compensated dynamic images.

Figure 2.9 shows the error norm curves for the proposed and conventional approaches with varying deconvolution iterations. 0^{th} deconvolution iteration implies

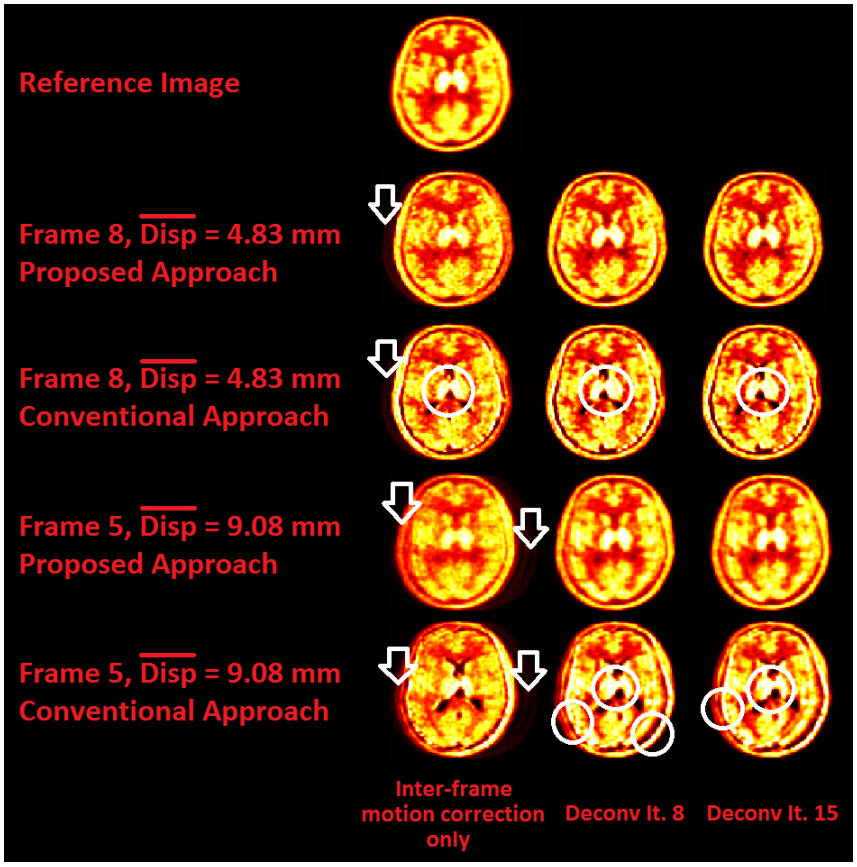

Figure 2.8: (L-to-R) inter-frame motion compensated images, inter-frame and intra-frame motion compensated images with conventional and proposed approaches of transmission-emission alignment, and deconvolution iterations 8 and 15 respectively. White ellipses highlight artifacts. Proposed approach outperforms conventional methods in producing motion compensated images with superior quality.

inter-frame only motion correction. We omitted frames with negligible intra-frame motion. The proposed approach showed a larger error drop compared to the conventional approach. In fact, for the conventional approach, the error norm increases with deconvolution iterations and intra-frame motion. This is again attributed to transmission-emission mismatch which starts to dominate with higher intra-frame motion.

Figure 2.10 shows the Error Norm vs. $\overline{Disp}$ plots for the proposed and con-

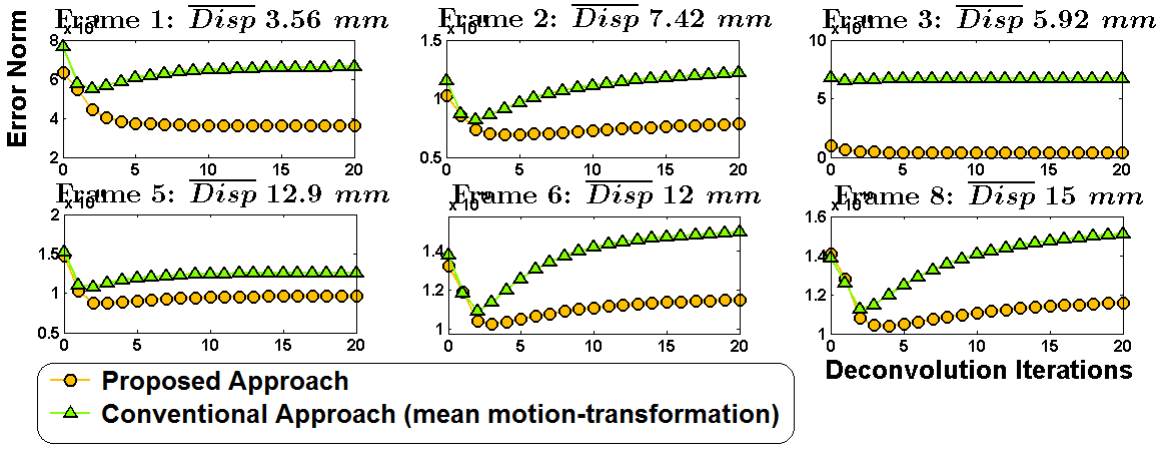

Figure 2.9: Error norm plot for different frames against deconvolution iterations (10 OSEM iterations, 16 subsets). 0^{th} iteration implies intra-frame only motion correction. Proposed approach outperformed conventional approach exhibiting a larger error drop. Conventional approach showed an increase in error norm because the transmission-emission mismatch starts to dominate with increased deconvolution iterations.

ventional approaches with inter-frame and intra-frame motion correction (10 deconvolution iterations). We obtained a proportional relationship between error norm and $\overline{Disp}$. Conventional approach showed significant discrepancy with increasing intra-frame motion (quantified by $\overline{Disp}$). Even at higher levels of intra-frame motion (higher $\overline{Disp}$), the proposed approach showed a significantly better error performance compared to the conventional approach.

Figure 2.11 shows overall noise vs. bias plots for deconvolution iterations 1, 2, 3, 5, 8, 10, 15, and 20 (across 8 ROIs). The proposed approach outperformed conventional approach in noise vs. bias tradeoff at different magnitudes of intra-frame motion. With increasing deconvolution iterations we saw a greater reduction in bias at a cost of smaller increase in noise levels. For conventional approach, the noise-bias performance worsened with increasing deconvolution iterations, which is attributed

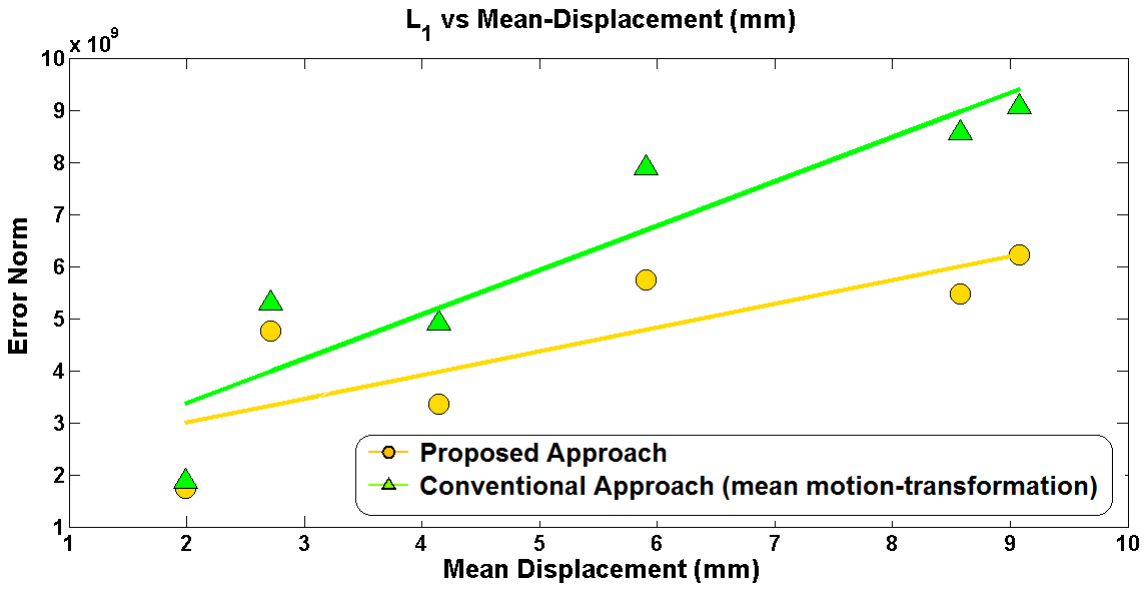

Figure 2.10: Error Norm vs. $\overline{Disp}$ plot for individual frames. It shows increased discrepancy with higher intra-frame motion (higher $\overline{Disp}$). Proposed approach outperforms conventional approach by significantly reducing the transmission-emission mismatch artifacts (as shown by a better error performance).

to the transmission-emission mismatch artifacts.

2.3 Discussions and Conclusions

We have presented an approach to correct for intra-frame motion in multi-frame PET imaging. Intra-frame motion compensation is achieved by iteratively removing residual motion blur from the individually reconstructed frames using a Richardson-Lucy deconvolution approach. To more appropriately accommodate this framework, we presented a novel approach of using time-weighted averaging of motion transformed transmission images to mitigate transmission-emission mismatch artifacts caused by patient motion. Our methodology is amenable to different framing sequences in a dynamic study.

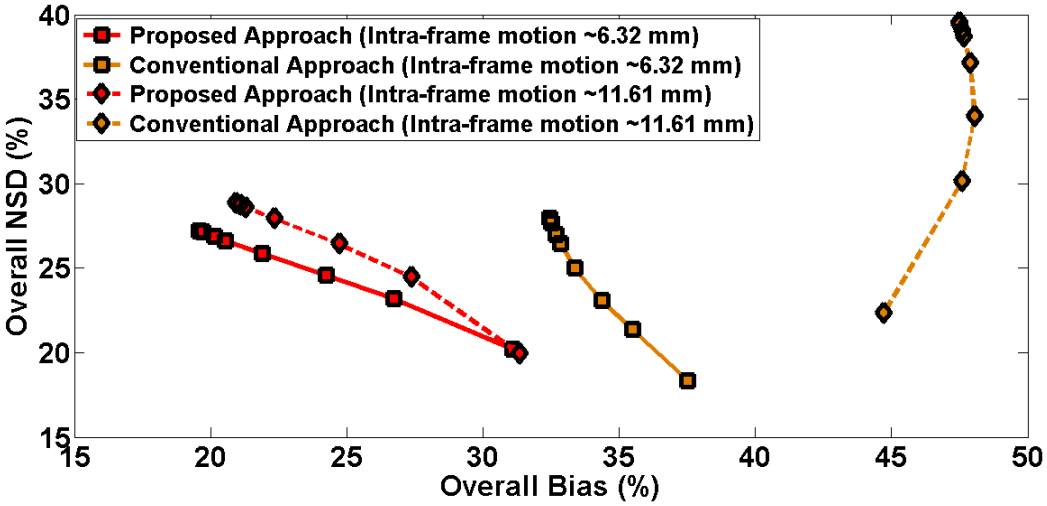

Figure 2.11: Overall noise-bias plots across deconvolution iterations 1, 2, 3, 5, 8, 10, 15, 20 respectively for 8 ROIs. Proposed approach shows a better noise-bias performance over conventional approach with a greater reduction in bias at a cost of smaller increase in noise levels.

We studied three transmission-emission alignment strategies in multi-frame PET imaging at various magnitudes of intra-frame motion (quantified by $\overline{Disp}$). The first two approaches, classified as conventional methods, used: (1) transmission image transformed by mean motion transformation, and (2) transmission image transformed by median motion transformation to generate ACFs. The third approach, our proposed method, performed time-weighted averaging of motion transformed transmission images to generate ACFs. The reconstructed images were corrected for inter-frame and intra-frame motion. Qualitative analysis of motion compensated images showed that the proposed approach produced images with superior quality compared to the conventional approach (Figure 2.6). Small regions of interest such as the caudate and putamen were clearly distinguishable, and the functional morphology was preserved for different magnitudes of intra-frame motion. On the contrary, the im-

ages from the conventional approach were visibly degraded by transmission-emission mismatch artifacts that degraded the uptake distribution in the caudate and putamen (Figure 2.6). The artifacts became severe with increasing intra-frame motion. Quantitative analysis of motion compensated images showed that the proposed approach resulted in a substantial reduction of error norm in comparison to conventional methods (Figure 2.7), thus further validating our inference from qualitative analysis. Hence, the proposed approach of using time-weighted average of motion transformed transmission images showed enhanced recovery both qualitatively and quantitatively by substantially reducing transmission-emission mismatch artifacts in reconstructed images.

In the context of multi-frame PET images, incorporating the proposed transmission-emission alignment strategy, qualitative and quantitative analysis from simulations showed that our approach of intra-frame motion compensation produced images with superior quality (Figure 2.8), improved accuracy (Figure 2.9), and enhanced noise-bias performance (Figure 2.10). Error norm increased with intra-frame motion (Figure 2.11), which was attributed to the significant transmission-emission mismatch artifacts. However, even for high intra-frame motion, the proposed methodology of transmission-emission alignment and intra-frame motion compensation resulted in considerably less error norm (discrepancy) compared to conventional approach and inter-frame only motion compensated images.

Following development and validation of the proposed framework as presented

here, future efforts include application to cohort studies involving dynamic PET imaging and assessment in the context of quantitative parametric imaging. In parallel, we note that our intra-frame motion correction approach relies on accurate tracking of patient motion over time. The Polaris Vicra optical tracking system is utilized by a number of users and has resulted in enhanced reconstructions for different algorithms [129, 138, 151, 155]. Nonetheless, use of this device has the potential to suffer from drifts of the cap on which the retro-reflective spheres are mounted or of the scalp with respect to the skull (e.g. due to rubbing of head against the bed). Tracking solutions that seek to minimize such issues are clearly preferred, an example of which has been the promising use of structured light motion tracking of the face [156, 157], which can be utilized in the context of our proposed methodology.

In conclusion, we have empirically demonstrated that: (1) reconstructing emission images with time-weighted average of motion transformed transmission images greatly reduces transmission-emission mismatches. (2) Coupled with a Richardson-Lucy deconvolution procedure to compensate for intra-frame motion, our proposed approach produces motion compensated images with superior quality compared to the conventional approach which is prone to noticeable transmission-emission mismatch artifacts. (3) Our proposed methodology works for different framing sequences in a dynamic study.

Chapter 3

Quantitative Myocardial Perfusion PET Imaging

Quantitative myocardial perfusion (MP) PET has the potential to enhance detection of early stages of atherosclerosis or microvascular dysfunction, characterization of flow-limiting effects of coronary artery disease (CAD), and identification of balanced reduction of flow due to multivessel stenosis. We aim to enable quantitative MP-PET at the individual voxel level, which has the potential to allow enhanced visualization and quantification of myocardial blood flow (MBF) and flow reserve (MFR) as computed from uptake parametric images. This framework is especially challenging for the ^{82}Rb radiotracer. The short half-life enables fast serial imaging and high patient throughput; yet, the acquired dynamic PET images suffer from high noise-levels introducing large variability in uptake parametric images and, therefore, in the estimates

of MBF and MFR. Robust estimation requires substantial post-smoothing of noisy data, degrading valuable functional information of physiological and pathological importance. We present a feasible and robust approach to generate parametric images at the voxel-level that substantially reduces noise without significant loss of spatial resolution. The proposed methodology, denoted physiological clustering, makes use of the functional similarity of voxels to penalize deviation of voxel kinetics from physiological partners. The results were validated using extensive simulations (with transmural and non-transmural perfusion defects) and clinical studies. Compared to post-smoothing, physiological clustering depicted enhanced quantitative noise vs. bias performance as well as superior recovery of perfusion defects (as quantified by CNR) with minimal increase in bias. Overall, parametric images obtained from the proposed methodology were robust in the presence of high-noise levels as manifested in the voxel time-activity-curves.

3.1 Introduction

Studies worldwide have attributed a high morbidity and mortality rate to cardiovascular diseases [158–162]. The World Health Organization has predicted that by 2030 approximately 23.6 million people will die due to coronary artery disease. Subsequently, there has been considerable attention and efforts devoted to instrumentation, experimentation, assessment, and analysis of the early detection, staging, and management of CAD [163].

Absolute quantification of myocardial blood flow (MBF) and flow reserve (MFR), i.e. ratios of MBF values at peak stress to rest, augments conventional myocardial perfusion imaging (MPI) and can potentially allow early detection of preclinical atherosclerosis, providing an opportunity to modify risk factors or initiate treatment [162, 164, 165]. MFR has been shown to be related to the degree of coronary artery stenosis (CAS) [166]. It thus allows for noninvasive assessment of the functional importance of CAS and may aid identification of patients with either diffuse, nonocclusive luminal coronary artery narrowing or a balanced reduction in coronary artery blood flow (extensive multi-vessel coronary disease) [167].

PET naturally enables noninvasive and accurate quantification of MBF and MFR [163, 168–170], and compared to SPECT, has higher sensitivity as well as superior spatio-temporal resolution, and involves more straightforward attenuation correction [22, 164, 171–174]. Dynamic cardiac PET has also demonstrated superior diagnostic accuracy and added prognostic value for the detection of CAD at low levels of administered dose [170, 175–177].

Despite all these benefits, quantification of MBF and MFR remains to be translated into routine clinical practice and, thus far, remains primarily as a research adventure. An impediment has been the need for production and delivery of short-lived radiotracers at the clinical site. ^{82}Rb provides great opportunities to this end [163, 178, 179], as it does not require an onsite cyclotron. Furthermore, its short half-life of 76 secs enables fast serial imaging ($\sim$ 15 mins) [180] and high patient

throughput. However, low count statistics produces very noisy dynamic (uptake) images adversely impacting accurate quantification of MBF and MFR especially at the voxel-level (parametric images) [181]. Figure 3.1 shows LV myocardial uptake images (without post-smoothing) from a clinical study and the corresponding voxel time activity curves (TACs). The TACs demonstrate an erratic behavior due to poor SNR at the voxel scale. Such a concentration curve may be physiologically implausible resulting in highly unstable parameter estimates [182].

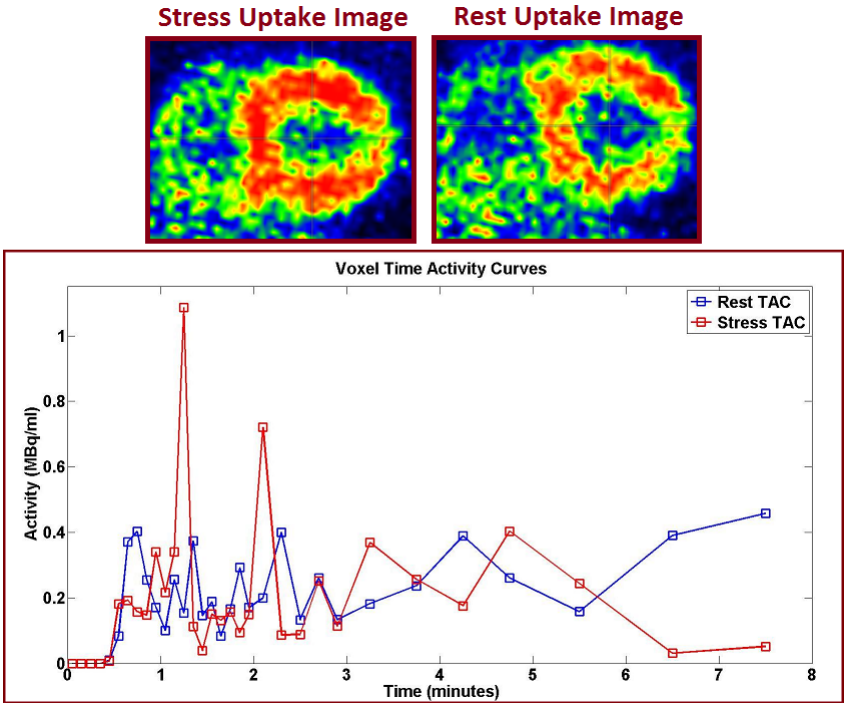

Figure 3.1: *(top)* Short-axis view of LV myocardial uptake images for ^{82}Rb radiotracer (without post-smoothing) from a clinical subject. Uptake images are summed images from 24 minutes. High noise-levels are clearly visible in the images. *(bottom)* The LV myocardium TACs, at the voxel-scale, exhibit an erratic time-course due to poor SNR in the dynamic images. This results in highly unstable estimates of physiological parameters of interest at the voxel-level.

We emphasize that we aim to enable quantitative MP PET at the individual voxel

level. This has the potential to enable enhanced visualization and quantification of MBF/MFR as well as abnormal decrease (gradient) in longitudinal myocardial blood flow from the base to the apex of the heart (e.g. diffuse luminal narrowing in patients with mild angiographic CAD) [183–187]. One way to address the issue of high noise-levels is to perform heavy post-smoothing on reconstructed dynamic images before estimating functional parameters by kinetic modeling. This comes at a cost of substantial resolution degradation (high estimation bias). Another approach is to perform region-of-interest (ROI) quantification of MBF and MFR where the voxel intensities are averaged over each ROI. This also comes at a cost of loss of spatial information and underlying tissue heterogeneity.

One way to address the issue of high noise-levels is to perform heavy post-smoothing on reconstructed dynamic images before estimating functional parameters by kinetic modeling. This comes at a cost of substantial resolution degradation (high estimation bias). Another approach is to perform region-of-interest (ROI) quantification of MBF and MFR where the voxel intensities are averaged over each ROI. This also comes at a cost of loss of spatial information and underlying tissue heterogeneity. Table 3.1 reviews some of the existing approaches in quantitative imaging literature for the estimation of functional parameters of interest at an ROI or voxel-level.

We propose a novel framework of robust kinetic parameter estimation at the individual voxel level that substantially reduces noise using a method which we term "physiological clustering" [188], and as elaborated in Section 3.2. Physiological clus-

tering is an approach of clustering a PET image driven by the underlying physiology. The resulting label map is a union of disjoint clusters each represented by its mean kinetics. The parameter estimation problem is then formulated as nonlinear least squares with spatial constraints (NLLS-SC) where the spatial constraints are derived from the physiologically clustered image.

Section 3.3 describes the experimental design used to validate our methodology, with results presented in Section 3.4. Discussions and conclusions are presented in Sections 3.5 and 3.6 respectively.

3.2 Theory

3.2.1 Pharmacokinetic Model for the ^{82}Rb Radiotracer

^{82}Rb radiotracer kinetics can be described by a one-tissue compartment model [181, 189–191]. The myocardial activity concentration time-course, $C_{myo}(t)$, is defined by first-order ordinary differential equation (ODE):

$$\frac{\mathrm{d}C_{myo}(t)}{\mathrm{d}t} = K_1 C_a(t) - k_2 C_{myo}(t) \tag{3.1}$$

where $C_a(t)$ is the arterial input function (which is commonly approximated by $C_{LV}(t)$, the LV blood concentration time-course, as used from here onwards), and K_1 (uptake rate in units of mL/min/g) and k_2 (washout rate in units of 1/min) are the transport rate constants. Solving the ODE (equation 3.1) for $C_{myo}(t)$ gives the

Table 3.1: A brief review of some of the existing approaches in quantitative imaging literature for the estimation of physiological parameters of interest at an ROI or voxel-level.

Methods	Remarks
ROI-average Approach [192–195]	• number of computations reduced from number of voxels (N_V) to number of ROIs (N_R), where $N_R << N_V$. • loss of spatial information and underlying tissue heterogeneity. • neglects spatial variations of tracer kinetics within an ROI due to partial volume effects (PVE).
Least Squares Approach Basis Function Method [104, 196]	• preserves tissue heterogeneity by computing voxel-wise parameter estimates. • unstable parameter estimates due to poor SNR.
Regularization Approach [197–199]	• stabilizes voxel-wise parameter estimation by adding a smoothness constraint (penalty function) e.g. Tikhonov regularization. • smoothness penalties blur edges and can be replaced by edge-preserving penalties. • mutual information penalties to incorporate structural information.
Mixture Modeling [200, 201]	• represents voxel TACs as a mixture of multiple kinetic processes (biological heterogeneity, low spatial resolution, PVE).
Bayesian Approach [202, 203]	• models the noise in the TACs as a Gaussian error distribution. • facilitates uncertainty quantification of estimated kinetic parameters. • high variance in voxel-wise estimates due to poor SNR.
Clustering Approach [204–211]	• clusters the dynamic images into several homogeneous regions. • clustering based on lowest-order moments (tracer clearance rate, k_2). • clustering based on the shape and magnitude of TACs. • hierarchical clustering using weighted dissimilarity metric. • clustering based on multivariate Gaussian mixture models.
Wavelet Processing [212–220]	• image denoising using spatio-temporal wavelets. • apriori knowledge of the dimensionality of wavelet transform is required. • denoising procedure depends on the chosen threshold for the shrinkage operation.

following convolution equation:

$$C_{myo}(t) = C_{LV}(t) \otimes K_1 e^{-k_2 t} \tag{3.2}$$

where we use $C_a(t) = C_{LV}(t)$. Due to partial volume effects (PVE), caused by the limited resolution of PET scanners, the measured myocardial tissue concentration time course, $C_{meas}(t)$, is contaminated by "spill-over" of activity from the LV blood-pool and the RV blood-pool:

$$C_{meas}(t) = f_{LV} C_{LV}(t) + f_{RV} C_{RV}(t) + (1 - f_{LV} - f_{RV}) C_{LV}(t) \otimes K_1 e^{-k_2 t} \tag{3.3}$$

where $f_{LV}(f_{RV})$ is the fractional blood volume spill-over from LV (RV) that accounts for contribution of blood activity in the measured myocardial tissue concentration time-course.

K_1 estimates from a ^{82}Rb study needs to be corrected for the extraction fraction, EF, which can be performed via the generalized Renkin-Crone model [221].

$$K_1 = MBF \times EF = MBF \times \left(1 - ae^{-\frac{b}{MBF}}\right) \tag{3.4}$$

The extraction fraction, EF, is a nonlinear function of MBF and decreases with increase in MBF due to tracer extraction from blood via diffusion and active transport [222, 223]. Many studies have reported the generalized Renkin-Crone model

parameters (a and b) for various radiotracers and a comprehensive table can be found in [181, Table 4]. In this work we chose $a = 0.77$ and $b = 0.63$ [189].

3.2.2 Image Derived Input Functions

The input function can be measured invasively by arterial cannulation which is a cumbersome procedure, both for the clinician and the patient. This calls for alternative ways to acquire the input function. Generation of image derived input function (IDIFs) from the reconstructed dynamic images is the noninvasive and feasible alternative [224]. In the above-mentioned commonly utilized framework (i.e. equation 3.3), estimation of the parameter vector $\boldsymbol{\beta} \triangleq [K_1 \ k_2 \ f_{LV} \ f_{RV}]^T$ requires knowledge of the input functions $C_{LV}(t)$ and $C_{RV}(t)$, which are conveniently estimated given the large blood pools of LV and right atrium (RA) in the PET FOV [164].

$C_{LV}(t)$ and $C_{RV}(t)$ were extracted from co-registered dynamic PET images by placing an elliptical ROI (~ 100 mm^2) in the LV and RV blood pools. These concentration curves are generated from 4 mid-ventricular imaging planes and then averaged to reduce noise [225].

3.2.3 Physiological Clustering

Clustering techniques for enhanced parameter estimation have been reported before [205, 207–210]. However, in this work, clustering is driven by the underlying physiology of functional regions. The physiological clustering approach for noise re-

duction is motivated by the observation that *accurate kinetic parameter estimation requires segmentation; ideal segmentation requires knowledge of the underlying physiological (kinetic) parameters* [211]. This dilemma is easily addressed by performing clustering and kinetic modeling in an iterative fashion. This approach reduces bias propagation from clustering into parameter estimation which may dominate if the two processes are performed separately.

Algorithm 3 describes a pseudocode for physiological clustering that uses K-means with kinetic modeling (KM-KM) [211]. K-means clustering uses the Euclidean norm of the TACs to gauge physiological similarity of a pair of voxels indexed by (i, j):

$$S_{K-means}(i,j) = \|\boldsymbol{TAC}_i - \boldsymbol{TAC}_j\|_{\boldsymbol{W}} \tag{3.5}$$

$$= \sqrt{(\boldsymbol{TAC}_i - \boldsymbol{TAC}_j)^T \boldsymbol{W} (\boldsymbol{TAC}_i - \boldsymbol{TAC}_j)} \tag{3.6}$$

where $\boldsymbol{W}$ is the data weighting matrix. Algorithm 3 generates a label map where each functionally homogeneous region is represented by mean kinetics. Mean kinetics of each cluster forms the spatial constraints set $\{\boldsymbol{\beta}_{sc}\}$ for robust parameter estimation.

Algorithm 3 Physiological Clustering: K-means clustering with Kinetic Modeling (KM-KM)

1: **Given:** number of clusters, N.
2: Smooth dynamic images **only** for the generation of label map.
3: Randomly sample the dynamic space to select N representation TACs for the myocardial tissue.
4: Perform kinetic modeling to estimate kinetic parameters from the N representation TACs.
5: Compute noise-free TACs from the estimated kinetic parameters in Step 4. These N TACs form the initial cluster centroids for clustering.
6: **repeat**
7: Generate voxel-wise label map using K-means clustering and the N representation TACs from Step 5.
8: Compute representative TACs (noisy centroids) for the N clusters using the label map from Step 7.
9: Repeat Step 4 to estimate kinetic parameters for the N representation TACs from Step 8.
10: Repeat Step 5 to generate a new set of N representative, noise-free, TACs (cluster centroids).
11: **until** (no significant change in cluster centroids)
12: Estimate kinetic parameters from the final set of N representative, noise-free, TACs.
13: **Output:** Kinetic parameters from Step 12 act as spatial constraints for their individual clusters.

3.2.4 Robust Parameter Estimation

Robust estimation of physiologically meaningful parameters (like the uptake rate K_1) is achieved by solving the following nonlinear least squares with spatial constraints (NLLS-SC) optimization problem for each voxel:

$$\hat{\boldsymbol{\beta}} = \underset{\boldsymbol{\beta}}{\operatorname{argmin}} \|\boldsymbol{C_{meas}}(\boldsymbol{t};\boldsymbol{\beta}) - \boldsymbol{C_{PET}}(\boldsymbol{t})\|^2_{\boldsymbol{W}} + \gamma\|\boldsymbol{\beta} - \boldsymbol{\beta}_{sc}\|^2_2 \tag{3.7}$$

where $\boldsymbol{\beta} \triangleq [K_1\ k_2\ f_{LV}\ f_{RV}]^T$ is the desired parameter vector, $\boldsymbol{C_{meas}}(\boldsymbol{t},\boldsymbol{\beta})$ models the measured PET signal (equation 3.3), $\boldsymbol{C_{PET}}(\boldsymbol{t})$ is the measured voxel TAC, $\boldsymbol{\beta}_{sc}$ is the spatial constraint derived from physiological clustering of dynamic images (Algorithm 3; as concluded with step 13), and $\boldsymbol{W}$ is the data weighting matrix. Each voxel belongs to one of the N clusters and the representative kinetic parameter vector for that cluster forms the spatial constraint vector. γ penalizes large deviations from mean kinetics. Figure 3.2 depicts a flowchart of the overall proposed approach.

Equation 3.7 is solved using the basis function method [196] for weighted least squares. $\boldsymbol{W} = \text{diag}\{\frac{\triangle \boldsymbol{t}^2}{\boldsymbol{DF}^2\boldsymbol{C}}\}$ where $\triangle\boldsymbol{t}$, $\boldsymbol{DF}$, and $\boldsymbol{C}$ are vectors of frame durations, decay correction factors, and frame counts respectively [226, Page 76]. 200 basis functions ($\boldsymbol{B}_i(k_2^i;\boldsymbol{t})$; $i = \{1,\cdots,200\}$) were assumed with nonlinear parameter, k_2^i, logarithmically spaced in the range [0 1]. MBF is estimated from K_1 by solving equation 3.4 using a fixed-point iteration approach [227].

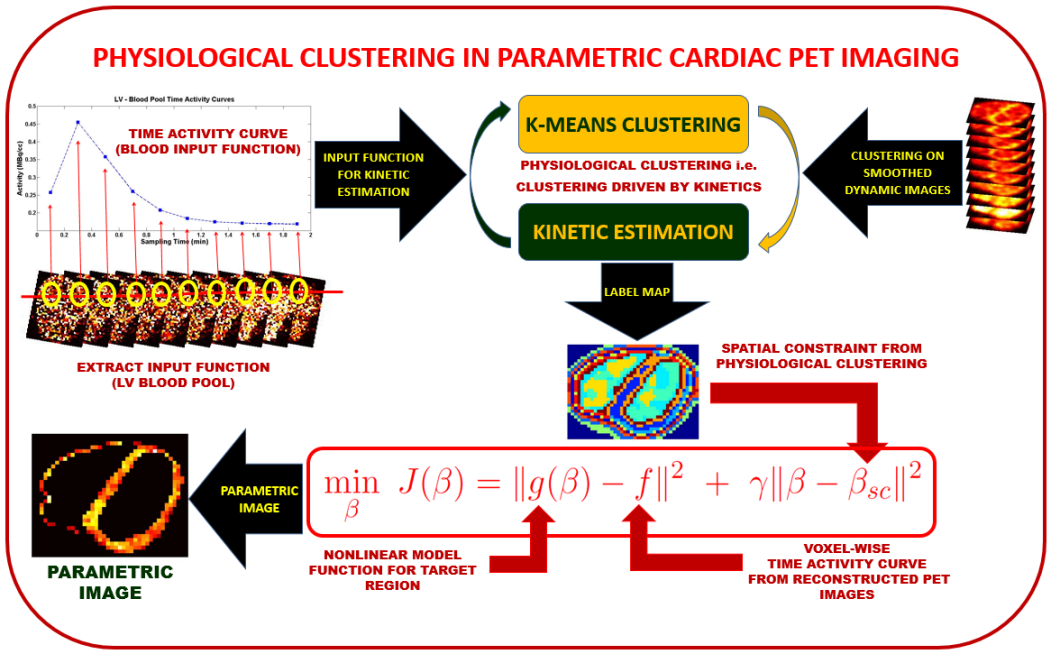

Figure 3.2: Flowchart of the proposed approach: Kinetic parameter estimation is formulated as a nonlinear least squares with spatial constraints problem (NLLS-SC) where spatial constraints are computed from a physiologically driven clustering of dynamic images. Physiological clustering of dynamic images is performed using K-means clustering with kinetic modeling in an iterative fashion. This gives a map of labels where each functionally homogeneous cluster is represented by mean kinetics (cluster centroid). Parametric images are acquired by solving the NLLS-SC problem for each voxel by penalizing spatial variations from mean kinetics. This substantially reduces noise in the estimation process for each voxel by utilizing kinetic information from physiologically similar voxels (cluster members). Resolution degradation may be substantially minimized as regression is performed on non-smoothed (raw) dynamic images.

3.3 Methods

3.3.1 Simulations

3.3.1.1 Perfusion Defects

Transmural and non-transmural perfusion defects were simulated at different locations along the LV wall using the NCAT phantom [228]. Figure 3.3 illustrates short-axis views of the perfusion defects and the corresponding parameters used to generate

the phantoms. Defects were simulated in stress images and were placed over the anterior-lateral and lateral-inferior regions.

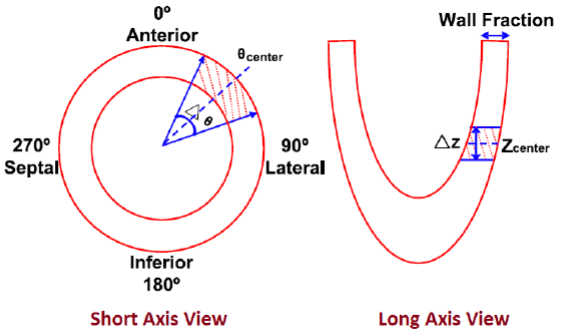

Perfusion Defect	Short Axis View	Parameters		Defect Type
A		Θ_{center}	90°	Transmural
		$\Delta\Theta$	60°	
		z_{center}	0.5	
		Δz	50 mm	
		Wall fraction	1	
B		Θ_{center}	90°	Non-Transmural
		$\Delta\Theta$	60°	
		z_{center}	0.5	
		Δz	50 mm	
		Wall fraction	0.75	

Figure 3.3: *(top)* Short-axis and long-axis views of the LV wall with the region of perfusion defect shaded. Cold defects are parameterized by (θ_{center}, $\triangle\theta$, z_{center}, $\triangle z$, and wall fraction). *(bottom)* Table shows the short-axis views of the simulated perfusion defects and the corresponding parameters used to generate the phantoms [229].

3.3.1.2 Simulation and Reconstruction

Original TACs were generated for five tissues (liver, lung, muscle, normally perfused myocardium, and myocardium defect) using realistic kinetic parameters and the one tissue-compartment model. Table 3.2 lists the kinetic parameters used in the simulations. Arterial blood fraction for the myocardial tissue was simulated as 25%. Figure 3.4 shows the noise free TACs for LV and RV input functions, normally per-

fused myocardium, and the perfusion defect.

The dynamic data set consisted of 32 time frames (24×5 secs, 4×20 secs, and 4×40 secs) for a total duration of 6 minutes. Analytic simulations were performed for the dynamic images utilizing 315 angular samples covering 180°, 323 radial bins with 2.26 mm spacing, and 47 axial bins with 3.27 mm spacing [230]. Reconstructions were performed utilizing $128 \times 128 \times 47$ voxels in the transaxial (x, y) and axial (z) directions, respectively, with voxel dimensions $3.27 \times 3.27 \times 3.27$ mm^3. Attenuation, normalization, randoms, scatter, and decay were also incorporated. For randoms and scatter, a uniform distribution was assumed in the projection space. Poisson noise was then added to generate 30 realizations of noisy dynamic sinograms which were reconstructed using the OSEM algorithm (3 iterations, 21 subsets) [39].

3.3.1.3 Parametric Imaging using Physiological Clustering

Physiological clustering was performed on post-smoothed reconstructed dynamic images to generate a set of spatial constraint vectors, one for each functional cluster. Three clusters were assumed a priori (background, normal myocardium, and perfusion defect). Parametric images were generated using non-smoothed reconstructed dynamic images and varying penalty parameter, $\gamma \in [0\ 1 \times 10^{-1}]$ (equation 3.7). $\gamma = 0$ corresponds to no spatial constraint (unconstrained minimization).

Table 3.2: Kinetic parameters used in simulation of cardiac PET images for ^{82}Rb radiotracer.

Tissue	K_1 (mL/min/g)	k_2 (1/min)
Liver	0.57	0.97
Lung	0.18	0.98
Muscle	0.06	0.21
Myocardium (rest)	0.70	0.16
Myocardium (stress)	1.48	0.32
Perfusion Defect (stress)	0.74	0.25

3.3.1.4 Parametric Imaging following Post-smoothing

To evaluate the efficacy of our approach we computed parametric images by first post-smoothing the reconstructed dynamic images to reduce noise followed by solving the following weighted nonlinear least squares problem using basis function method:

$$\hat{\boldsymbol{\beta}}_{ps} = \underset{\boldsymbol{\beta}}{\operatorname{argmin}} \|\boldsymbol{C_{meas}(t;\beta)} - \boldsymbol{C^{ps}_{PET}(t)}\|^2_{\boldsymbol{W}} \tag{3.8}$$

where $\boldsymbol{C}^{ps}_{PET}(t)$ denotes the voxel TAC from post-smoothed dynamic images. Post-smoothing was performed using Butterworth filter of order 4 and cutoff frequencies ranging from 0.2 cycle/cm to 1 cycle/cm (0.1 cycle/cm increments). Equation 3.8 is a special case of equation 3.7 when $\gamma = 0$ and $\boldsymbol{C}_{PET}(t) = \boldsymbol{C}^{ps}_{PET}(t)$.

3.3.1.5 Figures of Merit

We quantitatively analyzed parametric images (from physiological clustering, Section 3.3.1.3, and post-smoothing, Section 3.3.1.4) by computing the following figures

of merit [231]:

$$\text{Bias} = \frac{1}{N_p}\sum_{j\in ROI}\frac{|(\frac{1}{R}\sum_{i=1}^{R}\theta_{i,j}^{est}) - \theta_j^{true}|}{\theta_j^{true}} \tag{3.9}$$

$$\text{NSD} = \frac{1}{N_p}\sum_{j\in ROI}\frac{\sqrt{\frac{1}{R-1}\sum_{i=1}^{R}(\theta_{i,j}^{est} - \frac{1}{R}\sum_{i=1}^{R}\theta_{i,j}^{est})^2}}{\frac{1}{R}\sum_{i=1}^{R}\theta_{i,j}^{est}} \tag{3.10}$$

$$\text{RMSE} = \sqrt{\frac{\sum_{j=1}^{N_p}\sum_{i=1}^{R}(\theta_{i,j}^{est} - \theta_j^{true})^2}{N_p \times R}} \tag{3.11}$$

$$\text{Contrast} = \frac{\overline{\theta_N}}{\overline{\theta_D}} - 1 \tag{3.12}$$

where θ_j^{true} is the j^{th} voxel value of the true parametric image, $\theta_{i,j}^{est}$ is the j^{th} voxel value of the estimated parametric image from the i^{th} noise realization, R is the total number of noise realizations, and N_p is the total number of voxels in an ROI. Two ROIs were drawn on the normally perfused myocardium and the perfusion defect. Overall Bias, NSD, and RMSE were calculated by computing a weighted average of the ROI values (weighted by the size of the ROI). Contrast was calculated from the mean uptake values from the normal and defect regions, $\overline{\theta_N}$ and $\overline{\theta_D}$, respectively.

3.3.2 Clinical Studies

3.3.2.1 Patient Dataset

We studied 3 patients (2 males and 1 female) that underwent ^{82}Rb PET/CT scans for a rest-stress study. The average age of these patients was 65 ± 16 years, and the average weight of these patients was 182 ± 61 lbs. All patients had a history of CAD

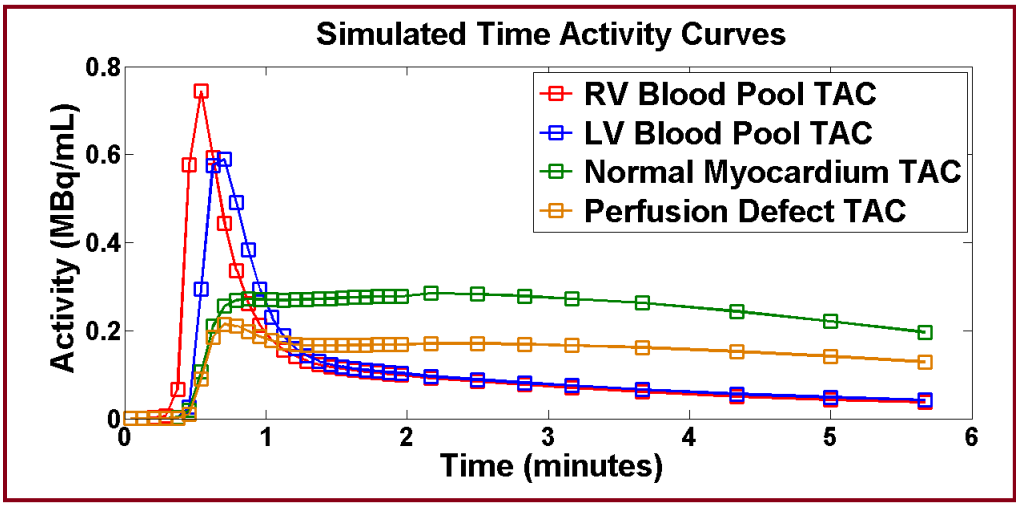

Figure 3.4: Noise-free TACs were generated using a one-tissue compartment model and the kinetic parameters specified in Table 3.2. LV and RV concentration curves were extracted from a clinical study and fitted with a multiexponential model [232] to generate finely sampled concentration time course. This plot shows TACs extracted from noise-free simulated dynamic images.

and showed perfusion defects along the inferior-lateral wall. Table 3.3 summarizes the characteristics of the clinical data.

3.3.2.2 PET/CT Protocol

Sinograms were acquired using a GE LYSO-crystal, 64-slice Discovery Rx VCT scanner. Subjects were positioned supine using a scout scan. This was followed by a low-dose CT scan (120 kV, 80 mA) with shallow breathing for attenuation correction of PET data. Using a large intravenous line, $35-50$ mCi of ^{82}Rb was infused at 50 ml/min over 30 seconds, and a list-mode 2-D PET scan was acquired for 8 minutes. After rest acquisition, subjects received 0.4 mg of A2A adenosine receptor agonist Regadenoson, infused intravenously over 10 seconds. Within 20 seconds of pharmacologic induced stress, a second dose of $35-50$ mCi of ^{82}Rb was injected followed by

another 8 minute acquisition of list-mode 2-D PET scan. Rest and stress PET data were registered with the CT scan and the latter was used for attenuation correction of PET data. Randoms and scatter corrections were also applied to the emission data. Dynamic sinograms were reconstructed using the OSEM algorithm (2 iterations, 21 subsets) into 32 dynamics frames (framing sequence: 20×6 secs, 5×12 secs, 4×30 secs, and 3×60 secs) where each frame is a $128 \times 128 \times 47$ matrix with a voxel volume of $3.27 \times 3.27 \times 3.27$ mm^3.

Table 3.3: Characteristics of the clinical dataset for ^{82}Rb radiotracer.
Notation: BP (mm-Hg): rest systolic/diastolic blood pressure - stress systolic/diastolic blood pressure, HR (bpm): rest heart rate - peak heart rate, and LVEF (%) : Left Ventricle Ejection Fraction (rest - stress).

No.	Gender	Age (years)	BP (mm-Hg)	HR (bpm)	Weight (lb)	LVEF (%)	Defect Type
1	M	64	116/69 - 103/55	80 - 146	172	30 - 42	Large fixed inferior wall defect
2	M	49	119/65 - 133/60	75 - 96	247	45 - 50	Fixed perfusion defect in lateral wall
3	F	81	98/61 - 120/62	59 - 162	126	29 - 32	Fixed large inferior-lateral wall defect

3.3.2.3 Parametric Imaging using Physiological Clustering

Physiological clustering was performed on post-smoothed reconstructed dynamic images to generate a set of spatial constraint vectors, one for each functional cluster. Three clusters were assumed a priori. Parametric images were generated using non-smoothed reconstructed dynamic images and varying penalty parameter, $\gamma \in [0\ 1 \times 10^{-1}]$ (equation 3.7). $\gamma = 0$ corresponds to no spatial constraint (unconstrained minimization).

3.3.2.4 Parametric Imaging following Post-smoothing

We also computed parametric images by performing weighted nonlinear regression (equation 3.8) on post-smoothed reconstructed dynamic images. Post-smoothing was performed using Butterworth filter of order 4 and cutoff frequencies ranging from 0.2 cycle/cm to 1 cycle/cm (0.1 cycle/cm increments).

3.3.2.5 Figures of Merit

We quantitatively analyzed parametric images (from physiological clustering, Section 3.3.2.3, and post-smoothing, Section 3.3.2.4) by computing Contrast-to-Noise ratio, CNR $= \frac{\text{contrast}}{\text{NSD}}$, where NSD and contrast are defined as follows:

$$\text{NSD} = \frac{\sqrt{\frac{1}{N_B-1}\sum_{i\in B}(\theta_i^{est} - \frac{1}{N_B}\sum_{i\in B}\theta_i^{est})^2}}{\frac{1}{N_B}\sum_{i\in B}\theta_i^{est}} \tag{3.13}$$

$$\text{Contrast} = \frac{\frac{1}{N_B}\sum_{i\in B}\theta_i^{est}}{\frac{1}{N_D}\sum_{i\in D}\theta_i^{est}} - 1 \tag{3.14}$$

θ_i^{est} is the i^{th} pixel value of the estimated parametric image, N_B is the number of pixels in the background ROI, B, and N_D is the number of pixels in the perfusion defect ROI, D.

3.4 Results

3.4.1 Simulations

We compared parametric images of uptake rate (K_1) obtained using the proposed approach of physiological clustering and the conventional approach of post-smoothing. In physiological clustering approach, we varied the penalty parameter, γ, from 0 to 1×10^{-1} and in post-smoothing approach, we varied the cutoff frequency of the Butterworth filter, w_{cutoff}, from 0.2 cycles/cm to 1 cycles/cm.

3.4.1.1 Transmural Perfusion Defect

Figure 3.5 shows that with decreasing values of w_{cutoff}[1], and increasing values of γ, for the conventional post-smoothing and proposed physiological clustering methods, respectively, noise is considerably reduced in K_1 parametric images. In the post-smoothing approach, at lower cut-off frequencies typically encountered in clinical settings ($w_{\text{cutoff}} \leq 0.5$ cylces/cm), the images are blurred especially around the septal, anterior-lateral and lateral-inferior regions of the myocardium. By comparison, visual (qualitative) assessment reveals that the proposed approach produces sharper images with increased noise reduction. Increasing γ values increasingly penalize deviations of voxel estimates from spatial constraints which utilize kinetic information from physiologically similar voxels. This considerably reduces noise with reduced mixing

[1] Lower w_{cutoff} (i.e. smaller value) in the Butterworth filter corresponds to higher smoothing.

of information from functionally heterogeneous regions.

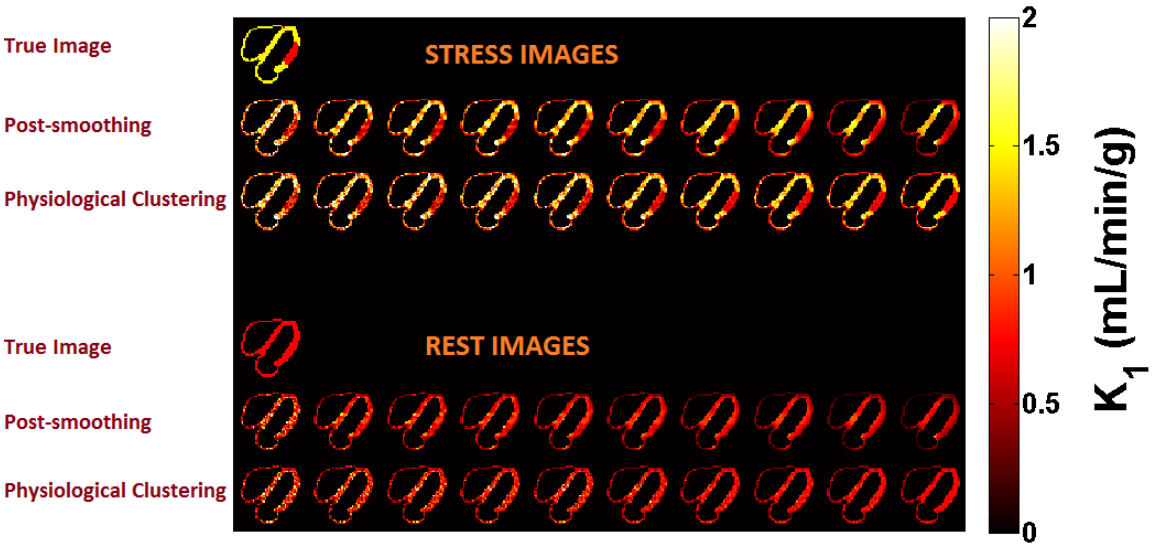

Figure 3.5: K_1 *parametric images:* we show K_1 images from rest-stress simulation. Perfusion defect was placed along the lateral myocardium wall in stress images. For each set of images we show: *(Row 1)* true K_1 image, *(Row 2)* K_1 images obtained from post-smoothed dynamic images with varying cutoff frequencies: *(L-to-R)* $w_{\text{cutoff}} = 0, 1, 0.9, 0.8, 0.7, 0.6, 0.5, 0.4, 0.3,$ and 0.2 cycles/cm where $w_{\text{cutoff}} = 0$ corresponds to no post-smoothing, and *(Row 3)* K_1 images obtained from physiological clustering approach by varying the penalty parameter: *(L-to-R)* $\gamma = 0, 1 \times 10^{-5}, 5 \times 10^{-5}, 8 \times 10^{-5}, 1{\times}10^{-4}, 3{\times}10^{-4}, 6{\times}10^{-4}, 9{\times}10^{-4}, 1{\times}10^{-3},$ and $1{\times}10^{-2}$ where $\gamma = 0$ corresponds to no spatial constraint. $w_{\text{cutoff}} = 0$ and $\gamma = 0$ are identical scenarios which involve weighted nonlinear regression on raw dynamic images (as seen from equations 3.7 and 3.8).

For quantitative analysis, Figure 3.6 shows plots of overall noise (NSD) versus overall bias for the K_1 parametric images for both rest (left) and stress (stress) MP simulations. Clearly, enhanced quantitative noise vs. bias performance is observed for the proposed framework. Table 3.4 also highlights key numerical performance of the two approaches in comparison to baseline parametric imaging ($w_{\text{cutoff}} = 0$ and $\gamma = 0$). For instance, in the case of rest imaging at optimal performance (i.e. minimum overall RMSE), post-smoothing gave an overall NSD reduction of $\sim 31\%$

at a cost of $\sim$ 1% increase in overall bias ($\sim$ 50% reduction in overall RMSE) while the physiological clustering approach gave an NSD reduction of $\sim$ 35% and bias reduction of $\sim$ 5% ($\sim$ 61% reduction in overall RMSE). In stress simulations, at optimal performance (minimum overall RMSE), post-smoothing approach gave an overall NSD reduction of $\sim$ 28% at a cost of $\sim$ 4% increase in overall bias ($\sim$ 38% reduction in overall RMSE) while physiological clustering approach gave an overall NSD reduction of $\sim$ 30% at a cost of $\sim$ 1% increase in overall bias ($\sim$ 46% reduction in overall RMSE). Thus, by comparison, physiological clustering resulted in superior quantitative accuracy by substantially reducing the overall RMSE ($\sim$ 11% and 8% further reduction in rest and stress images, respectively, compared to post-smoothing) without degrading resolution ($\sim$ 1% increase in overall estimation bias). We also computed CNR in stress uptake images (where perfusion defect was present) and found that physiological clustering, compared to post-smoothing approach, resulted in a higher CNR (13.7 as opposed to 7.2) at optimal performance.

We also studied the quantitative performance of the two approaches at the ROI level. Figure 3.7 shows the NSD versus bias curves for each of the normal myocardium and the perfusion defect. Clearly enhanced noise vs. bias trade-off performance is observed for the proposed framework. Numerical comparisons between the two approaches are summarized in Table 3.5 for both ROIs. In the normal myocardium, at optimal performance (minimum regional RMSE), post-smoothing gave an NSD reduction of $\sim$ 27% at a cost of $\sim$ 5.6% increase in bias ($\sim$ 36% reduction in RMSE)

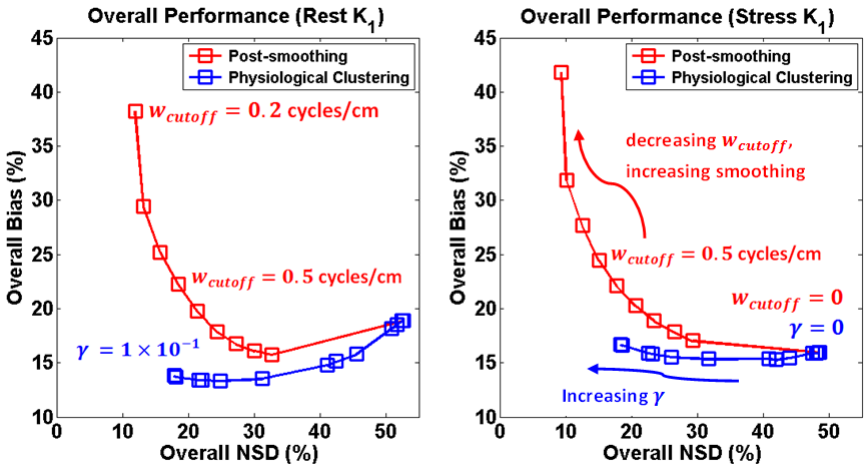

Figure 3.6: *Transmural perfusion defect:* plots of overall NSD versus overall bias comparing the K_1 parametric images obtained from post-smoothing approach and physiological clustering approach. Points on the post-smoothing curve correspond to different cutoff frequencies of Butterworth filter (w_{cutoff}) and points on the physiological clustering curve correspond to different values of penalty parameter (γ). $w_{\text{cutoff}} \leq 0.5$ cycles/cm are typically found in clinical settings [233, 234].

while physiological clustering approach gave an NSD reduction of $\sim 31\%$ at a cost of $\sim 4.6\%$ increase in bias ($\sim 43\%$ reduction in regional RMSE). In the perfusion defect region, at optimal performance (minimum regional RMSE), post-smoothing gave an NSD reduction of $\sim 42\%$ at a cost of $\sim 2.1\%$ increase in bias ($\sim 56\%$ reduction in regional RMSE) and physiological clustering approach gave an NSD reduction of $\sim 41\%$ and a bias reduction of $\sim 11\%$ ($\sim 68\%$ reduction in regional RMSE). This analysis demonstrates the efficacy of physiological clustering approach in substantially reducing noise and bias in the perfusion defect: the latter is related to the presence of noise-induced bias in non-linear estimation tasks [235], which can result in bias reduction when noise is handled more appropriately.

To quantify the ability to resolve perfusions defect, we studied CNR as a function of w_{cutoff} and γ for the post-smoothing physiological clustering approaches, respec-

Table 3.4: *Transmural perfusion defect:* summary of the quantitative performance of physiological clustering and post-smoothing approaches, compared to the baseline (no processing; $w_{\text{cutoff}} = 0$ and $\gamma = 0$). We include results for $w_{\text{cutoff}} = 0.5$ cycles/cm and $w_{\text{cutoff}} = 0.3$ cycles/cm which are typically found in clinical settings and may not be the optimal value [233, 234].
Note: optimal performance parameter(s) are highlighted in blue color.
Abbreviations: Inc. - Increase, Red. - Reduction, Post-smooth. - Post-smoothing, Phys. Clust. - Physiological Clustering

		Quantitative Metrics: Rest			
Methodology	Parameter	Bias Inc. (%)	NSD Red. (%)	RMSE Red. (%)	CNR
Post-smooth.	0.3 cycles/cm	10.5	40	40.3	-
	0.5 cycles/cm	3.3	34	49	-
	0.6 cycles/cm	1	31	50	-
Phys. Clust.	1×10^{-2}	-5.1	34.8	61.2	-

		Quantitative Metrics: Stress			
Methodology	Parameter	Bias Inc. (%)	NSD Red. (%)	RMSE Red. (%)	CNR
Post-smooth.	0.3 cycles/cm	15.6	37.8	22.2	9.9
	0.5 cycles/cm	8.4	33	34.3	9
	0.7 cycles/cm	3.9	27.5	38.2	7.2
Phys. Clust.	4×10^{-3}	1.2	32.6	46	13.7

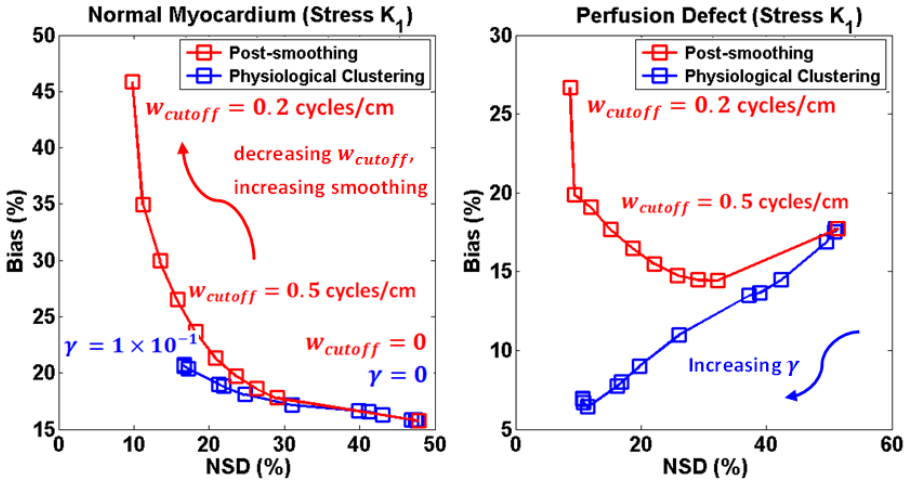

Figure 3.7: *Transmural Perfusion Defect:* Regional NSD versus bias curves for K_1 parametric images obtained from post-smoothing approach and physiological clustering approach. Points on the post-smoothing curve correspond to different cutoff frequencies of Butterworth filter (w_{cutoff}) and points on the physiological clustering curve correspond to different values of penalty parameter (γ). $w_{\text{cutoff}} \leq 0.5$ cycles/cm are typically found in clinical settings.

Table 3.5: *Transmural Perfusion Defect:* Summary of the quantitative performance of physiological clustering and post-smoothing approaches in the two ROIs: normal myocardium and perfusion defect. In the normal myocardium the optimal parameter values were $w_{\text{cutoff}} = 0.7$ cycles/cm and $\gamma = 4 \times 10^{-3}$ and in the perfusion defect the optimal parameter values were $w_{\text{cutoff}} = 0.3$ cycles/cm and $\gamma = 1 \times 10^{-2}$. Optimal parameters correspond to minimum regional RMSE.

	Quantitative Metrics: Normal Myocardium		
Methodology	Bias Increase (%)	NSD Reduction (%)	RMSE Reduction (%)
Post-smoothing	5.6	27	36.1
Physiological Clustering	4.6	30.7	42.8

	Quantitative Metrics: Perfusion Defect		
Methodology	Bias Increase (%)	NSD Reduction (%)	RMSE Reduction (%)
Post-smoothing	2.1	42	56.2
Physiological Clustering	11	40.6	68.3

tively. Figure 3.8 depicts plots for RMSE versus CNR as well as bias versus CNR. At higher CNR (≥ 3), physiological clustering, compared to post-smoothing, resulted in K_1 parametric images with significantly lower RMSE and estimation bias. With decreasing w_{cutoff} (especially $w_{\text{cutoff}} \leq 0.5$ cycles/cm as commonly encountered in clinical practice), the estimation bias (and RMSE) were severely degraded resulting in unstable K_1 parametric estimates. On the contrary, physiological clustering resulted in improved CNR without aggravating RMSE and estimation bias. Doubling the CNR (from ~ 5 to 10) was at the cost of 11% increase in estimation bias and 3.6% increase in RMSE for post-smoothing, while this was at a cost of $< 1\%$ increase in estimation bias and an actual improvement of 8% in RMSE in the proposed framework. This analysis demonstrates that the proposed approach of physiological clustering can better resolve perfusion defects without compromising the robustness of the esti-

mated K_1 parametric images, both of which are important in clinical decision making (diagnosis, prognosis and treatment response assessment).

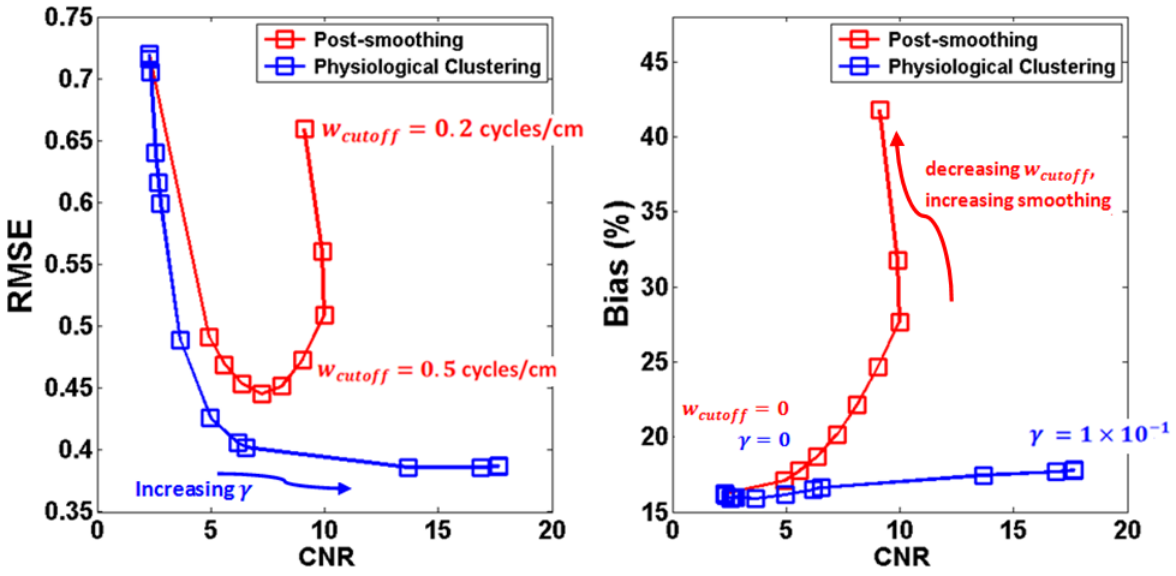

Figure 3.8: *(Left)* RMSE versus CNR and *(Right)* bias versus CNR curves for post-smoothing approach and physiological clustering approach. Points on the post-smoothing curve correspond to different cutoff frequencies of Butterworth filter (w_{cutoff}) and points on the physiological clustering curve correspond to different values of penalty parameter (γ). In both plots, the left-most point corresponds to $w_{\text{cutoff}} = 0$ and $\gamma = 0$.

3.4.1.2 Non-Transmural Perfusion Defect

We evaluated qualitative and quantitative performance for non-transmural perfusion defect placed along the lateral myocardium wall (wall fraction = 0.75, Figure 3.3). The defect was only simulated in stress images and, hence, we focus on stress uptake parametric images (Figure 3.9) obtained using post-smoothing and physiological clustering approaches.

Figure 3.9 shows that with increasing values of γ and decreasing values of w_{cutoff} noise is considerably reduced in K_1 parametric images. However, in the post-smoothing

approach, it becomes increasingly difficult to distinguish between transmural and non-transmural perfusion defects due to mixing of kinetic information from heterogeneous voxels on the boundary of the defect. At lower cutoff frequencies typically encountered in clinical settings ($w_{\text{cutoff}} \leq 0.5$ cycles/cm), the images are blurred specially around the septal, the anterior-lateral, and the lateral-inferior regions of the myocardium. On the contrary, the physiological clustering approach is able to resolve the non-transmural perfusion defect by only utilizing kinetic information from homogenous voxels to reduce noise.

Figure 3.9: K_1 *Parametric Images:* We show uptake images from stress simulation. Non-transmural perfusion defect was placed along the lateral myocardium wall (wall fraction = 0.75, Figure 3.3). We show: *(Row 1)* true K_1 image, *(Row 2)* K_1 images obtained from post-smoothed dynamic images with varying cutoff frequencies: (L-to-R) $w_{\text{cutoff}} = 0, 1, 0.9, 0.8, 0.7, 0.6, 0.5, 0.4, 0.3$, and 0.2 cycles/cm where $w_{\text{cutoff}} = 0$ corresponds to no post-smoothing, and *(Row 3)* K_1 images obtained from physiological clustering approach by varying the penalty parameter: (L-to-R) $\gamma = 0, 1 \times 10^{-5}, 5 \times 10^{-5}, 8 \times 10^{-5}, 1 \times 10^{-4}, 3 \times 10^{-4}, 6 \times 10^{-4}, 9 \times 10^{-4}, 1 \times 10^{-3}$, and 1×10^{-2} where $\gamma = 0$ corresponds to no spatial constraint. $w_{\text{cutoff}} = 0$ and $\gamma = 0$ are identical scenarios which involve weighted nonlinear regression on raw dynamic images (as seen from equations 3.7 and 3.8)

Figure 3.10 shows plots of overall NSD versus overall bias for the K_1 parametric images. At optimal performance (minimum overall RMSE), post-smoothing gave an overall NSD reduction of $\sim 28\%$ at a cost of $\sim 4.7\%$ increase in overall bias ($\sim 37\%$ reduction in overall RMSE) while physiological clustering approach gave an overall

NSD reduction of $\sim 33\%$ at a cost of $\sim 3.0\%$ increase in overall bias ($\sim 47\%$ reduction in overall RMSE). Physiological clustering approach showed superior quantitative accuracy by substantially reducing the overall RMSE ($\sim 10\%$ reduction compared to post-smoothing approach) with minimal resolution degradation ($\sim 3\%$ increase in overall estimation bias). We also computed CNR and found that physiological clustering, compared to post-smoothing approach, resulted in a higher CNR (11.3 as opposed to 5.7) at optimal performance (minimum overall RMSE). Table 3.6 summarizes the quantitative performance of the two approaches for non-transmural perfusion defect.

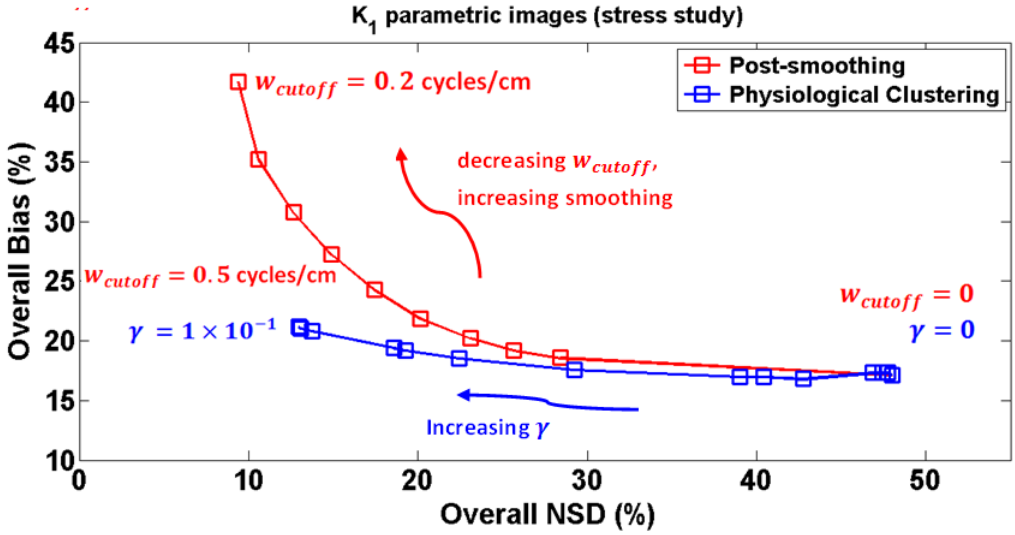

Figure 3.10: *Non-Transmural Perfusion Defect:* Plots of overall NSD versus overall bias comparing the K_1 parametric images obtained from post-smoothing approach and physiological clustering approach. Points on the post-smoothing curve correspond to different cutoff frequencies of Butterworth filter (w_{cutoff}) and points on the physiological clustering curve correspond to different values of penalty parameter (γ).

Quantitative performance of the two approaches at the ROI level is also depicted in Figure 3.11 for the normal myocardium and the perfusion defect. As before, Ta-

Table 3.6: *Non-Transmural Perfusion Defect:* Summary of the quantitative performance of physiological clustering and post-smoothing approaches. We include results for $w_{\text{cutoff}} = 0.5$ cycles/cm and $w_{\text{cutoff}} = 0.3$ cycles/cm which are typically found in clinical settings and may not be the optimal value.
Note: optimal performance parameter(s) are highlighted in blue color.
Abbreviations: Inc. - Increase, Red. - Reduction, Post-smooth. - Post-smoothing, Phys. Clust. - Physiological Clustering

		Quantitative Metrics: Stress			
Methodology	Parameter	Bias Inc. (%)	NSD Red. (%)	RMSE Red. (%)	CNR
Post-smooth.	0.3 cycles/cm	18.1	37.4	17.8	2.3
	0.5 cycles/cm	10.1	33.1	31.3	5.3
	0.7 cycles/cm	4.7	27.8	36.9	5.7
Phys. Clust.	4×10^{-3}	3	33.4	47.1	11.3

ble 3.7 also shows numerical comparison between the two approaches. Overall, the results demonstrate the efficacy of the physiological clustering approach in enabling substantially enhanced noise vs. bias quantitative performance in the non-transmural perfusion defect.

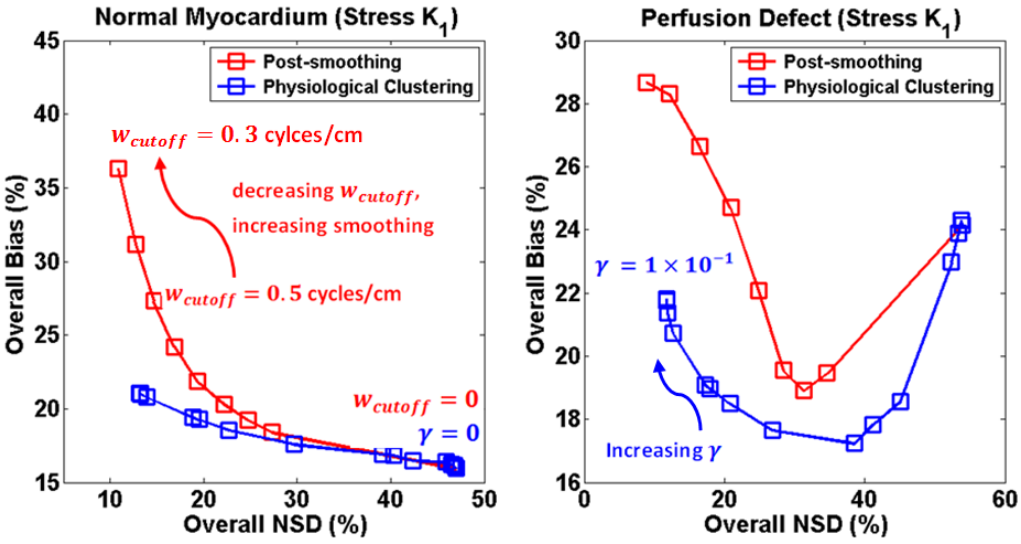

Figure 3.11: *Non-Transmural Perfusion Defect:* Regional NSD versus bias curves for K_1 parametric images obtained from post-smoothing approach and physiological clustering approach. Points on the post-smoothing curve correspond to different cutoff frequencies of Butterworth filter (w_{cutoff}) and points on the physiological clustering curve correspond to different values of penalty parameter (γ).

Table 3.7: *Non-Transmural Perfusion Defect:* Summary of the quantitative performance of physiological clustering and post-smoothing approaches in the two ROIs: normal myocardium and perfusion defect. In the normal myocardium the optimal parameter values were $w_{\text{cutoff}} = 0.7$ cycles/cm and $\gamma = 1 \times 10^{-2}$ and in the perfusion defect the optimal parameter values were $w_{\text{cutoff}} = 0.3$ cycles/cm and $\gamma = 4 \times 10^{-3}$. Optimal parameters correspond to minimum regional RMSE.

	Quantitative Metrics: Normal Myocardium		
Methodology	Bias Increase (%)	NSD Reduction (%)	RMSE Reduction (%)
Post-smoothing	5.9	27.6	35.8
Physiological Clustering	5	33.7	44.9

	Quantitative Metrics: Perfusion Defect		
Methodology	Bias Increase (%)	NSD Reduction (%)	RMSE Reduction (%)
Post-smoothing	4.5	50	51.7
Physiological Clustering	-3.4	33.1	57.7

Figure 3.12 shows plots for RMSE versus CNR as well as bias versus CNR. In physiological clustering approach, as the CNR doubled from 5 to 10, RMSE was improved from 44% to 6% and the estimation bias increased from 2.3% to 3.4%. However, with post-smoothing, the achievable CNR was less than six (CNR < 6), and the RMSE and bias performance was clearly degraded in comparison to the physiological clustering approach.

3.4.2 Patient Dataset

We compared, qualitatively and quantitatively, parametric images of stress uptake rate (K_1) obtained using the proposed approach of physiological clustering and the conventional approach of post-smoothing. Figure 3.13 shows summed stress uptake images for three ^{82}Rb PET patient studies. The characteristics of the dataset are

described in Table 3.3. In the clinic, post-smoothed reconstructed dynamic images are summed to generate a static image with a higher SNR. This gives better visualization of normal uptake regions and perfusion defects. However, this analysis is qualitative and does not result in voxel-wise parametric images. Figure 3.14 shows that with increasing values of γ and decreasing values of w_{cutoff} noise is considerably reduced in K_1 parametric images. However, compared to post-smoothing approach, physiological clustering is able to resolve the perfusion defects without blurring the region of normal uptake at the interface of the defect.

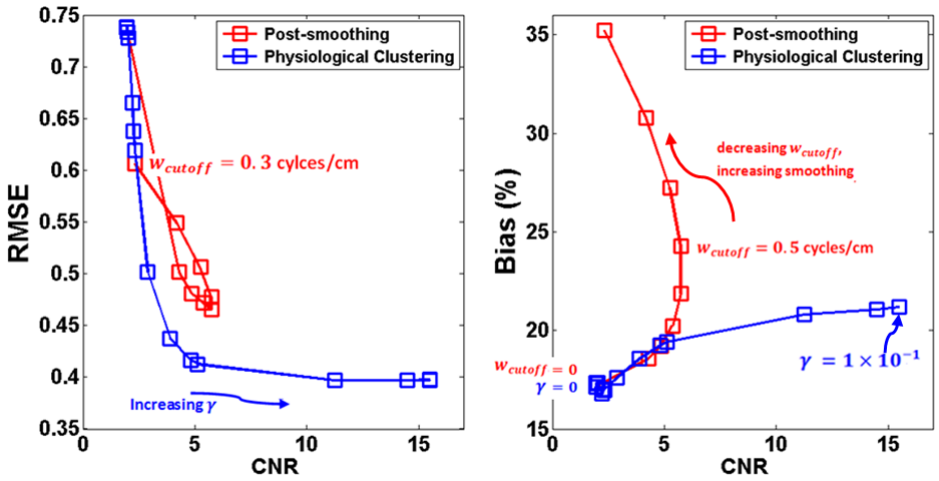

Figure 3.12: *(Left)* RMSE versus CNR and *(Right)* bias versus CNR curves for post-smoothing approach and physiological clustering approach. Points on the post-smoothing curve correspond to different cutoff frequencies of Butterworth filter (c) and points on the physiological clustering curve correspond to different values of penalty parameter (γ). In both plots, the left-most point corresponds to $w_{\text{cutoff}} = 0$ and $\gamma = 0$.

For quantitative comparison, Figure 3.15 depicts uptake rate (K_1) versus CNR for the two approaches in normally perfused region and perfusion defect. Physiological clustering outperformed post-smoothing approach in the sense that for a given uptake rate, higher CNR was obtained. In post-smoothing approach, with decreasing

w_{cutoff}, the uptake rate deteriorates even for normal myocardium which is attributed to the heterogeneous mixing of voxels at the interface of the perfusion defect. On the contrary, physiological clustering approach is able to resolve the perfusion defect with substantial noise reduction resulting in a higher CNR. These results demonstrate the efficacy of physiological clustering approach on clinical data.

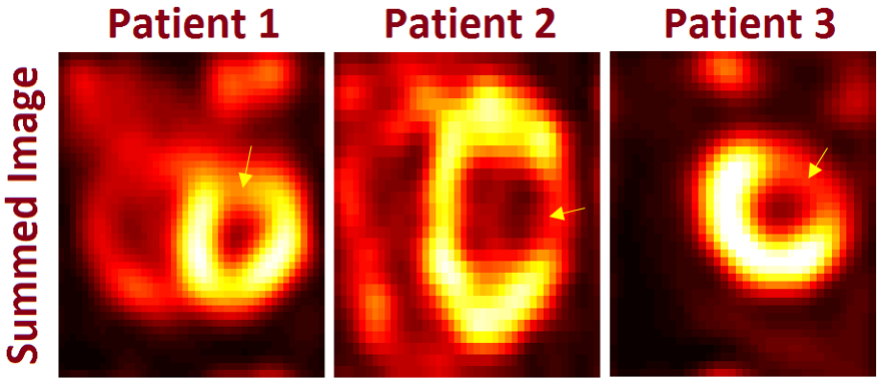

Figure 3.13: Short-axis slices of summed stress uptake images for three patient studies. Yellow arrows point to the perfusion defects. *Note: These are not parametric images but just the sum of post-smoothed dynamic images.*

3.5 Discussion

3.5.1 K-means Clustering Algorithm

We used the K-means clustering algorithm to segment dynamic PET images into functionally homogeneous clusters. K-means clustering, though extremely simple and straightforward, is sensitive to the initialization of representative TACs due to non-convex objective function, requires *a priori* specification of number of clusters, and the similarity metric does not incorporate spatial proximity of voxels. We discuss

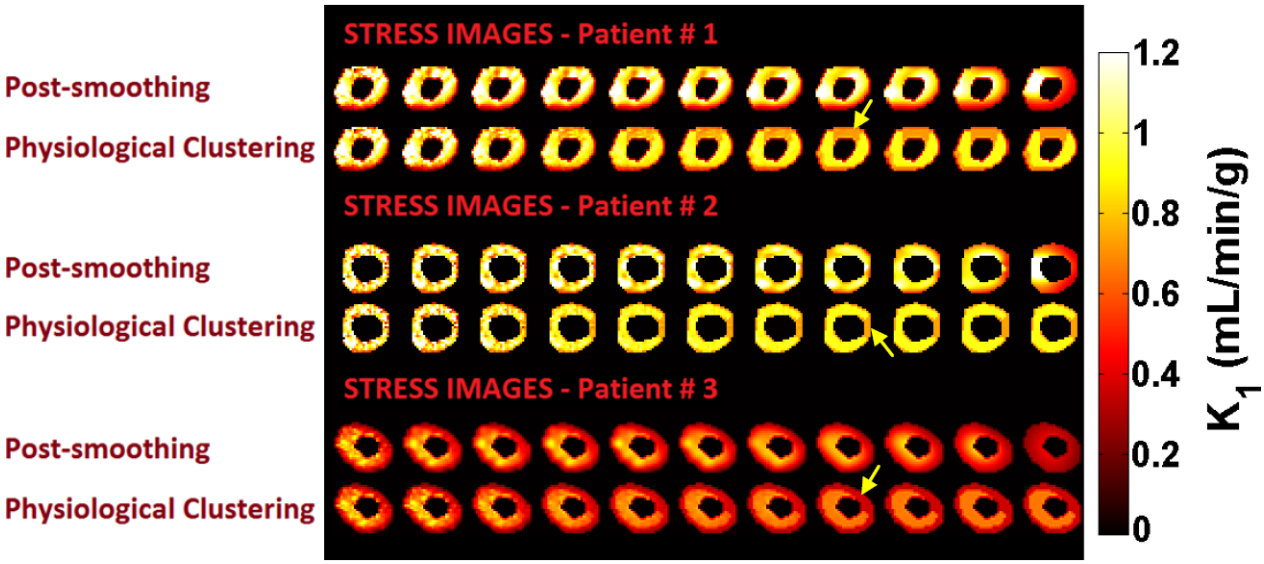

Figure 3.14: K_1 *Parametric Images:* We show short-axis views of stress uptake images from three patient studies. For the post-smoothing approach, K_1 images were obtained by varying cutoff frequencies: (L-to-R) $w_{\text{cutoff}} = 0, 1, 0.9, 0.8, 0.7, 0.6, 0.5, 0.4, 0.3, 0.2$, and 0.1 cycles/cm where $w_{\text{cutoff}} = 0$ corresponds to no post-smoothing, and, for physiological clustering approach K_1 images were obtained by varying the penalty parameter: (L-to-R) $\gamma = 0, 2 \times 10^{-6}, 5 \times 10^{-6}, 1 \times 10^{-5}, 5 \times 10^{-5}, 8 \times 10^{-5}, 1 \times 10^{-4}, 3 \times 10^{-4}, 6 \times 10^{-4}, 9 \times 10^{-4}$, and 1×10^{-3} where $\gamma = 0$ corresponds to no spatial constraint. Perfusion defects are shown by yellow arrows.

these aspects below and plan to pursue and carefully study them in future work.

3.5.1.1 Sensitivity to initialization of clusters

Non-convexity can be addressed by a convex relaxation of the K-means objective function [236, 237]:

$$\min_{\boldsymbol{U}} F_\rho(\boldsymbol{U}) \triangleq \frac{1}{2} \sum_{i=1}^{p} \|\boldsymbol{TAC}_i - \boldsymbol{u}_i\|_{\boldsymbol{W}}^2 + \rho \sum_{i<j} w_{i,j} \|\boldsymbol{u}_i - \boldsymbol{u}_j\|_1 \tag{3.15}$$

where p is the number of voxels, ρ is a tuning parameter, $w_{i,j}$ is a non-negative weight, and the i^{th} column of matrix $\boldsymbol{U}$ (i.e. u_i) is the cluster centroid for voxel i.

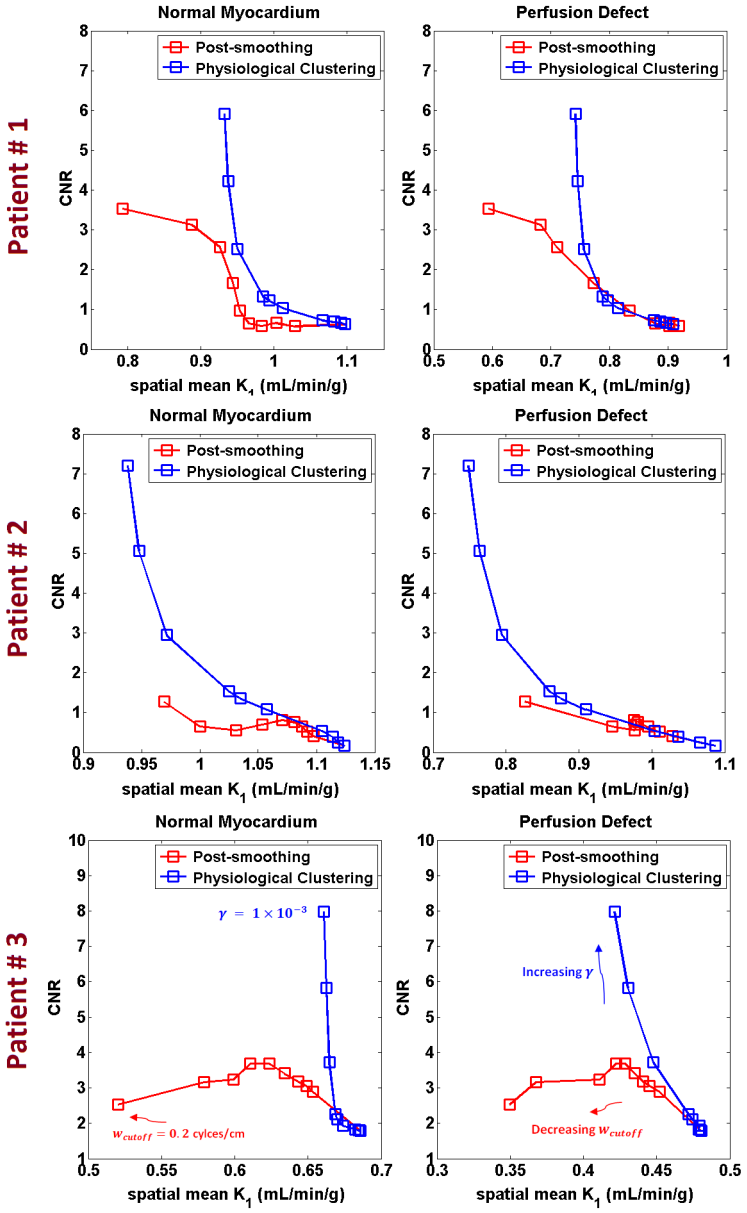

Figure 3.15: CNR versus uptake rate curves for post-smoothing approach and physiological clustering approach. Points on the post-smoothing curve correspond to different cutoff frequencies of Butterworth filter (w_{cutoff}) and points on the physiological clustering curve correspond to different values of penalty parameter (γ). In both plots, the right-most point corresponds to $w_{\text{cutoff}} = 0$ and $\gamma = 0$. Uptake rates were computed in a small ROI (~ 20 voxels) in the vicinity of the perfusion defect.

An interesting aspect of this convexification is that it obviates the need of predefining number of clusters at the cost of fixing the tuning parameter ρ. Voxels i and j belong

to the same cluster if $u_i = u_j$. When $\rho = 0$, $u_i \neq u_j$, $\forall\ i, j$ and there are p singleton clusters, and when ρ is sufficiently high, all voxels amalgamate into a single cluster. Equation 3.15 can be solved using the ADMM algorithm [238].

3.5.1.2 Number of Clusters

For simulations, we chose the true number of clusters ($N = 3$) in Algorithm 3, and for clinical studies, we also chose three clusters ($N = 3$) after carefully visualizing the summed dynamic images with the help of a resident. We quantitatively analyzed simulated stress uptake images obtained using the physiological clustering approach with varying number of clusters, $N = 3, 5, 8$, and 11. Figure 3.16 shows the percentage reductions achieved in overall NSD, bias, and RMSE in the estimated K_1 parametric images. For $N = 3$ and 5, the quantitative performance is almost similar ($< 2\%$ difference) but, for $N = 8$ and 11, the performance degrades further by $> 5\%$. Overall, it was observed that in MP PET imaging, the performance is less sensitive to the number of clusters than in whole brain imaging [239], which is understandable given the greater number of distinct regions in the latter. Some variability in the quantitative performance is attributed to random initializations of the clustering algorithm as discussed before. Apart from the initialization of the clustering algorithm, choosing a very large number of clusters may lead to sub-optimal quantitative performance as shown in Figure 3.16. Estimating the true number of clusters is a common problem in clustering algorithms and there exist a number of efforts to address this

issue e.g. Akaike information criterion [240] or Bayesian information criterion [241], cross-validation [242] etc.

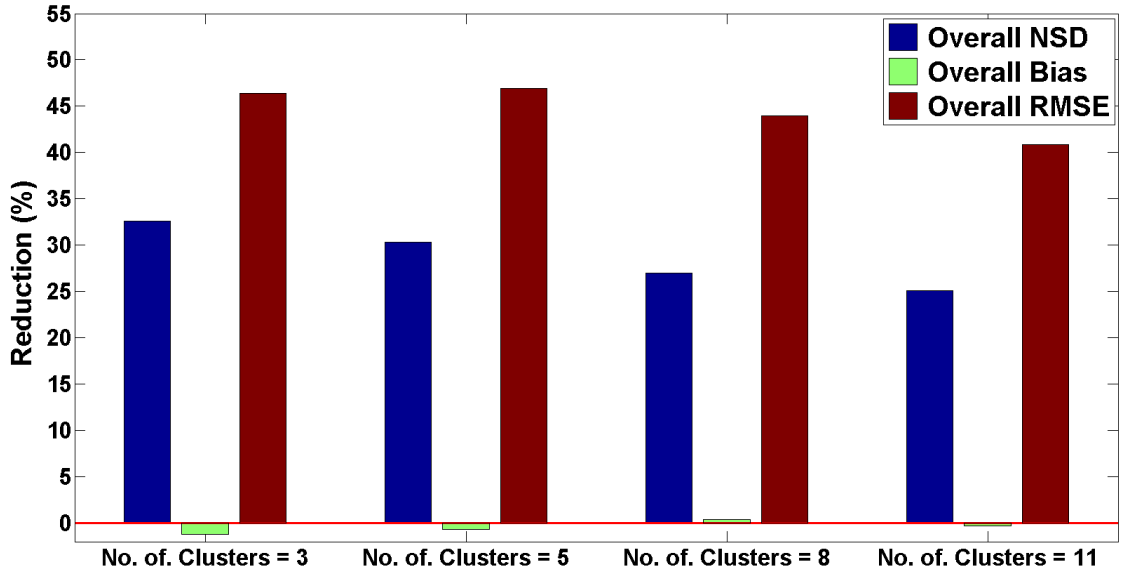

Figure 3.16: A bar graph showing percentage reduction achieved in overall NSD, bias, and RMSE by varying the number of clusters in the physiological clustering process.

3.5.1.3 Spatially Proximity of Voxels

The similarity metric in equation 3.5 can be modified to account for spatial proximity of voxels. Such metrics are found in normalized cuts and spectral clustering algorithms [243, 244]:

$$S_{Spec.\ Clust.}(i,j) = exp\left(-\frac{\|\boldsymbol{TAC}_i - \boldsymbol{TAC}_j\|_W^2}{\sigma_{TAC}^2}\right) exp\left(-\frac{\|\boldsymbol{X}_i - \boldsymbol{X}_j\|_2^2}{\sigma_X^2}\right) \quad (3.16)$$

for $\|\boldsymbol{X}_i - \boldsymbol{X}_j\|_2 < r$ where $\boldsymbol{X}_i$ is the spatial coordinate of voxel i. Incorporating spatial coordinates of voxels in the similarity metric encourages contiguous clusters,

which is physiologically more plausible; however, this benefit comes at the cost of optimizing an additional parameter (σ_X), which we intend to study.

In our simulations, we randomly sampled the myocardium to select representative TACs to initialize the clustering process (Step 3, Algorithm 3). Hence, parametric images obtained from the proposed approach of physiological clustering are not only robust to high noise-levels in the voxel TACs but also robust to the inherent variability in the clustering across multiple noise realizations. At the same time, it is plausible that incorporating the afore-mentioned features in the clustering algorithm or utilizing a specialized clustering technique could lead to further enhanced performance.

3.5.2 Image Derived Input Function

In our experiments, we extracted the input functions by manually placing an elliptical ROI in the LV and RV blood pools. There are several approaches in the scientific literature which automatically extract the input functions from dynamic PET images e.g. utilizing factor analysis (FA) [245], non-negative matrix factorization (NMF) [246], and independent component analysis (ICA) [191]. The basic theme underlying these approaches is shared. The dynamic data set (A) is factorized into a product of factor images (W) and coefficient matrix (H):

$$A_{N\times M} = W_{N\times r} H_{r\times M} \tag{3.17}$$

where r is the number of factors chosen a priori, N is the number of voxels, and M is the number of dynamic frames. The rows of H matrix provide the TACs for the r factors. In MP PET imaging, $r = 3$ (RV, LV, and myocardium). A shortcoming of these splitting techniques is the non-uniqueness of the solution matrices (W and H), upto a rotation matrix Q, as shown below [247, 248]:

$$A = (WQ^{-1})(QH) = \tilde{W}\tilde{H} \tag{3.18}$$

where W, H, $\tilde{W}$, and $\tilde{H}$ are nonnegative matrices. Non-uniqueness in FA is addressed by imposing minimal structure overlap (MSO) constraint as implemented in generalized FA for dynamic sequences (GFADS) [190]. NMF is preferred over GFADs which uses conjugate gradient algorithm as opposed to simple multiplicative/additive update equation in NMF [249]. Automatically extracted input functions using matrix factorization techniques may further enhance performance of the proposed approach.

3.5.3 Resolution Degrading Factors

Spatial resolution of ^{82}Rb PET images is impacted by the high positron range, photon non-collinearity and inter-crystal scattering [76, 250, 251]. Resolution is further degraded due to patient motion (cardiac motion, respiratory motion, and bulk motion) [252]. It has been shown before [253] that these degrading factors resulted in $\sim$ 48% underestimation of myocardial activity, leading to inaccurate estimates of parametric images; however, when correcting for all degrading effects (including mo-

tion) except for ^{82}Rb positron range, $\sim$ 23% underestimation continued to remain. A thorough comparison of the impact of various correction methods for resolution degradation, including post-reconstruction PVC [254] and reconstruction-based resolution modeling (RM) [83] on MP PET parametric imaging remains to be performed.

In our proposed approach of physiological clustering, kinetic parameters are estimated from pre-smoothed dynamic images which influence the accuracy of the estimated parameters. This reinforces the need of incorporating resolution modeling and appropriate motion correction schemes in the reconstruction process to obtain high quality perfusion images which may lead to more accurate parametric images.

3.5.4 Direct 4-D Parametric Imaging

Direct 4-D parametric imaging reduces noise in the parametric images by incorporating kinetic modeling within the image reconstruction framework. There have been a few approaches to this in the specific context of MP PET imaging. Rakvongthai et. al., [255] proposed a direct 4-D reconstruction method solved using preconditioned conjugate gradient to estimate uptake rate images for ^{18}F-Flurpiridaz radiotracer. Rahmim et al., [256] used numerical methods with optimization transfer approach to estimate K_1 parametric images for ^{82}Rb radiotracer. Su et al., [231], used a modified EM method to estimate K_1 parametric images for ^{13}N-Ammonia radiotracer. Quadratic penalty function is commonly employed to minimize intensity differences between neighboring voxels in the image space [255]. Future work involves incorpo-

rating cluster-based priors, such as utilized in the present work, within the direct 4-D reconstruction to obtain substantial noise reduction at the cost of minimal increase in bias.

3.6 Conclusions

Parametric imaging based on physiological clustering clearly outperforms conventional parameter estimation techniques by producing images with higher SNR. It substantially reduces noise with minimal increase in bias by utilizing kinetic information from physiologically similar voxels. Functionally similar voxels are binned in the same cluster with each cluster represented by mean kinetics. The mean kinetic information for each cluster is enforced as a spatial constraint in the voxel-wise parameter estimation process thereby forcing (by tuning the penalty parameter γ) the estimated parameters to be close to the mean kinetics of its representative cluster. Unlike previous approaches, it avoids resolution degradation as no spatial smoothing of heterogeneous functional regions is performed. The proposed approach showed enhanced qualitative and quantitative performance for simulations and patient data.

Chapter 4

Dual-biomarker Parametric Imaging from Dynamic ^{11}C-PiB PET

The biodistribution and chemical kinetics of the administered radiopharmaceutical in the organ of interest is usually quantified by computing parametric images of physiological parameters like relative blood flow (R_1), metabolism, distribution volume ration (DVR), receptor content etc. Such *biomarkers* provide fruitful information about neuronal activities in ROIs and to monitor and diagnose neurodegenration. Parametric images are generated via a "compact" tracer kinetic model that encapsulates all the biological and physiological factors that contribute to the measured tissue concentration of radiotracer [99].

^{11}C-PiB compound is a PET radiotracer used to image amyloid deposition in patients suffering from neurodegenrative dementia e.g. Alzheimer disease [257, 258]. Regional cerebral glucose metabolism (quantified using ^{18}F-FDG PET) and regional cerebral blood flow (CBF, quantified using ^{15}O-water PET) are used as biomarkers of neurodegenration [259]. CBF reflects neuronal activity, shown (in mouse models) to regulate regional vulnerability to β-amyloid deposition (^{11}C-PiB) [260]. Figure 4.1 shows correlations maps between DVR and CBF and DVR and R_1 for the whole group of 55 subjects and Figure 4.2 shows correlations maps between DVR and CBF and DVR and R_1 for the two subgroups (18 subjects each) with mean cortical DVRs of 1.49 and 0.93 respectively.

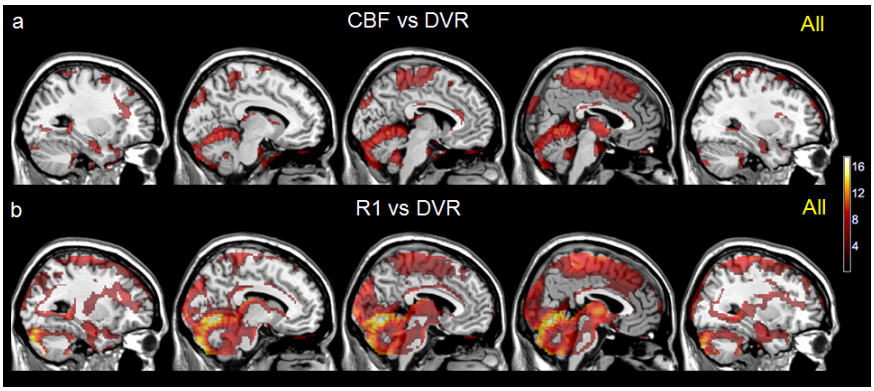

Figure 4.1: Positive Relationship between DVR maps and Cerebral Blood Flow (a) and DVR maps and R_1 maps (b) in entire group of non-demented older adults ($n = 55$). Reproduced from [260]

Recently, for the ^{11}C PiB compound, parametric images of R_1 and DVR has been proposed as an approach for dual-biomarker imaging to diagnose early onset of dementia from a single PET acquisition [259, 261]. This approach has also been considered to evaluate *biological* correlations between relative blood flow and β-amyloid depo-

sitions [260, 262]. However, the poor SNR of the acquired PET images, the kinetic model employed, and the limitations of the parameter estimation techniques results in noise-induced correlations that can be easily confounded with biological correlations. We demonstrate that noise-induced correlations pose significant confounds to interpretation [110].

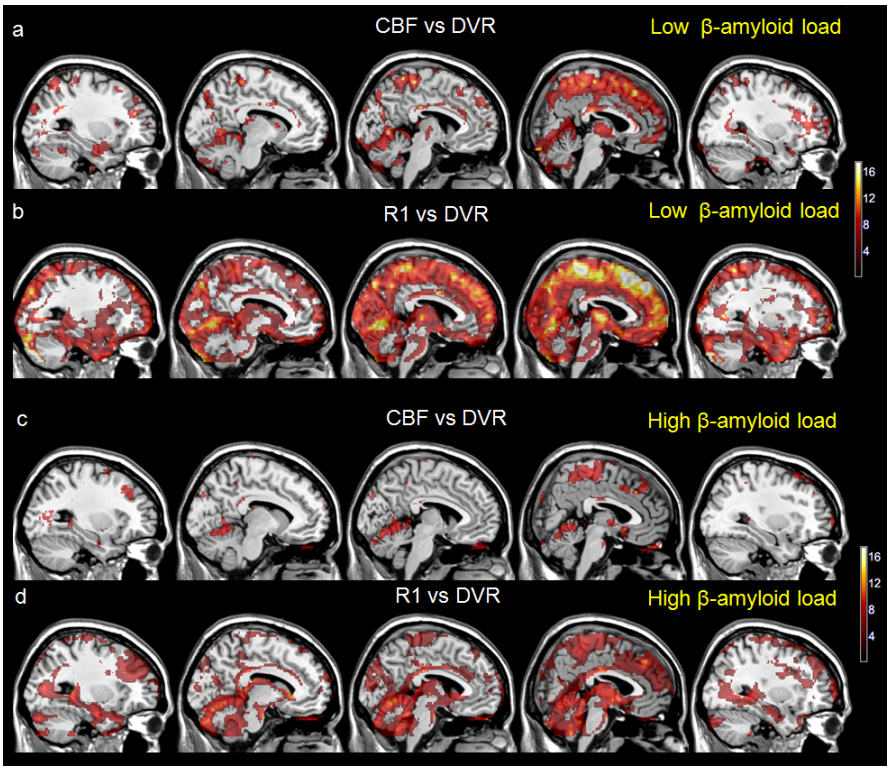

Figure 4.2: Positive Relationship between DVR maps and CBF (a, c) and DVR maps and R_1 maps (b, d) shown by tertiles of cortical β-amyloid load ($n = 18$ per group with mean cortical DVRs of 1.49 and 0.93 respectively). Reproduced from [260]

4.1 Theory

4.1.1 Pharmacokinetic Model for the ^{11}C-PiB Compound

We employ two-tissue compartment model with reference tissue input function as shown in Figure 4.4 to model the kinetics of ^{11}C-PiB compound. Tracer dynamics can be described by a system of first-order ordinary differential equations (ODEs) for tissue of interest and reference tissue:

$$\begin{aligned} \frac{\mathrm{d}C_{F+NS}(t)}{\mathrm{d}t} &= K_1 C_P(t) + k_4 C_{SP}(t) - (k_2 + k_3) C_{F+NS}(t) \\ \frac{\mathrm{d}C_{SP}(t)}{\mathrm{d}t} &= k_3 C_{F+NS}(t) - k_4 C_{SP}(t) \\ \frac{\mathrm{d}C_R(t)}{\mathrm{d}t} &= K_1^{'} C_P(t) - k_2^{'} C_R(t) \end{aligned} \tag{4.1}$$

A simplified reference tissue model (SRTM) can be obtained under the assumption of rapid equilibrium attained between C_{F+NS} and C_{SP}. At equilibrium, the total activity concentration in specific binding regions is approximated with a one-tissue compartment model with $C_T(t) = C_{F+NS}(t) + C_{SP}(t)$. Solving the differential equations (4.1) for SRTM and substituting $R_1 = \frac{K_1}{K_1^{'}}$ and $BP = \frac{k_3}{k_4} = DVR - 1$ yields the following analytical expression:

$$C_T(t) = R_1 C_R(t) + \left(k_2 - \frac{R_1 k_2}{1 + BP} \right) C_R(t) \otimes e^{-\frac{k_2}{1+BP} t} \tag{4.2}$$

Equation (4.2) can be solved using the basis function method [196] for weighted least squares.

4.1.2 Linearized Regression Method (Zhou et. al. 2003)

The differential equations for SRTM can be written as follows:

$$\begin{aligned} \frac{\mathrm{d}C_T(t)}{\mathrm{d}t} &= K_1 C_P(t) + k_{2a} C_T(t) \\ \frac{\mathrm{d}C_R(t)}{\mathrm{d}t} &= K_1^{'} C_P(t) - k_2^{'} C_R(t) \qquad (4.3) \\ k_{2a} &= \frac{k_2}{1+BP} \qquad (4.4) \\ \frac{K_1^{'}}{k_2^{'}} &= \frac{K_1}{k_2} \qquad (4.5) \end{aligned}$$

$C_P(t)$ can be eliminated from the set of differential equations (4.3) and, using equations (4.4)-(4.5), one can write a single ODE interms of $C_R(t)$:

$$\frac{\mathrm{d}C_T(t)}{\mathrm{d}t} = R_1 \frac{\mathrm{d}C_R(t)}{\mathrm{d}t} + k_2 C_R(t) - \frac{k_2}{1+BP} C_T(t) \qquad (4.6)$$

Integrating both sides of equation (4.6) and applying the initial conditions $C_T(0) = C_R(0) = 0$ gives:

$$C_T(t) = R_1 C_R(t) + k_2 \int_0^t C_R(s)\, ds - k_2^{'} \int_0^t C_T(s)\, ds \qquad (4.7)$$

Multiplying both sides of equation (4.7) by $\frac{1+BP}{k_2}$ and rearranging gives:

$$\int_0^t C_T(s)\,ds = DVR \int_0^t C_R(s)\,ds + \frac{DVR}{k_2/R_1} C_R(t) - \frac{DVR}{k_2} C_T(t) \tag{4.8}$$

Equations (4.7)-(4.8) can be solved using linearized regression method [263] to obtain estimates of R_1 and DVR.

In our analysis, we used two approaches: (1) basis function method to solve equation (4.2) and (2) linearized regression method to solve equations (4.7)-(4.8) to obtain voxel-wise estimates of R_1 and DVR.

4.1.3 Noise-induced correlations: A Mathematical Formulation

A mathematical formulation is presented which helps to understand the noise-induced effects from a theoretical point of view. It allows us to distill two conditions or constraints which, if enforced, will help preserve the true correlations in estimated parameters. Table 4.1 describes the notation used in the analysis.

Table 4.1: Mathematical notation for noise-induced correlations analysis.

Description	Notation
Data vector	$\boldsymbol{y} \in \mathcal{M}_{n\times 1}(\mathbb{R})$
Noise vector	$\boldsymbol{w} \in \mathcal{M}_{n\times 1}(\mathbb{R})$
Parameter vector	$\boldsymbol{\beta} \in \mathcal{M}_{p\times 1}(\mathbb{R})$
System model	$\boldsymbol{X} \in \mathcal{M}_{n\times p}(\mathbb{R})$
Linear operator	$\boldsymbol{L} \in \mathcal{M}_{p\times n}(\mathbb{R})$
True Covariance Matrix	$\boldsymbol{K} \in \mathcal{M}_{p\times p}(\mathbb{R})$
Noise Covariance Matrix	$\boldsymbol{K_w} \in \mathcal{M}_{n\times n}(\mathbb{R})$

We assume that $\boldsymbol{y}$ follows a linear model contaminated by additive Gaussian noise:

$$\boldsymbol{y} = \boldsymbol{X}\boldsymbol{\beta} + \boldsymbol{w} \tag{4.9}$$

where $\boldsymbol{w} \sim \mathcal{N}(\boldsymbol{0}, \boldsymbol{K_w})$. The estimated parameter vector, $\hat{\boldsymbol{\beta}}$, linearly depends on data:

$$\begin{aligned} \hat{\boldsymbol{\beta}} &= \boldsymbol{L}\boldsymbol{y} && (4.10)\\ &= \boldsymbol{L}(\boldsymbol{X}\boldsymbol{\beta} + \boldsymbol{w}) && (4.11)\\ &= \boldsymbol{L}\boldsymbol{X}\boldsymbol{\beta} + \boldsymbol{L}\boldsymbol{w} && (4.12) \end{aligned}$$

The estimated covariance matrix, $\hat{\boldsymbol{K}}$, is computed as follows:

$$\begin{aligned} \hat{\boldsymbol{K}} &= Cov(\hat{\boldsymbol{\beta}}) && (4.13)\\ &= E(\hat{\boldsymbol{\beta}}\hat{\boldsymbol{\beta}}^T) - E(\hat{\boldsymbol{\beta}})E(\hat{\boldsymbol{\beta}})^T && (4.14)\\ &= E(\boldsymbol{L}\boldsymbol{X}\boldsymbol{\beta} + \boldsymbol{L}\boldsymbol{w})(\boldsymbol{L}\boldsymbol{X}\boldsymbol{\beta} + \boldsymbol{L}\boldsymbol{w}^T) - E(\boldsymbol{L}\boldsymbol{X}\boldsymbol{\beta} + \boldsymbol{L}\boldsymbol{w})E(\boldsymbol{L}\boldsymbol{X}\boldsymbol{\beta} + \boldsymbol{L}\boldsymbol{w})^T && (4.15)\\ &= (\boldsymbol{L}\boldsymbol{X})Cov(\boldsymbol{\beta})(\boldsymbol{L}\boldsymbol{X})^T + \boldsymbol{L}\boldsymbol{K_w}\boldsymbol{L}^T && (4.16)\\ &= (\boldsymbol{L}\boldsymbol{X})\boldsymbol{K}(\boldsymbol{L}\boldsymbol{X})^T + \boldsymbol{L}\boldsymbol{K_w}\boldsymbol{L}^T && (4.17) \end{aligned}$$

Equation (4.17) shows that the estimated covariance matrix, $\hat{\boldsymbol{K}}$, is additively contaminated by the shaped noise-covariance matrix, $\boldsymbol{L}\boldsymbol{K_w}\boldsymbol{L}^T$. The first term on the RHS of equation (4.17) also shows that even in the absence of noise the true covari-

ance matrix is shaped by the operator $\boldsymbol{LX}$. This equation provides two constraints that need to be enforced in order to recover the true covariance matrix, $\boldsymbol{K}$. These constraints are listed below:

$$\boldsymbol{LX} = \boldsymbol{I} \tag{4.18}$$

$$\boldsymbol{LK_wL}^T = \gamma \boldsymbol{R} \tag{4.19}$$

where $\boldsymbol{I}$ is an identity matrix, $\boldsymbol{R}$ is a prespecified positive definite diagonal matrix, and γ is a positive real number.

4.2 Methodology

For validation, kinetic parameters (K_1, k_2, k_3, k_4) from ^{11}C-PiB studies of normal controls were estimated, averaged and assigned to a mathematical brain phantom, from which time-activity-curves (TACs) were generated using a two-tissue compartmental model (blood-volume fraction was set to 3%). This was followed by realistic simulations of dynamic frames for the geometry of the HRRT scanner (including 20 noise realizations in the sinogram-space of the same subject; i.e. simulating no biological correlations). OSEM reconstructions ($1 - 10$ iterations) for each dataset were generated. Parametric Images of R_1 and DVR ($= BP + 1$) were obtained via the simplified reference tissue model (SRTM) using (1) the basis function method (BFM) and (2) linearized formulation and regression (LR) to estimate the parameters. Noise-

Bias trade-off curves were obtained for R_1 and DVR images, demonstrating reduced bias with increasing iterations at the cost of enhanced noise levels, as expected.

Next, Pearson correlation coefficients were determined for each voxel-pair of (R_1, DVR) vectors (across the 20 noise realizations) with lower and upper bounds for a 95% confidence interval, and quantitatively evaluated for each OSEM reconstruction. A hypothesis test for no correlation with a probability value (p-value) of 0.05 was also conducted, and the resulting correlation images were analyzed qualitatively and quantitatively for all OSEM iterations. Specifically, 13 regions-of-interest (ROIs) were considered. Overall, R_1 and DVR showed statistically significant correlations, across the OSEM iterations, for all ROIs using the BFM approach, while this was also the case for the LR method with the exception of the parietal cortex, pons and occipital pole. Figure 4.3 shows a schematic of the adopted methodology for simulations and analysis.

4.3 Results and Conclusions

Figure 4.5 shows parameteric images of R_1 and DVR for increasing OSEM iterations. Figure 4.6 shows R_1-DVR correlation plots against OSEM iterations. R_1 and DVR showed statistically significant noise induced correlations, for all ROIs using the basis function method (BFM). Weighted linear regression method showed reduced noise-induced correlations in some regions (compared to BFM) except Cerebellum, Parietal Cortex, Frontal Cortex, Pons and Thalamus; but still depicted significant correlations

for a number of regions. The observed *significant correlations* are attributed purely to noise in parametric quantification of dynamic ^{11}C-PiB PET. This shows that in R_1-DVR analysis, biological correlations may be confounded with noise-induced correlations. Future work should explore potential approaches that quantify and account for there associations to provide more accurate estimates of correlations between DVR and R_1 estimates from a single acquisition.

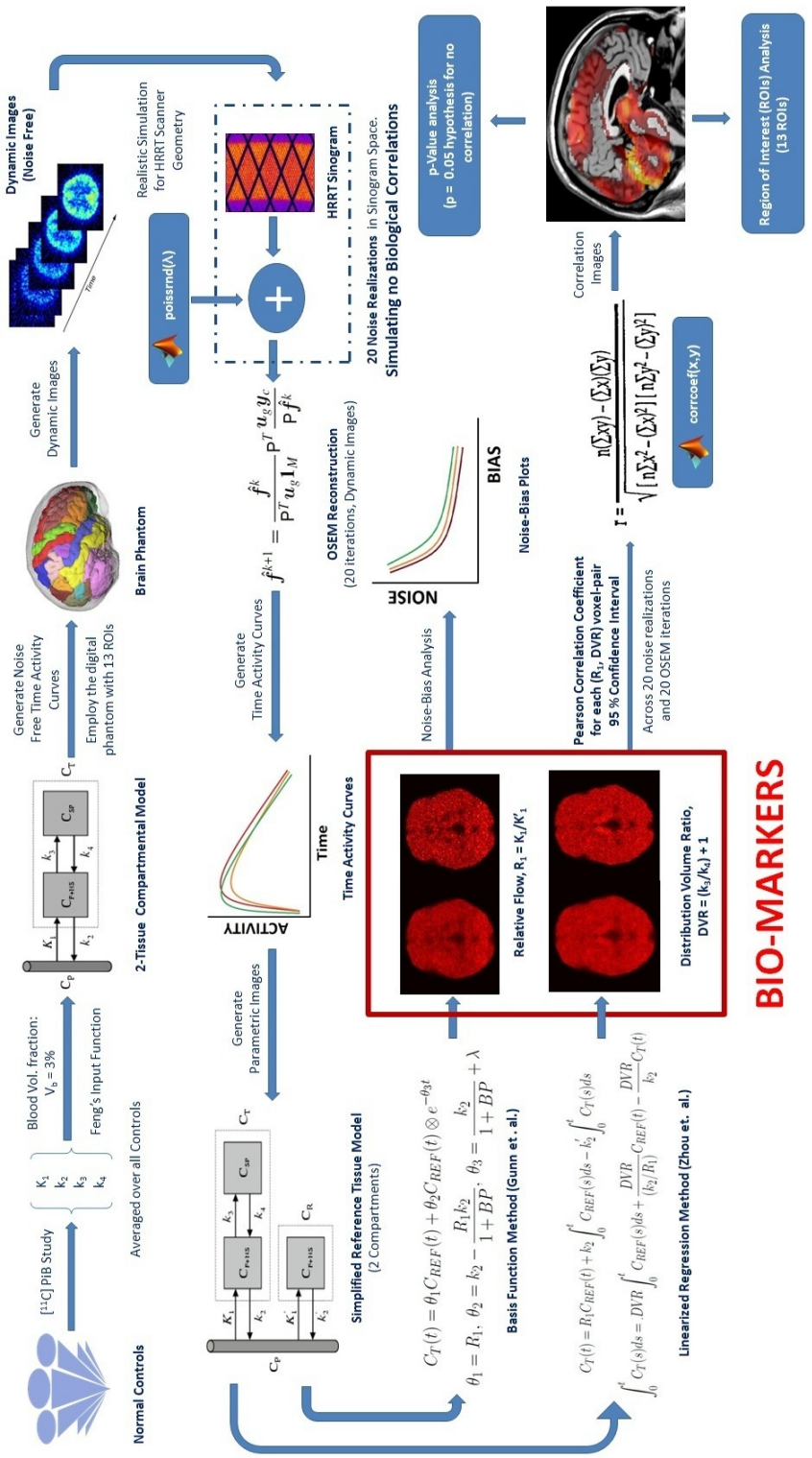

Figure 4.3: Methodology for simulations and analysis

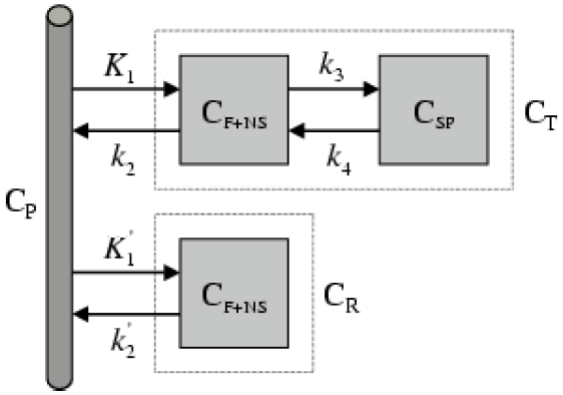

Figure 4.4: Two-tissue compartmental model with reference tissue input function for ^{11}C-PiB compound [104, Figure 1]. $C_P(t)$ is the activity concentration time-course in plasma, $C_{F+NS}(t)$ is the activity concentration time-course for free and non-specific binding, $C_{SP}(t)$ is the activity concentration time-course for specific binding, $C_T(t) = C_{F+NS}(t) + C_{SP}(t)$ is the total activity concentration time-course in the tissue of interest, and $C_R(t)$ is the activity concentration time-course in the reference tissue. K_1, k_2, k_3, and k_4 are the transport rate constants for the tissue of interest and $K_1^{'}$ and $k_2^{'}$ are the influx and efflux rate constants for the reference tissue.

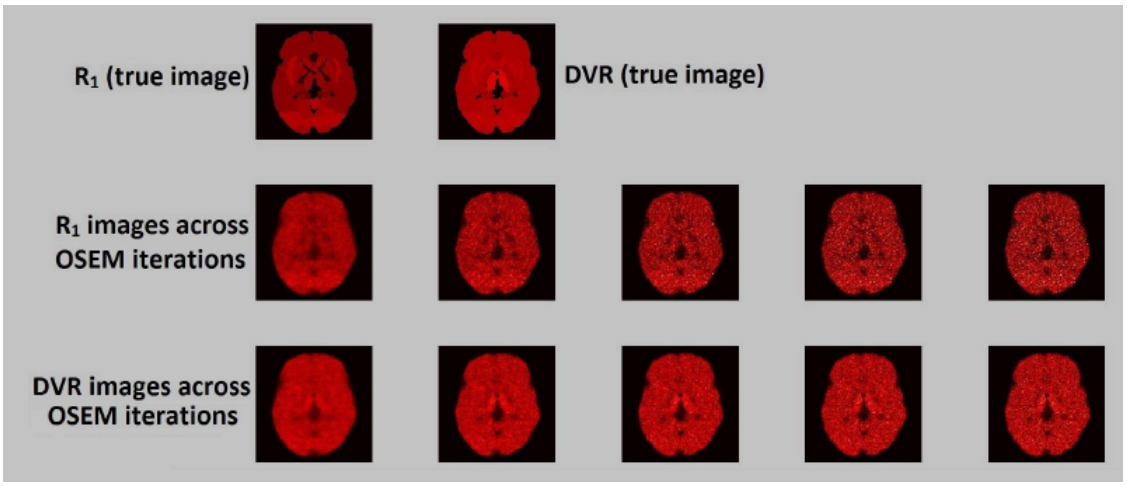

Figure 4.5: Simulated parametric images of R_1 and DVR against OSEM iterations.

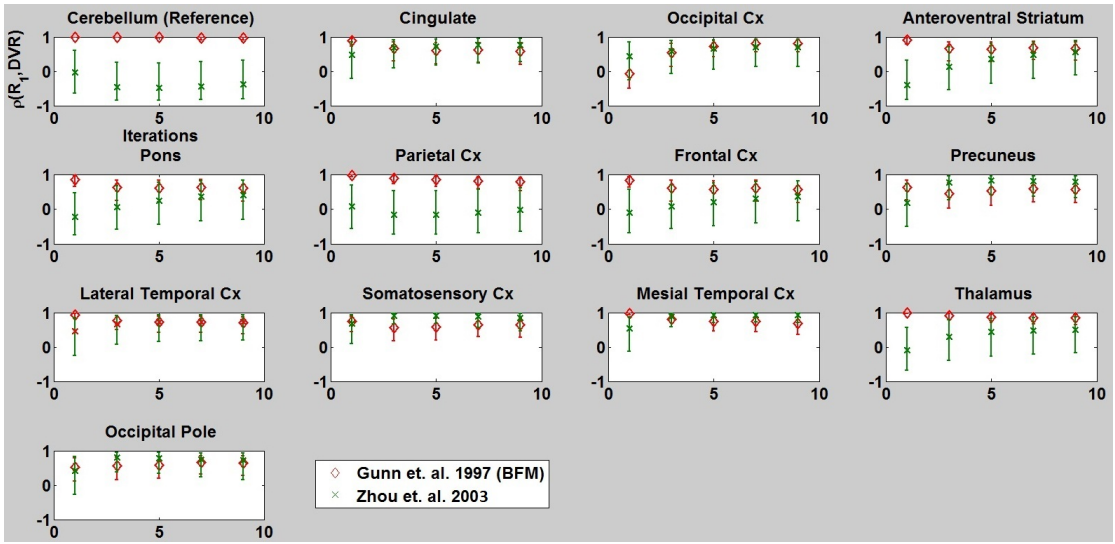

Figure 4.6: R_1-DVR correlation plots against OSEM iterations (95% confidence interval).

Chapter 5

Conclusions and Future Work

Motion-compensation in Dynamic Brain PET Imaging: We have demonstrated through extensive simulations that GIIMC algorithm enables compensation of both inter-frame and intra-frame motion in a unified framework. It significantly reduces transmission-emission mimatches by coregistering emission data with time-weighted average of motion-transformed transmission data for each dynamic frame. Such transmission-emission mismatch artifacts are significant even for low motion levels when convention methods of transmission-emission alignment are employed. GIIMC algorithm is also amenable to different framing sequences.

Future work involves: (1) validation on cohort studies involving dynamic PET imaging and assessment in the context of quantitative parametric imaging. An interesting cohort would be subjects with Tourette syndrome which constitutes significant patient motion during the dynamic PET scan. A scatter plot of the distribution vol-

ume ratios (DVRs) with and without motion correction would be a promising statistic that may reveal the ability of GIIMC algorithm to efficiently segregate normal subjects from Tourette subjects, (2) incorporating motion correction in Direct 4-D parametric image reconstruction to obtain parametric images with superior resolution-noise performance [264]. This approach is feasible as the motion blurring kernel for each dynamic frame, obtained from optical motion tracking, can be applied in the parametric image space with two convolution operations (in forward and back projection operations), and (3) further minimizing susceptibility to transmission-emission mismatch artifacts using TOF PET image reconstruction techniques. TOF PET reconstruction, compared to non-TOF reconstruction methods, has demonstrated robustness to inconsistencies between emission data and corrections [265].

Parametric Myocardial Perfusion PET Imaging: Parametric imaging based on physiological clustering clearly outperforms conventional parameter estimation techniques by producing images with higher SNR. It substantially reduces noise with minimal increase in bias by utilizing kinetic information from physiologically similar voxels. Unlike previous approaches, it avoids resolution degradation as no spatial smoothing of heterogeneous functional regions is performed. The proposed approach showed enhanced qualitative and quantitative performance for simulations (transmural and non-transmural perfusion defect) and patient data.

Future work involves: (1) application of physiological clustering approach to other tracers (e.g. ^{13}N-ammonia and ^{18}F-FDG) used in myocardial perfusion imaging, us-

ing convex K-means clustering to obviate sensitivity to initialization, incorporating spatial proximity in the similarity metric to reduce miss-classification of voxels, studying the impact of resolution modeling on the proposed physiological clustering based parameter estimation method, and the influence of IDIF from FA or ICA on the accuracy of estimated parameters, (2) incorporating spatio-temporal priors within Direct 4-D reconstruction to obtain substantial noise reduction at the cost of minimal increase in bias, and (3) comparing the proposed approach with various existing noise reduction techniques like non-local means filtering, principle component analysis, and wavelet smoothing techniques.

Bibliography

[1] S. Savarese, "Shape reconstruction from shadows and reflections," Ph.D. dissertation, California Institute of Technology, 2005.

[2] S. Savarese, M. Andreetto, H. Rushmeier, F. Bernardini, and P. Perona, "3d reconstruction by shadow carving: Theory and practical evaluation," *International journal of computer vision*, vol. 71, no. 3, pp. 305–336, 2007.

[3] S. R. Arridge, "Optical tomography in medical imaging," *Inverse problems*, vol. 15, no. 2, p. R41, 1999.

[4] A. Fenster and D. B. Downey, "3-d ultrasound imaging: A review," *Engineering in Medicine and Biology Magazine, IEEE*, vol. 15, no. 6, pp. 41–51, 1996.

[5] M. N. Wernick and J. N. Aarsvold, *Emission tomography: the fundamentals of PET and SPECT*. Academic Press, 2004.

[6] L. A. Shepp and B. F. Logan, "The fourier reconstruction of a head section," *Nuclear Science, IEEE Transactions on*, vol. 21, no. 3, pp. 21–43, 1974.

BIBLIOGRAPHY

[7] A. C. Kak and M. Slaney, *Principles of computerized tomographic imaging*. Society for Industrial and Applied Mathematics, 2001.

[8] S. R. Cherry, J. A. Sorenson, and M. E. Phelps, *Physics in nuclear medicine*. Elsevier Health Sciences, 2012.

[9] J. Radon, "On the determination of functions from their integral values along certain manifolds," *Medical Imaging, IEEE Transactions on*, vol. 5, no. 4, pp. 170–176, 1986.

[10] J. Hadamard, "Sur les problèmes aux dérivées partielles et leur signification physique," *Princeton university bulletin*, vol. 13, no. 49-52, p. 28, 1902.

[11] ——, *Lectures on Cauchy's problem in linear partial differential equations*. Courier Dover Publications, 2003.

[12] G. T. Herman, "Image reconstruction from projections," *Real-Time Imaging*, vol. 1, no. 1, pp. 3–18, 1995.

[13] C. L. Epstein, *Introduction to the mathematics of medical imaging*. Siam, 2008.

[14] F. Natterer and F. Natterer, *The mathematics of computerized tomography*. Springer, 1986.

[15] Y. Chen, Q. Wu, and X. He, "Human action recognition by radon transform," in *Data Mining Workshops, 2008. ICDMW'08. IEEE International Conference on*. IEEE, 2008, pp. 862–868.

[16] S. Tabbone, L. Wendling, and J.-P. Salmon, "A new shape descriptor defined on the radon transform," *Computer Vision and Image Understanding*, vol. 102, no. 1, pp. 42–51, 2006.

[17] S. Helgason, *Integral geometry and Radon transforms*. Springer, 2011.

[18] V. P. Palamodov, *Reconstructive integral geometry*. Springer, 2004, vol. 98.

[19] T. Peter, "The radon transform-theory and implementation," Ph.D. dissertation, PhD thesis, Dept. of Mathematical Modelling Section for Digital Signal Processing of Technical University of Denmark, 1996.

[20] D. I. Marcussen and C. H. Trinderup, "Radon transform in tomographic image reconstruction," Ph.D. dissertation, Technical University of Denmark, DTU, DK-2800 Kgs. Lyngby, Denmark, 2009.

[21] J. Hsieh, "Computed tomography: principles, design, artifacts, and recent advances." SPIE Bellingham, WA, 2009.

[22] A. Rahmim and H. Zaidi, "Pet versus spect: strengths, limitations and challenges," *Nuclear medicine communications*, vol. 29, no. 3, pp. 193–207, 2008.

[23] J. L. Prince and J. M. Links, *Medical imaging signals and systems*. Pearson Prentice Hall Upper Saddle River, NJ, 2006.

[24] A. Rahmim, "Statistical list-mode image reconstruction and motion compensa-

tion techniques in high-resolution positron emission tomography (pet)," Ph.D. dissertation, University of British Columbia, 2005.

[25] A. Braun, T. Balkin, N. Wesenten, R. Carson, M. Varga, P. Baldwin, S. Selbie, G. Belenky, and P. Herscovitch, "Regional cerebral blood flow throughout the sleep-wake cycle. an h2 (15) o pet study." *Brain*, vol. 120, no. 7, pp. 1173–1197, 1997.

[26] M. Jahanshahi, I. H. Jenkins, R. G. Brown, C. D. Marsden, R. E. Passingham, and D. J. Brooks, "Self-initiated versus externally triggered movements i. an investigation using measurement of regional cerebral blood flow with pet and movement-related potentials in normal and parkinson's disease subjects," *Brain*, vol. 118, no. 4, pp. 913–933, 1995.

[27] P. Videbech, "Pet measurements of brain glucose metabolism and blood flow in major depressive disorder: a critical review," *Acta Psychiatrica Scandinavica*, vol. 101, no. 1, pp. 11–20, 2000.

[28] T. Dierks, V. Jelic, R. D. Pascual-Marqui, L.-O. Wahlund, P. Julin, D. E. Linden, K. Maurer, B. Winblad, and A. Nordberg, "Spatial pattern of cerebral glucose metabolism (pet) correlates with localization of intracerebral eeg-generators in alzheimer's disease," *Clinical Neurophysiology*, vol. 111, no. 10, pp. 1817–1824, 2000.

[29] N. Avril, M. Menzel, J. Dose, M. Schelling, W. Weber, F. Jänicke, W. Nathrath,

and M. Schwaiger, "Glucose metabolism of breast cancer assessed by 18f-fdg pet: histologic and immunohistochemical tissue analysis," *Journal of Nuclear Medicine*, vol. 42, no. 1, pp. 9–16, 2001.

[30] F. G. Duhaylongsod, V. J. Lowe, E. F. Patz Jr, A. L. Vaughn, R. E. Coleman, and W. G. Wolfe, "Lung tumor growth correlates with glucose metabolism measured by fluoride-18 fluorodeoxyglucose positron emission tomography," *The Annals of thoracic surgery*, vol. 60, no. 5, pp. 1348–1352, 1995.

[31] W. C. Drevets, E. Frank, J. C. Price, D. J. Kupfer, D. Holt, P. J. Greer, Y. Huang, C. Gautier, and C. Mathis, "Pet imaging of serotonin 1a receptor binding in depression," *Biological psychiatry*, vol. 46, no. 10, pp. 1375–1387, 1999.

[32] D. F. Wong, H. S. Singer, J. Brandt, E. Shaya, C. Chen, J. Brown, A. Kimball, A. Gjedde, R. F. Dannals, H. T. Ravert *et al.*, "D2-like dopamine receptor density in tourette syndrome measured by pet." *Journal of nuclear medicine: official publication, Society of Nuclear Medicine*, vol. 38, no. 8, pp. 1243–1247, 1997.

[33] H. N. Wagner, H. D. Burns, R. F. Dannals, D. F. Wong, B. Langstrom, T. Duelfer, J. J. Frost, H. T. Ravert, J. M. Links, S. B. Rosenbloom *et al.*, "Imaging dopamine receptors in the human brain by positron tomography," *Science*, vol. 221, no. 4617, pp. 1264–1266, 1983.

[34] D. F. Wong, H. N. Wagner, L. E. Tune, R. F. Dannals, G. D. Pearlson, J. M. Links, C. A. Tamminga, E. P. Broussolle, H. T. Ravert, A. A. Wilson *et al.*, "Positron emission tomography reveals elevated d2 dopamine receptors in drug-naive schizophrenics," *Science*, vol. 234, no. 4783, pp. 1558–1563, 1986.

[35] P. Vaissier, M. Goorden, A. Taylor, and F. Beekman, "Fast count–regulated osem reconstruction with adaptive resolution recovery," *Medical Imaging, IEEE Transactions on*, vol. 32(12), pp. 2250–2261, 2013.

[36] Y. Jian, "Spatial resolution improvement in positron emission tomography: Physics, statistical models and iterative image reconstruction," Ph.D. dissertation, Yale University, 2014.

[37] K. Lange and R. Carson, "Em reconstruction algorithms for emission and transmission tomography." *Journal of computer assisted tomography*, vol. 8, no. 2, pp. 306–316, 1984.

[38] L. A. Shepp and Y. Vardi, "Maximum likelihood reconstruction for emission tomography," *Medical Imaging, IEEE Transactions on*, vol. 1, no. 2, pp. 113–122, 1982.

[39] H. M. Hudson and R. S. Larkin, "Accelerated image reconstruction using ordered subsets of projection data," *Medical Imaging, IEEE Transactions on*, vol. 13, no. 4, pp. 601–609, 1994.

[40] T. Hsiao, A. Rangarajan, and G. R. Gindi, "Provably convergent osem-like reconstruction algorithm for emission tomography," in *Medical Imaging 2002*. International Society for Optics and Photonics, 2002, pp. 10–19.

[41] I.-T. Hsiao, A. Rangarajan, and G. Gindi, "A new convergent map reconstruction algorithm for emission tomography using ordered subsets and separable surrogates," in *Biomedical Imaging, 2002. Proceedings. 2002 IEEE International Symposium on*. IEEE, 2002, pp. 409–412.

[42] T. Hsiao, A. Rangarajan, P. Khurd, and G. Gindi, "An accelerated convergent ordered subsets algorithm for emission tomography," *Physics in medicine and biology*, vol. 49, no. 11, p. 2145, 2004.

[43] I.-T. Hsiao, P. Khurd, A. Rangarajan, and G. Gindi, "An overview of fast convergent ordered-subsets reconstruction methods for emission tomography based on the incremental em algorithm," *Nuclear Instruments and Methods in Physics Research Section A: Accelerators, Spectrometers, Detectors and Associated Equipment*, vol. 569, no. 2, pp. 429–433, 2006.

[44] P. Khurd, I.-T. Hsiao, A. Rangarajan, and G. Gindi, "A globally convergent regularized ordered-subset em algorithm for list-mode reconstruction," *Nuclear Science, IEEE Transactions on*, vol. 51, no. 3, pp. 719–725, 2004.

[45] L. Kaufman, "Maximum likelihood, least squares, and penalized least squares

for pet," *Medical Imaging, IEEE Transactions on*, vol. 12, no. 2, pp. 200–214, 1993.

[46] J. Nuyts and J. A. Fessler, "A penalized-likelihood image reconstruction method for emission tomography, compared to postsmoothed maximum-likelihood with matched spatial resolution," *Medical Imaging, IEEE Transactions on*, vol. 22, no. 9, pp. 1042–1052, 2003.

[47] J. A. Fessler, "Penalized weighted least-squares image reconstruction for positron emission tomography," *Medical Imaging, IEEE Transactions on*, vol. 13, no. 2, pp. 290–300, 1994.

[48] ——, "Mean and variance of implicitly defined biased estimators (such as penalized maximum likelihood): Applications to tomography," *Image Processing, IEEE Transactions on*, vol. 5, no. 3, pp. 493–506, 1996.

[49] G. Wang and J. Qi, "Analysis of penalized likelihood image reconstruction for dynamic pet quantification," *Medical Imaging, IEEE Transactions on*, vol. 28, no. 4, pp. 608–620, 2009.

[50] E. U. Mumcuoglu, R. Leahy, S. R. Cherry, and Z. Zhou, "Fast gradient-based methods for bayesian reconstruction of transmission and emission pet images," *Medical Imaging, IEEE Transactions on*, vol. 13, no. 4, pp. 687–701, 1994.

[51] J. Nuyts, P. Dupont, S. Stroobants, R. Benninck, L. Mortelmans, and

P. Suetens, "Simultaneous maximum a posteriori reconstruction of attenuation and activity distributions from emission sinograms," *Medical Imaging, IEEE Transactions on*, vol. 18, no. 5, pp. 393–403, 1999.

[52] J. Qi and R. M. Leahy, "Resolution and noise properties of map reconstruction for fully 3-d pet," *Medical Imaging, IEEE Transactions on*, vol. 19, no. 5, pp. 493–506, 2000.

[53] A. R. De Pierro and M. B. Yamagishi, "Fast em-like methods for maximum" a posteriori" estimates in emission tomography," *Medical Imaging, IEEE Transactions on*, vol. 20, no. 4, pp. 280–288, 2001.

[54] J. Nuyts, D. Bequé, P. Dupont, and L. Mortelmans, "A concave prior penalizing relative differences for maximum-a-posteriori reconstruction in emission tomography," *Nuclear Science, IEEE Transactions on*, vol. 49, no. 1, pp. 56–60, 2002.

[55] P. J. Green, "Bayesian reconstructions from emission tomography data using a modified em algorithm," *Medical Imaging, IEEE Transactions on*, vol. 9, no. 1, pp. 84–93, 1990.

[56] J. A. Zahnen, "Penalized maximum likelihood reconstruction methods for emission tomography," Ph.D. dissertation, University of Florida, 2006.

[57] E. U. Mumcuoglu, R. M. Leahy, S. R. Cherry, and E. Hoffman, "Accurate geometric and physical response modelling for statistical image reconstruction in

high resolution pet," in *Nuclear Science Symposium, 1996. Conference Record., 1996 IEEE*, vol. 3. IEEE, 1996, pp. 1569–1573.

[58] D. L. Bailey, D. W. Townsend, P. E. Valk, and M. N. Maisey, *Positron emission tomography*. Springer, 2005.

[59] M. Blume, "Joint image and motion reconstruction for positron emission tomography," Ph.D. dissertation, Fakultt fr Informatik Technische Universitt Mnchen, 2011.

[60] J. Logan and H. Bernstein, "A monte carlo simulation of compton scattering in positron emission tomography," *Journal of computer assisted tomography*, vol. 7, no. 2, pp. 316–320, 1983.

[61] B. Bendriem and D. W. Townsend, *The theory and practice of 3D PET*. Springer, 1998, vol. 32.

[62] C. Thompson, "The effect of collimation on scatter fraction in multi-slice pet," *Nuclear Science, IEEE Transactions on*, vol. 35, no. 1, pp. 598–602, 1988.

[63] T. Spinks, T. Jones, D. Bailey, D. Townsend, S. Grootoonk, P. Bloomfield, M.-C. Gilardi, M. Casey, B. Sipe, and J. Reed, "Physical performance of a positron tomograph for brain imaging with retractable septa," *Physics in medicine and biology*, vol. 37, no. 8, p. 1637, 1992.

[64] D. L. Bailey and S. R. Meikle, "A convolution-subtraction scatter correction

method for 3d pet," *Physics in medicine and biology*, vol. 39, no. 3, p. 411, 1994.

[65] A. J. Reader, S. Zhao, P. J. Julyan, D. L. Hastings, and J. Zweit, "Adaptive correction of scatter and random events for 3-d backprojected pet data," *Nuclear Science, IEEE Transactions on*, vol. 48, no. 4, pp. 1350–1356, 2001.

[66] S. Grootoonk, T. Spinks, D. Sashin, N. Spyrou, and T. Jones, "Correction for scatter in 3d brain pet using a dual energy window method," *Physics in medicine and biology*, vol. 41, no. 12, p. 2757, 1996.

[67] S. R. Cherry, S. R. Meikle, and E. J. Hoffman, "Correction and characterization of scattered events in three-dimensional pet using scanners with retractable septa." *Journal of Nuclear Medicine: official publication, Society of Nuclear Medicine*, vol. 34, no. 4, pp. 671–678, 1993.

[68] J. M. Ollinger, "Model-based scatter correction for fully 3d pet," *Physics in medicine and biology*, vol. 41, no. 1, p. 153, 1996.

[69] C. Watson, "New, faster, image-based scatter correction for 3d pet," *Nuclear Science, IEEE Transactions on*, vol. 47, no. 4, pp. 1587–1594, 2000.

[70] J. M. Ollinger and J. A. Fessler, "Positron-emission tomography," *IEEE Signal Processing Magazine*, vol. 14(1), pp. 43–55, 1997.

[71] R. Manavaki, A. J. Reader, C. Keller, J. Missimer, and R. J. Walledge, "Scatter

modeling for 3-d pet list-mode em reconstruction," in *Nuclear Science Symposium Conference Record, 2002 IEEE*, vol. 3. IEEE, 2002, pp. 1863–1868.

[72] D. Brasse, P. E. Kinahan, C. Lartizien, C. Comtat, M. Casey, and C. Michel, "Correction methods for random coincidences in fully 3d whole-body pet: impact on data and image quality," *Journal of nuclear medicine*, vol. 46, no. 5, pp. 859–867, 2005.

[73] O. Rokitta, M. Casey, K. Wienhard, and U. Pictrzyk, "Random correction for positron emission tomography using singles count rates," in *Nuclear Science Symposium Conference Record, 2000 IEEE*, vol. 3. IEEE, 2000, pp. 17–37.

[74] B. Pointon and V. Sossi, "Towards model-based randoms correction for 3-d dual head coincidence imaging," in *Nuclear Science Symposium Conference Record, 2003 IEEE*, vol. 4. IEEE, 2003, pp. 2799–2803.

[75] C. S. Levin and E. J. Hoffman, "Calculation of positron range and its effect on the fundamental limit of positron emission tomography system spatial resolution," *Physics in medicine and biology*, vol. 44, no. 3, p. 781, 1999.

[76] A. Rahmim, J. Tang, M. Lodge, S. Lashkari, M. R. Ay, R. Lautamäki, B. Tsui, and F. Bengel, "Analytic system matrix resolution modeling in pet: an application to rb-82 cardiac imaging," *Physics in medicine and biology*, vol. 53, no. 21, p. 5947, 2008.

[77] J. Cal-González, J. Herraiz, S. España, P. Corzo, J. J. Vaquero, M. Desco, and J. M. Udias, "Positron range estimations with penelopet," *Physics in medicine and biology*, vol. 58, no. 15, p. 5127, 2013.

[78] M. R. Palmer, X. Zhu, and J. A. Parker, "Modeling and simulation of positron range effects for high resolution pet imaging," *Nuclear Science, IEEE Transactions on*, vol. 52, no. 5, pp. 1391–1395, 2005.

[79] B. Bai, A. Ruangma, R. Laforest, Y.-C. Tai, and R. M. Leahy, "Positron range modeling for statistical pet image reconstruction," in *Nuclear Science Symposium Conference Record, 2003 IEEE*, vol. 4. IEEE, 2003, pp. 2501–2505.

[80] S. E. Derenzo, "Mathematical removal of positron range blurring in high resolution tomography," *Nuclear Science, IEEE Transactions on*, vol. 33, no. 1, pp. 565–569, 1986.

[81] S. Haber, S. E. Derenzo, and D. Uber, "Application of mathematical removal of positron range blurring in positron emission tomography," *Nuclear Science, IEEE Transactions on*, vol. 37, no. 3, pp. 1293–1299, 1990.

[82] A. Del Guerra, *Ionizing radiation detectors for medical imaging*. World Scientific, 2004.

[83] A. Rahmim, J. Qi, and V. Sossi, "Resolution modeling in pet imaging: Theory, practice, benefits, and pitfalls," *Medical physics*, vol. 40, no. 6, p. 064301, 2013.

[84] S. Blinder, M.-L. Camborde, K. R. Buckley, A. Rahmim, K. J.-C. Cheng, T. J. Ruth, and V. Sossi, "Influence of depth of interaction on spatial resolution and image quality for the hrrt," in *Nuclear Science Symposium Conference Record, 2005 IEEE*, vol. 3. IEEE, 2005, pp. 5–pp.

[85] M. E. Casey, "Point spread function reconstruction in pet," *Siemens Medical Solution, Knoxville, USA*, 2007.

[86] M. Ito, S. J. Hong, and J. S. Lee, "Positron emission tomography (pet) detectors with depth-of-interaction (doi) capability," *Biomedical Engineering Letters*, vol. 1, no. 2, pp. 70–81, 2011.

[87] J. G. Rogers, "A method for correcting the depth-of-interaction blurring in pet cameras," *Medical Imaging, IEEE Transactions on*, vol. 14, no. 1, pp. 146–150, 1995.

[88] L. R. MacDonald and M. Dahlbom, "Parallax correction in pet using depth of interaction information," *Nuclear Science, IEEE Transactions on*, vol. 45, no. 4, pp. 2232–2237, 1998.

[89] M. V. Green, H. G. Ostrow, J. Seidel, and M. G. Pomper, "Experimental evaluation of depth-of-interaction correction in a small-animal positron emission tomography scanner," *Molecular imaging*, vol. 9, no. 6, p. 311, 2010.

[90] Y. Shao, S. R. Cherry, S. Siegel, and R. W. Silverman, "A study of inter-crystal

scatter in small scintillator arrays designed for high resolution pet imaging," *Nuclear Science, IEEE Transactions on*, vol. 43, no. 3, pp. 1938–1944, 1996.

[91] I. Bankman, *Handbook of medical image processing and analysis*. academic press, 2008.

[92] E. J. Hoffman, T. M. Guerrero, G. Germano, W. Digby, and M. Dahlbom, "Pet system calibrations and corrections for quantitative and spatially accurate images," *Nuclear Science, IEEE Transactions on*, vol. 36, no. 1, pp. 1108–1112, 1989.

[93] A. Rahmim, J.-C. Cheng, K. Dinelle, M. Shilov, W. P. Segars, O. G. Rousset, B. M. Tsui, D. F. Wong, and V. Sossi, "System matrix modelling of externally tracked motion," *Nuclear medicine communications*, vol. 29, no. 6, p. 574, 2008.

[94] H. Zaidi, "Recent developments and future trends in nuclear medicine instrumentation," *Z Med Phys*, vol. 16, no. 1, pp. 5–17, 2006.

[95] A. Rahmim, O. Rousset, and H. Zaidi, "Strategies for motion tracking and correction in pet," *PET Clinics*, vol. 2, no. 2, pp. 251–266, 2007.

[96] H. Mohy-ud Din, N. Karakatsanis, M. Ay, C. Endres, D. Wong, and A. Rahmim, "Generalized inter-frame and intra-frame motion correction in pet imaging-a simulation study," in *Nuclear Science Symposium and Medical Imaging Conference (NSS/MIC), 2011 IEEE*. IEEE, 2011, pp. 3858–3862.

[97] H. Mohy-ud Din, N. Karakatsanis, J. Goddard, J. Baba, W. Wills, A. Tahari, D. Wong, and A. Rahmim, "Generalized dynamic pet inter-frame and intra-frame motion correction-phantom and human validation studies," in *Nuclear Science Symposium and Medical Imaging Conference (NSS/MIC), 2012 IEEE*. IEEE, 2012, pp. 3067–3078.

[98] N. A. Karakatsanis, H. Zaidi, and C. Tsoumpas, "Generalized 3d and 4d motion compensated whole-body pet image reconstruction employing nested em deconvolution," in *Imaging Systems and Techniques (IST), 2014 IEEE International Conference on*. IEEE, 2014, pp. 263–268.

[99] R. E. Carson, "Tracer kinetic modeling in pet," in *Positron Emission Tomography*. Springer, 2005, pp. 127–159.

[100] E. D. Morris, C. J. Endres, K. C. Schmidt, B. T. Christian, R. F. Muzic Jr, and R. E. Fisher, "Kinetic modeling in positron emission tomography," *Emission Tomography: The Fundamentals of PET and SPECT. Academic, San Diego*, 2004.

[101] M. Bentourkia and H. Zaidi, "Tracer kinetic modeling in pet," *PET Clinics*, vol. 2, no. 2, pp. 267–277, 2007.

[102] H. Watabe, Y. Ikoma, Y. Kimura, M. Naganawa, and M. Shidahara, "Pet kinetic analysiscompartmental model," *Annals of nuclear medicine*, vol. 20, no. 9, pp. 583–588, 2006.

[103] R. N. Gunn, S. R. Gunn, and V. J. Cunningham, "Positron emission tomography compartmental models," *Journal of Cerebral Blood Flow & Metabolism*, vol. 21, no. 6, pp. 635–652, 2001.

[104] R. N. Gunn, S. R. Gunn, F. E. Turkheimer, J. A. Aston, and V. J. Cunningham, "Positron emission tomography compartmental models: A basis pursuit strategy for kinetic modeling," *Journal of Cerebral Blood Flow & Metabolism*, vol. 22, no. 12, pp. 1425–1439, 2002.

[105] K. Schmidt and F. Turkheimer, "Kinetic modeling in positron emission tomography." *The quarterly journal of nuclear medicine: official publication of the Italian Association of Nuclear Medicine (AIMN)[and] the International Association of Radiopharmacology (IAR)*, vol. 46, no. 1, pp. 70–85, 2002.

[106] E. R. Carson, C. Cobelli, and L. Finkelstein, "The mathematical modeling of metabolic and endocrine systems: model formulation, identification, and validation," *AMC*, vol. 10, p. 12, 1983.

[107] S. Huang and M. Phelps, "Principles of tracer kinetic modeling in positron emission tomography and autoradiography," *Positron emission tomography and autoradiography: principles and applications for the brain and heart*, pp. 287–346, 1986.

[108] K. Levenberg, "A method for the solution of certain problems in least squares," *Quarterly of applied mathematics*, vol. 2, pp. 164–168, 1944.

[109] D. W. Marquardt, "An algorithm for least-squares estimation of nonlinear parameters," *Journal of the Society for Industrial & Applied Mathematics*, vol. 11, no. 2, pp. 431–441, 1963.

[110] H. Mohy-ud Din, N. A. Karakatsanis, J. C. Price, Y. Zhou, S. M. Resnick, C. J. Endres, W. E. Klunk, C. A. Mathis, D. F. Wong, and A. Rahmim, "Investigation of noise-induced correlations in dual-biomarker parametric imaging from dynamic [c-11] pib pet," in *Journal of Cerebral Blood Flow and Metabolism*, vol. 32. Nature Publishing Group, NY 10013-1917 USA, 2012, pp. S186–S187.

[111] C. Messa, Y. Choi, C. K. Hoh, E. L. Jacobs, J. A. Glaspy, S. Rege, E. Nitzsche, S.-C. Huang, M. E. Phelps, and R. A. Hawkins, "Quantification of glucose utilization in liver metastases: parametric imaging of fdg uptake with pet," *Journal of computer assisted tomography*, vol. 16, no. 5, pp. 684–689, 1992.

[112] P. Millet, V. Ibáñez, J. Delforge, S. Pappata, and J. Guimón, "Wavelet analysis of dynamic pet data: application to the parametric imaging of benzodiazepine receptor concentration," *Neuroimage*, vol. 11, no. 5, pp. 458–472, 2000.

[113] L. G. Strauss and P. S. Conti, "The applications of pet in clinical oncology." *Journal of nuclear medicine: official publication, Society of Nuclear Medicine*, vol. 32, no. 4, pp. 623–48, 1991.

[114] W. Chen, "Clinical applications of pet in brain tumors," *Journal of nuclear medicine*, vol. 48, no. 9, pp. 1468–1481, 2007.

[115] P. A. Kaufmann and P. G. Camici, "Myocardial blood flow measurement by pet: technical aspects and clinical applications," *Journal of Nuclear Medicine*, vol. 46, no. 1, pp. 75–88, 2005.

[116] M. Bergström, A. Grahnen, and B. Långström, "Positron emission tomography microdosing: a new concept with application in tracer and early clinical drug development," *European journal of clinical pharmacology*, vol. 59, no. 5-6, pp. 357–366, 2003.

[117] A. Al-Nahhas, Z. Win, T. Szyszko, A. Singh, C. Nanni, S. Fanti, and D. Rubello, "Gallium-68 pet: a new frontier in receptor cancer imaging," *Anticancer research*, vol. 27, no. 6B, pp. 4087–4094, 2007.

[118] T. Faber, N. Raghunath, D. Tudorascu, and J. Votaw, "Motion correction of pet brain images through deconvolution: I. theoretical development and analysis in software simulations," *Physics in Medicine and Biology*, vol. 54, no. 3, p. 797, 2009.

[119] W. H. Richardson, "Bayesian-based iterative method of image restoration," *JOSA*, vol. 62, no. 1, pp. 55–59, 1972.

[120] L. B. Lucy, "An iterative technique for the rectification of observed distributions," *The astronomical journal*, vol. 79, p. 745, 1974.

[121] L. Tellmann, R. Fulton, U. Pietrzyk, I. Nickel, I. Stangier, O. Winz, and H. Her-

zog, "Concepts of registration and correction of head motion in positron emission tomography." *Zeitschrift fur medizinische Physik*, vol. 16, no. 1, pp. 67–74, 2005.

[122] O. A. van den Heuvel, R. Boellaard, D. J. Veltman, C. Mesina, and A. A. Lammertsma, "Attenuation correction of pet activation studies in the presenceof task-related motion," *Neuroimage*, vol. 19, no. 4, pp. 1501–1509, 2003.

[123] H. Herzog, L. Tellmann, R. Fulton, I. Stangier, E. R. Kops, K. Bente, C. Boy, R. Hurlemann, and U. Pietrzyk, "Motion artifact reduction on parametric pet images of neuroreceptor binding," *Journal of Nuclear Medicine*, vol. 46, no. 6, pp. 1059–1065, 2005.

[124] N. Costes, A. Dagher, K. Larcher, A. C. Evans, D. L. Collins, and A. Reilhac, "Motion correction of multi-frame pet data in neuroreceptor mapping: simulation based validation," *Neuroimage*, vol. 47, no. 4, pp. 1496–1505, 2009.

[125] U. E. Ruttimann, P. J. Andreason, and D. Rio, "Head motion during positron emission tomography: Is it significant?" *Psychiatry Research: Neuroimaging*, vol. 61, no. 1, pp. 43–51, 1995.

[126] M. V. Green, J. Seidel, S. D. Stein, T. E. Tedder, K. M. Kempner, C. Kertzman, and T. A. Zeffiro, "Head movement in normal subjects during simulated pet brain imaging with and without head restraint," *Journal of Nuclear Medicine*, vol. 35, no. 9, pp. 1538–1546, 1994.

[127] P. M. Bloomfield, T. J. Spinks, J. Reed, L. Schnorr, A. M. Westrip, L. Livieratos, R. Fulton, and T. Jones, "The design and implementation of a motion correction scheme for neurological pet," *Physics in medicine and biology*, vol. 48, no. 8, p. 959, 2003.

[128] D. F. Wong, J. R. Brašić, H. S. Singer, D. J. Schretlen, H. Kuwabara, Y. Zhou, A. Nandi, M. A. Maris, M. Alexander, W. Ye *et al.*, "Mechanisms of dopaminergic and serotonergic neurotransmission in tourette syndrome: clues from an in vivo neurochemistry study with pet," *Neuropsychopharmacology*, vol. 33, no. 6, pp. 1239–1251, 2007.

[129] B. Lopresti, A. Russo, W. Jones, T. Fisher, D. Crouch, D. Altenburger, and D. Townsend, "Implementation and performance of an optical motion tracking system for high resolution brain pet imaging," *Nuclear Science, IEEE Transactions on*, vol. 46, no. 6, pp. 2059–2067, 1999.

[130] Y. Picard and C. J. Thompson, "Motion correction of pet images using multiple acquisition frames," *Medical Imaging, IEEE Transactions on*, vol. 16, no. 2, pp. 137–144, 1997.

[131] A. J. Montgomery, K. Thielemans, M. A. Mehta, F. Turkheimer, S. Mustafovic, and P. M. Grasby, "Correction of head movement on pet studies: comparison of methods," *Journal of Nuclear Medicine*, vol. 47, no. 12, pp. 1936–1944, 2006.

[132] S. H. Keller, M. Sibomana, O. V. Olesen, C. Svarer, S. Holm, F. L. Andersen,

and L. Højgaard, "Methods for motion correction evaluation using 18f-fdg human brain scans on a high-resolution pet scanner," *Journal of Nuclear Medicine*, vol. 53, no. 3, pp. 495–504, 2012.

[133] H. Zaidi, M.-L. Montandon, and S. Meikle, "Strategies for attenuation compensation in neurological pet studies," *Neuroimage*, vol. 34, no. 2, pp. 518–541, 2007.

[134] M. Daube-Witherspoon, Y. Yan, M. Green, R. Carson, K. Kempner, and P. Herscovitch, "Correction for motion distortion in pet by dynamic monitoring of patient position," *J. Nucl. Med*, vol. 31, no. 5, p. 816, 1990.

[135] M. Menke, M. Atkins, and K. Buckley, "Compensation methods for head motion detected during pet imaging," *Nuclear Science, IEEE Transactions on*, vol. 43, no. 1, pp. 310–317, 1996.

[136] S.-K. Woo, H. Watabe, Y. Choi, K. M. Kim, C. C. Park, P. M. Bloomfield, and H. Iida, "Sinogram-based motion correction of pet images using optical motion tracking system and list-mode data acquisition," *Nuclear Science, IEEE Transactions on*, vol. 51, no. 3, pp. 782–788, 2004.

[137] J. Qi and R. H. Huesman, "List mode reconstruction for pet with motion compensation: a simulation study," in *Biomedical Imaging, 2002. Proceedings. 2002 IEEE International Symposium on.* IEEE, 2002, pp. 413–416.

[138] R. E. Carson, W. C. Barker, J.-S. Liow, and C. A. Johnson, "Design of a motion-compensation osem list-mode algorithm for resolution-recovery reconstruction for the hrrt," in *Nuclear Science Symposium Conference Record, 2003 IEEE*, vol. 5. IEEE, 2003, pp. 3281–3285.

[139] A. Rahmim, P. Bloomfield, S. Houle, M. Lenox, C. Michel, K. R. Buckley, T. J. Ruth, and V. Sossi, "Motion compensation in histogram-mode and list-mode em reconstructions: beyond the event-driven approach," *Nuclear Science, IEEE Transactions on*, vol. 51, no. 5, pp. 2588–2596, 2004.

[140] K. Thielemans, S. Mustafovic, and L. Schnorr, "Image reconstruction of motion corrected sinograms," in *Nuclear Science Symposium Conference Record, 2003 IEEE*, vol. 4. IEEE, 2003, pp. 2401–2406.

[141] P. Buhler, U. Just, E. Will, J. Kotzerke, and J. van den Hoff, "An accurate method for correction of head movement in pet," *Medical Imaging, IEEE Transactions on*, vol. 23, no. 9, pp. 1176–1185, 2004.

[142] A. Rahmim, K. Dinelle, J.-C. K. Cheng, M. A. Shilov, W. P. Segars, S. C. Lidstone, S. Blinder, O. G. Rousset, H. Vajihollahi, B. M. Tsui *et al.*, "Accurate event-driven motion compensation in high-resolution pet incorporating scattered and random events," *Medical Imaging, IEEE Transactions on*, vol. 27, no. 8, pp. 1018–1033, 2008.

[143] R. R. Fulton, S. R. Meikle, S. Eberl, J. Pfeiffer, and C. J. Constable, "Correction

for head movements in positron emission tomography using an optical motion-tracking system," *Nuclear Science, IEEE Transactions on*, vol. 49, no. 1, pp. 116–123, 2002.

[144] N. Raghunath, T. Faber, S. Suryanarayanan, and J. Votaw, "Motion correction of pet brain images through deconvolution: Ii. practical implementation and algorithm optimization," *Physics in Medicine and Biology*, vol. 54, no. 3, p. 813, 2009.

[145] S. M. LaValle, *Planning algorithms*. Cambridge university press, 2006.

[146] M. Moakher, "Means and averaging in the group of rotations," *SIAM journal on matrix analysis and applications*, vol. 24, no. 1, pp. 1–16, 2002.

[147] C. Gramkow, "On averaging rotations," *Journal of Mathematical Imaging and Vision*, vol. 15, no. 1-2, pp. 7–16, 2001.

[148] R. Tron, R. Vidal, and A. Terzis, "Distributed pose averaging in camera networks via consensus on se (3)," in *Distributed Smart Cameras, 2008. ICDSC 2008. Second ACM/IEEE International Conference on*. IEEE, 2008, pp. 1–10.

[149] J. H. Manton, "A globally convergent numerical algorithm for computing the centre of mass on compact lie groups," in *Control, Automation, Robotics and Vision Conference, 2004. ICARCV 2004 8th*, vol. 3. IEEE, 2004, pp. 2211–2216.

[150] V. Sossi, H. W. de Jong, W. C. Barker, P. Bloomfield, Z. Burbar, M.-L. Camborde, C. Comtat, L. A. Eriksson, S. Houle, D. Keator *et al.*, "The second generation hrrt-a multi-centre scanner performance investigation," in *Nuclear Science Symposium Conference Record, 2005 IEEE*, vol. 4. IEEE, 2005, pp. 2195–2199.

[151] K. Dinelle, S. Blinder, J.-C. K. Cheng, S. Lidstone, K. Buckley, T. Ruth, and V. Sossi, "Investigation of subject motion encountered during a typical positron emission tomography scan," in *Nuclear Science Symposium Conference Record, 2006. IEEE*, vol. 6. IEEE, 2006, pp. 3283–3287.

[152] B. K. Horn, "Closed-form solution of absolute orientation using unit quaternions," *JOSA A*, vol. 4, no. 4, pp. 629–642, 1987.

[153] M. G. Ullisch, J. J. Scheins, C. Weirich, E. R. Kops, A. Celik, L. Tellmann, T. Stöcker, H. Herzog, and N. J. Shah, "Mr-based pet motion correction procedure for simultaneous mr-pet neuroimaging of human brain," *PloS one*, vol. 7, no. 11, p. e48149, 2012.

[154] H. Hoppe, T. DeRose, T. Duchamp, M. Halstead, H. Jin, J. McDonald, J. Schweitzer, and W. Stuetzle, "Piecewise smooth surface reconstruction," in *Proceedings of the 21st annual conference on Computer graphics and interactive techniques*. ACM, 1994, pp. 295–302.

[155] K. Dinelle, H. Ngo, S. Blinder, N. Vafai, G. Topping, and V. Sossi, "Frame-to-

frame image realignment assessment tool for dynamic brain positron emission tomography," *Medical physics*, vol. 38, no. 2, pp. 773–781, 2011.

[156] O. V. Olesen, R. R. Paulsen, L. Hojgaard, B. Roed, and R. Larsen, "Motion tracking for medical imaging: a nonvisible structured light tracking approach," *Medical Imaging, IEEE Transactions on*, vol. 31, no. 1, pp. 79–87, 2012.

[157] O. V. Olesen, J. M. Sullivan, T. Mulnix, R. R. Paulsen, L. Hojgaard, B. Roed, R. E. Carson, E. D. Morris, and R. Larsen, "List-mode pet motion correction using markerless head tracking: Proof-of-concept with scans of human subject," *Medical Imaging, IEEE Transactions on*, vol. 32, no. 2, pp. 200–209, 2013.

[158] C. J. Murray and A. D. Lopez, "Global mortality, disability, and the contribution of risk factors: Global burden of disease study," *The Lancet*, vol. 349, no. 9063, pp. 1436–1442, 1997.

[159] M. Gulati, D. K. Pandey, M. F. Arnsdorf, D. S. Lauderdale, R. A. Thisted, R. H. Wicklund, A. J. Al-Hani, and H. R. Black, "Exercise capacity and the risk of death in women the st james women take heart project," *Circulation*, vol. 108, no. 13, pp. 1554–1559, 2003.

[160] T. Thom, N. Haase, W. Rosamond, V. J. Howard, J. Rumsfeld, T. Manolio, Z.-J. Zheng, K. Flegal, C. Odonnell, S. Kittner *et al.*, "Heart disease and stroke statistics2006 update a report from the american heart association statistics

committee and stroke statistics subcommittee," *Circulation*, vol. 113, no. 6, pp. e85–e151, 2006.

[161] G. A. Mensah and D. W. Brown, "An overview of cardiovascular disease burden in the united states," *Health Affairs*, vol. 26, no. 1, pp. 38–48, 2007.

[162] T. H. Schindler, H. R. Schelbert, A. Quercioli, and V. Dilsizian, "Cardiac pet imaging for the detection and monitoring of coronary artery disease and microvascular health," *JACC: Cardiovascular Imaging*, vol. 3, no. 6, pp. 623–640, 2010.

[163] V. Dilsizian and J. Narula, *Atlas of nuclear cardiology*. Springer, 2013.

[164] M. A. Lodge and F. M. Bengel, "Methodology for quantifying absolute myocardial perfusion with pet and spect," *Current cardiology reports*, vol. 9, no. 2, pp. 121–128, 2007.

[165] X.-B. Pan, J. Decklerck, and D. D. Burckhardt, "Cardiac positron emission tomography: Overview of myocardial perfusion, myocardial blood flow and coronary flow reserve imaging," *www.siemens.com/mi*, pp. 1–12, 2009.

[166] N. G. Uren, J. A. Melin, B. De Bruyne, W. Wijns, T. Baudhuin, and P. G. Camici, "Relation between myocardial blood flow and the severity of coronary-artery stenosis," *New England Journal of Medicine*, vol. 330, no. 25, pp. 1782–1788, 1994.

[167] R. Parkash, R. DeKemp, T. Ruddy, A. Kitsikis, R. Hart, L. Beauschene, K. Williams, R. Davies, M. Labinaz, and R. Beanlands, "Potential utility of rubidium 82 pet quantification in patients with 3-vessel coronary artery disease," *Journal of nuclear cardiology*, vol. 11, no. 4, pp. 440–449, 2004.

[168] K. Yoshida, N. Mullani, and K. L. Gould, "Coronary flow and flow reserve by pet simplified for clinical applications using rubidium-82 or nitrogen-13-ammonia," *Journal of Nuclear Medicine*, vol. 37, no. 10, pp. 1701–1712, 1996.

[169] F. M. Bengel, T. Higuchi, M. S. Javadi, and R. Lautamäki, "Cardiac positron emission tomography," *Journal of the American College of Cardiology*, vol. 54, no. 1, pp. 1–15, 2009.

[170] R. Nakazato, D. S. Berman, E. Alexanderson, and P. Slomka, "Myocardial perfusion imaging with pet," *Imaging in medicine*, vol. 5, no. 1, pp. 35–46, 2013.

[171] M. A. Lodge, H. Braess, F. Mahmoud, J. Suh, N. Englar, S. Geyser-Stoops, J. Jenkins, S. L. Bacharach, and V. Dilsizian, "Developments in nuclear cardiology: Transition from single photon emission computed tomography to positron emission tomography/computed tomography," *Journal of Invasive Cardiology*, vol. 17, no. 9, p. 491, 2005.

[172] M. Salerno and G. A. Beller, "Noninvasive assessment of myocardial perfusion," *Circulation: Cardiovascular Imaging*, vol. 2, no. 5, pp. 412–424, 2009.

[173] R. Sciagrà, "Quantitative cardiac positron emission tomography: The time is coming!" *Scientifica*, vol. 2012, 2012.

[174] J. O'Donnell, P. Wojtylak, and P. Faulhaber, "Myocardial perfusion imaging: past, present and future," *MedicaMundi*, vol. 54(1), pp. 46–49, 2010.

[175] H. Ohira, T. Dowsley, G. Dwivedi, R. A. deKemp, B. J. Chow, T. D. Ruddy, R. A. Davies, J. DaSilva, R. S. Beanlands, and R. Hessian, "Quantification of myocardial blood flow using pet to improve the management of patients with stable ischemic coronary artery disease," *Future cardiology*, vol. 10, no. 5, pp. 611–631, 2014.

[176] G. R. Small, R. G. Wells, T. Schindler, B. J. Chow, and T. D. Ruddy, "Advances in cardiac spect and pet imaging: Overcoming the challenges to reduce radiation exposure and improve accuracy," *Canadian Journal of Cardiology*, vol. 29, no. 3, pp. 275–284, 2013.

[177] S. Dorbala and M. F. Di Carli, "Cardiac pet perfusion: Prognosis, risk stratification, and clinical management," in *Seminars in nuclear medicine*, vol. 44, no. 5. Elsevier, 2014, pp. 344–357.

[178] K. Yoshinaga, R. Klein, and N. Tamaki, "Generator-produced rubidium-82 positron emission tomography myocardial perfusion imagingfrom basic aspects to clinical applications," *Journal of cardiology*, vol. 55, no. 2, pp. 163–173, 2010.

[179] P. Arumugam, D. Tout, and C. Tonge, "Myocardial perfusion scintigraphy using rubidium-82 positron emission tomography," *British medical bulletin*, p. ldt026, 2013.

[180] R. A. deKemp, T. D. Ruddy, T. Hewitt, M. M. Dalipaj, and R. Beanlands, "Detection of serial changes in absolute myocardial perfusion with 82rb pet." *Journal of nuclear medicine: official publication, Society of Nuclear Medicine*, vol. 41, no. 8, pp. 1426–1435, 2000.

[181] R. Klein, R. S. Beanlands *et al.*, "Quantification of myocardial blood flow and flow reserve: technical aspects," *Journal of nuclear cardiology*, vol. 17, no. 4, pp. 555–570, 2010.

[182] A. J. Reader and J. Verhaeghe, "4d image reconstruction for emission tomography," *Physics in medicine and biology*, vol. 59, no. 22, p. R371, 2014.

[183] K. L. Gould, Y. Nakagawa, K. Nakagawa, S. Sdringola, M. J. Hess, M. Haynie, N. Parker, N. Mullani, and R. Kirkeeide, "Frequency and clinical implications of fluid dynamically significant diffuse coronary artery disease manifest as graded, longitudinal, base-to-apex myocardial perfusion abnormalities by noninvasive positron emission tomography," *Circulation*, vol. 101, no. 16, pp. 1931–1939, 2000.

[184] K. L. Gould, N. P. Johnson, T. M. Bateman, R. S. Beanlands, F. M. Bengel, R. Bober, P. G. Camici, M. D. Cerqueira, B. J. Chow, M. F. Di Carli *et al.*,

"Anatomic versus physiologic assessment of coronary artery disease: role of coronary flow reserve, fractional flow reserve, and positron emission tomography imaging in revascularization decision-making," *Journal of the American College of Cardiology*, vol. 62, no. 18, pp. 1639–1653, 2013.

[185] I. Valenta, A. Quercioli, and T. H. Schindler, "Diagnostic value of pet-measured longitudinal flow gradient for the identification of coronary artery disease," *JACC: Cardiovascular Imaging*, vol. 7, no. 4, pp. 387–396, 2014.

[186] A. Rahmim, H. Mohy-ud Din, and T. Schindler, "Base-to-apex gradient abnormality detection task performance in myocardial perfusion pet imaging," in *Society of Nuclear Medicine Annual Meeting Abstracts*, vol. 55, no. Supplement 1. Soc Nuclear Med, 2014, p. 600.

[187] A. Rahmim, A. K. Tahari, and T. H. Schindler, "Towards quantitative myocardial perfusion pet in the clinic," *Journal of the American College of Radiology*, vol. 11, no. 4, pp. 429–432, 2014.

[188] H. Mohy-ud Din, N. A. Karakatsanis, M. A. Lodge, J. Tang, and A. Rahmim, "Parametric myocardial perfusion pet imaging using physiological clustering," in *SPIE Medical Imaging*. International Society for Optics and Photonics, 2014, pp. 90 380P–90 380P.

[189] M. Lortie, R. S. Beanlands, K. Yoshinaga, R. Klein, J. N. DaSilva *et al.*, "Quantification of myocardial blood flow with 82rb dynamic pet imaging," *European*

journal of nuclear medicine and molecular imaging, vol. 34, no. 11, pp. 1765–1774, 2007.

[190] G. El Fakhri, A. Sitek, B. Guérin, M. F. Kijewski, M. F. Di Carli, and S. C. Moore, "Quantitative dynamic cardiac 82rb pet using generalized factor and compartment analyses," *Journal of nuclear medicine*, vol. 46, no. 8, pp. 1264–1271, 2005.

[191] A. Karpikov, H. Tagare, T. Mulnix, J.-D. Gallezot, A. Sinusas, C. Liu, and R. Carson, "Myocardial blood flow from dynamic pet using independent component analysis," in *Nuclear Science Symposium and Medical Imaging Conference (NSS/MIC), 2012 IEEE*. IEEE, 2012, pp. 2222–2226.

[192] A. A. Lammertsma and S. P. Hume, "Simplified reference tissue model for pet receptor studies," *Neuroimage*, vol. 4, no. 3, pp. 153–158, 1996.

[193] M. Slifstein, B. Kolachana, E. Simpson, P. Tabares, B. Cheng, M. Duvall, W. G. Frankle, D. Weinberger, M. Laruelle, and A. Abi-Dargham, "Comt genotype predicts cortical-limbic d1 receptor availability measured with [11c] nnc112 and pet," *Molecular psychiatry*, vol. 13, no. 8, pp. 821–827, 2008.

[194] J. A. Nye, J. R. Votaw, N. Jarkas, D. Purselle, V. Camp, J. D. Bremner, C. D. Kilts, C. B. Nemeroff, and M. M. Goodman, "Compartmental modeling of 11c-homadam binding to the serotonin transporter in the healthy human brain," *Journal of Nuclear Medicine*, vol. 49, no. 12, pp. 2018–2025, 2008.

[195] V. Berti, C. Polito, S. Ramat, E. Vanzi, M. T. De Cristofaro, G. Pellicanò, F. Mungai, P. Marini, A. R. Formiconi, S. Sorbi *et al.*, "Brain metabolic correlates of dopaminergic degeneration in de novo idiopathic parkinsons disease," *European journal of nuclear medicine and molecular imaging*, vol. 37, no. 3, pp. 537–544, 2010.

[196] R. N. Gunn, A. A. Lammertsma, S. P. Hume, and V. J. Cunningham, "Parametric imaging of ligand-receptor binding in pet using a simplified reference region model," *Neuroimage*, vol. 6, no. 4, pp. 279–287, 1997.

[197] S.-C. Huang and Y. Zhou, "Spatially-coordinated regression for image-wise model fitting to dynamic pet data for generating parametric images," *Nuclear Science, IEEE Transactions on*, vol. 45, no. 3, pp. 1194–1199, 1998.

[198] F. O'Sullivan and A. Saha, "Use of ridge regression for improved estimation of kinetic constants from pet data," *Medical Imaging, IEEE Transactions on*, vol. 18, no. 2, pp. 115–125, 1999.

[199] M. E. Kamasak, C. A. Bouman, E. D. Morris, and K. Sauer, "Direct reconstruction of kinetic parameter images from dynamic pet data," *Medical Imaging, IEEE Transactions on*, vol. 24, no. 5, pp. 636–650, 2005.

[200] Y. Lin, J. Haldar, Q. Li, P. Conti, and R. Leahy, "Sparsity constrained mixture modeling for the estimation of kinetic parameters in dynamic pet," *Medical Imaging, IEEE Transactions on*, vol. 33(1), pp. 173 – 185, 2014.

[201] W. Zhu, J. Ouyang, Y. Rakvongthai, G. E. Fakhri, and Y. Fan, "A unified bayesian approach to kinetic model estimation in dynamic positron emission tomography," *arXiv preprint arXiv:1409.7454*, 2014.

[202] Y. Zhou, J. A. Aston, and A. M. Johansen, "Bayesian model comparison for compartmental models with applications in positron emission tomography," *Journal of Applied Statistics*, vol. 40, no. 5, pp. 993–1016, 2013.

[203] Y.-H. Dean Fang, G. El Fakhri, J. A. Becker, and N. M. Alpert, "Parametric imaging with bayesian priors: A validation study with¡ sup¿ 11¡/sup¿ c-altropane pet," *NeuroImage*, vol. 61, no. 1, pp. 131–138, 2012.

[204] J. Ashburner, J. Haslan, C. Taylor, V. Cunningham, and T. Jones, "Lvii-7. a cluster analysis approach for the characterisation of dynamic pet data," *Journal of Cerebral Blood Flow and Metabolism*, vol. 15, no. 1, p. S626, 1995.

[205] Y. Kimura, H. Hsu, H. Toyama, M. Senda, and N. M. Alpert, "Improved signal-to-noise ratio in parametric images by cluster analysis," *Neuroimage*, vol. 9, no. 5, pp. 554–561, 1999.

[206] J. L. Chen, S. R. Gunn, M. S. Nixon, and R. N. Gunn, "Markov random field models for segmentation of pet images," in *information processing in medical imaging*. Springer, 2001, pp. 468–474.

[207] K.-P. Wong, D. Feng, S. R. Meikle, and M. J. Fulham, "Segmentation of dy-

namic pet images using cluster analysis," *Nuclear Science, IEEE Transactions on*, vol. 49, no. 1, pp. 200–207, 2002.

[208] Y. Zhou, S.-C. Huang, M. Bergsneider, and D. F. Wong, "Improved parametric image generation using spatial-temporal analysis of dynamic pet studies," *NeuroImage*, vol. 15, no. 3, pp. 697–707, 2002.

[209] H. Guo, R. Renaut, K. Chen, and E. Reiman, "Clustering huge data sets for parametric pet imaging," *Biosystems*, vol. 71, no. 1, pp. 81–92, 2003.

[210] X. Huang, Y. Zhou, S. Bao, and S.-C. Huang, "Clustering-based linear least square fitting method for generation of parametric images in dynamic fdg pet studies," *International journal of biomedical imaging*, vol. 2007, 2007.

[211] A. Saad, B. Smith, G. Hamarneh, and T. Möller, "Simultaneous segmentation, kinetic parameter estimation, and uncertainty visualization of dynamic pet images," in *Medical Image Computing and Computer-Assisted Intervention–MICCAI 2007*. Springer, 2007, pp. 726–733.

[212] F. E. Turkheimer, M. Brett, D. Visvikis, and V. J. Cunningham, "Multiresolution analysis of emission tomography images in the wavelet domain," *Journal of Cerebral Blood Flow & Metabolism*, vol. 19, no. 11, pp. 1189–1208, 1999.

[213] F. E. Turkheimer, R. B. Banati, D. Visvikis, J. Aston, R. N. Gunn, and V. J. Cunningham, "Modeling dynamic pet-spect studies in the wavelet domain."

Journal of cerebral blood flow and metabolism: official journal of the International Society of Cerebral Blood Flow and Metabolism, vol. 20, no. 5, pp. 879–893, 2000.

[214] F. E. Turkheimer, M. Brett, J. A. Aston, A. P. Leff, P. A. Sargent, R. J. Wise, P. M. Grasby, and V. J. Cunningham, "Statistical modeling of positron emission tomography images in wavelet space," *Journal of Cerebral Blood Flow & Metabolism*, vol. 20, no. 11, pp. 1610–1618, 2000.

[215] F. E. Turkheimer, J. A. Aston, R. B. Banati, C. Riddell, and V. J. Cunningham, "A linear wavelet filter for parametric imaging with dynamic pet," *Medical Imaging, IEEE Transactions on*, vol. 22, no. 3, pp. 289–301, 2003.

[216] F. E. Turkheimer, J. Aston, M.-C. Asselin, and R. Hinz, "Multi-resolution bayesian regression in pet dynamic studies using wavelets," *Neuroimage*, vol. 32, no. 1, pp. 111–121, 2006.

[217] J.-W. Lin, A. F. Laine, O. Akinboboye, and S. R. Bergmann, "Use of wavelet transforms in analysis of time–activity data from cardiac pet," *Journal of Nuclear Medicine*, vol. 42, no. 2, pp. 194–200, 2001.

[218] J.-W. Lin, R. R. Sciacca, R.-L. Chou, A. F. Laine, and S. R. Bergmann, "Quantification of myocardial perfusion in human subjects using 82rb and wavelet-based noise reduction," *Journal of Nuclear Medicine*, vol. 42, no. 2, pp. 201–208, 2001.

[219] J.-W. Lin, A. F. Laine, and S. R. Bergmann, "Improving pet-based physiological quantification through methods of wavelet denoising," *Biomedical Engineering, IEEE Transactions on*, vol. 48, no. 2, pp. 202–212, 2001.

[220] N. M. Alpert, A. Reilhac, T. C. Chio, and I. Selesnick, "Optimization of dynamic measurement of receptor kinetics by wavelet denoising," *Neuroimage*, vol. 30, no. 2, pp. 444–451, 2006.

[221] J. O. Prior, G. Allenbach, I. Valenta, M. Kosinski, C. Burger, F. R. Verdun, A. B. Delaloye, and P. A. Kaufmann, "Quantification of myocardial blood flow with 82rb positron emission tomography: clinical validation with 15o-water," *European journal of nuclear medicine and molecular imaging*, vol. 39, no. 6, pp. 1037–1047, 2012.

[222] E. M. Renkin, "Transport of potassium-42 from blood to tissue in isolated mammalian skeletal muscles," *Am J Physiol*, vol. 197, no. 1205-1210, p. 297, 1959.

[223] C. Crone, "The permeability of capillaries in various organs as determined by use of the indicator diffusionmethod," *Acta physiologica scandinavica*, vol. 58, no. 4, pp. 292–305, 1963.

[224] P. Zanotti-Fregonara, K. Chen, J.-S. Liow, M. Fujita, and R. B. Innis, "Image-derived input function for brain pet studies: many challenges and few oppor-

tunities," *Journal of Cerebral Blood Flow & Metabolism*, vol. 31, no. 10, pp. 1986–1998, 2011.

[225] Y. Choi, S.-C. Huang, R. A. Hawkins, J. Y. Kim, B.-T. Kim, C. K. Hoh, K. Chen, M. E. Phelps, and H. R. Schelbert, "Quantification of myocardial blood flow using 13n-ammonia and pet: comparison of tracer models," *J NucI Med*, vol. 40, pp. 1045–1055, 1999.

[226] R. E. Carson, V. Cunningham, R. N. Gunn, H. Iida, G. M. Knudsen, R. A. Koeppe, K. Koshino, A. A. Lammertsma, K. L. Leenders, P. Maguire, W. Muller-Schauenburg, A. Sohlberg, C. Svarer, and H. Watabe, "Pet pharmacokinetic course manual," *International Society of Cerebral Blood Flow and Metabolism*, 2007.

[227] J. J. Leader, *Numerical analysis and scientific computation*. Pearson Addison Wesley Boston, 2004.

[228] W. P. Segars, D. S. Lalush, and B. M. Tsui, "A realistic spline-based dynamic heart phantom," *Nuclear Science, IEEE Transactions on*, vol. 46, no. 3, pp. 503–506, 1999.

[229] J. Tang, A. Rahmim, R. Lautamäki, M. A. Lodge, F. M. Bengel, and B. M. Tsui, "Optimization of rb-82 pet acquisition and reconstruction protocols for myocardial perfusion defect detection," *Physics in medicine and biology*, vol. 54, no. 10, p. 3161, 2009.

[230] J. Fessler *et al.*, "Image reconstruction toolbox," *Available at website: http://www. eecs. umich. edu/fessler/code*, 2012.

[231] K.-H. Su, T.-C. Yen, and Y.-H. D. Fang, "A novel approach for direct reconstruction of parametric images for myocardial blood flow from pet imaging," *Medical physics*, vol. 40, no. 10, p. 102505, 2013.

[232] C. Meyer, D.-N. Peligrad, and M. Weibrecht, "Assessment of input function distortions on kinetic model parameters in simulated dynamic ^{82}rb pet perfusion studies," *Nuclear Instruments and Methods in Physics Research Section A: Accelerators, Spectrometers, Detectors and Associated Equipment*, vol. 571, no. 1, pp. 199–202, 2007.

[233] A. K. Tahari, A. Lee, M. Rajaram, K. Fukushima, M. A. Lodge, B. C. Lee, E. P. Ficaro, S. Nekolla, R. Klein, R. L. Wahl *et al.*, "Absolute myocardial flow quantification with 82rb pet/ct: comparison of different software packages and methods," *European journal of nuclear medicine and molecular imaging*, vol. 41, no. 1, pp. 126–135, 2014.

[234] S. J. Cullom, J. A. Case, S. A. Courter, A. I. McGhie, and T. M. Bateman, "Regadenoson pharmacologic rubidium-82 pet: A comparison of quantitative perfusion and function to dipyridamole," *Journal of Nuclear Cardiology*, vol. 20, no. 1, pp. 76–83, 2013.

[235] M. Slifstein and M. Laruelle, "Effects of statistical noise on graphic analysis of

pet neuroreceptor studies," *Journal of Nuclear Medicine*, vol. 41, no. 12, pp. 2083–2088, 2000.

[236] F. Lindsten, H. Ohlsson, and L. Ljung, "Just relax and come clustering!: A convexification of k-means clustering," *Technical report from Automatic Control at Linkpings universitet*, 2011.

[237] T. D. Hocking, A. Joulin, F. Bach, J.-P. Vert *et al.*, "Clusterpath an algorithm for clustering using convex fusion penalties," in *28th international conference on machine learning*, 2011.

[238] E. C. Chi and K. Lange, "Splitting methods for convex clustering," *arXiv preprint arXiv:1304.0499*, 2013.

[239] L. Lu, N. A. Karakatsanis, J. Tang, W. Chen, and A. Rahmim, "3.5 d dynamic pet image reconstruction incorporating kinetics-based clusters," *Physics in medicine and biology*, vol. 57, no. 15, p. 5035, 2012.

[240] H. Akaike, "A new look at the statistical model identification," *Automatic Control, IEEE Transactions on*, vol. 19, no. 6, pp. 716–723, 1974.

[241] D. Pelleg, A. W. Moore *et al.*, "X-means: Extending k-means with efficient estimation of the number of clusters." in *ICML*, 2000, pp. 727–734.

[242] J. Wang, "Consistent selection of the number of clusters via crossvalidation," *Biometrika*, vol. 97, no. 4, pp. 893–904, 2010.

[243] S. Tatiraju and A. Mehta, "Image segmentation using k-means clustering, em and normalized cuts," *Department of EECS*, pp. 1–7, 2008.

[244] S. Mouysset, H. Zbib, S. Stute, J. Girault, J. Charara, J. Noailles, S. Chalon, I. Buvat, and C. Tauber, "Segmentation of dynamic pet images with kinetic spectral clustering," *Physics in medicine and biology*, vol. 58, no. 19, p. 6931, 2013.

[245] H.-M. Wu, C. K. Hoh, Y. Choi, H. R. Schelbert, R. A. Hawkins, M. E. Phelps, and S.-C. Huang, "Factor analysis for extraction of blood time-activity curves in dynamic fdg-pet studies." *Journal of nuclear medicine: official publication, Society of Nuclear Medicine*, vol. 36, no. 9, pp. 1714–1722, 1995.

[246] J.-H. Ahn, S. Kim, J.-H. Oh, and S. Choi, "Multiple nonnegative-matrix factorization of dynamic pet images," in *Proceedings of Asian Conference on Computer Vision*, 2004, pp. 1009–1013.

[247] M. Samal, M. Karny, H. Surova, P. Penicka, E. Marikova, and Z. Dienstbier, "On the existence of an unambiguous solution in factor analysis of dynamic studies," *Physics in medicine and biology*, vol. 34, no. 2, p. 223, 1989.

[248] D. Donoho and V. Stodden, "When does non-negative matrix factorization give a correct decomposition into parts?" in *Advances in neural information processing systems*, 2003, p. None.

[249] J. S. Lee, D. S. Lee, S. Choi, and K. S. Park, "Non-negative matrix factorization of dynamic images in nuclear medicine," in *Nuclear Science Symposium Conference Record, 2001 IEEE*, vol. 4. IEEE, 2001, pp. 2027–2030.

[250] L. Le Meunier, P. J. Slomka, D. Dey, A. Ramesh, L. E. Thomson, S. W. Hayes, J. D. Friedman, V. Cheng, G. Germano, and D. S. Berman, "Enhanced definition pet for cardiac imaging," *Journal of Nuclear Cardiology*, vol. 17, no. 3, pp. 414–426, 2010.

[251] ——, "Motion frozen 18f-fdg cardiac pet," *Journal of Nuclear Cardiology*, vol. 18, no. 2, pp. 259–266, 2011.

[252] A. Rahmim, J. Tang, and H. Zaidi, "Four-dimensional image reconstruction strategies in cardiac-gated and respiratory-gated pet imaging," *PET Clinics*, vol. 8, no. 1, pp. 51–67, 2013.

[253] A. Rahmim, J. Tang, M. Ay, and F. Bengel, "4d respiratory motion-corrected rb-82 myocardial perfusion pet image reconstruction," in *Nuclear Science Symposium Conference Record (NSS/MIC), 2010 IEEE*. IEEE, 2010, pp. 3312–3316.

[254] K. Erlandsson, I. Buvat, P. H. Pretorius, B. A. Thomas, and B. F. Hutton, "A review of partial volume correction techniques for emission tomography and their applications in neurology, cardiology and oncology," *Physics in medicine and biology*, vol. 57, no. 21, p. R119, 2012.

[255] Y. Rakvongthai, J. Ouyang, B. Guerin, Q. Li, N. M. Alpert, and G. El Fakhri, "Direct reconstruction of cardiac pet kinetic parametric images using a preconditioned conjugate gradient approach," *Medical physics*, vol. 40, no. 10, p. 102501, 2013.

[256] A. Rahmim, J. Tang, and H. Mohy-ud Din, "Direct 4d parametric imaging in dynamic myocardial perfusion pet," *Frontiers in Biomedical Technologies*, vol. 1, no. 1, pp. 4–13, 2014.

[257] W. E. Klunk, H. Engler, A. Nordberg, Y. Wang, G. Blomqvist, D. P. Holt, M. Bergström, I. Savitcheva, G.-F. Huang, S. Estrada *et al.*, "Imaging brain amyloid in alzheimer's disease with pittsburgh compound-b," *Annals of neurology*, vol. 55, no. 3, pp. 306–319, 2004.

[258] A. Nordberg, J. O. Rinne, A. Kadir, and B. Långström, "The use of pet in alzheimer disease," *Nature Reviews Neurology*, vol. 6, no. 2, pp. 78–87, 2010.

[259] P. T. Meyer, S. Hellwig, F. Amtage, C. Rottenburger, U. Sahm, P. Reuland, W. A. Weber, and M. Hüll, "Dual-biomarker imaging of regional cerebral amyloid load and neuronal activity in dementia with pet and 11c-labeled pittsburgh compound b," *Journal of Nuclear Medicine*, vol. 52, no. 3, pp. 393–400, 2011.

[260] J. Sojkova, J. Goh, B. Landman, X. Yang, Y. Zhou, Y. An, L. L. Beason-Held, M. A. Kraut, D. F. Wong, and S. M. Resnick, "Voxel-wise investigation of cerebral blood flow and distribution volume ratio (dvr) maps: Contribution

of blood flow to dvr, a measure of β-amyloid deposition," *Bayview Research Symposium*, 2011.

[261] D. Silverman, *PET in the Evaluation of Alzheimer's Disease and Related Disorders*. Springer, 2009.

[262] J. Sojkova, L. Beason-Held, Y. Zhou, Y. An, M. A. Kraut, W. Ye, L. Ferrucci, C. A. Mathis, W. E. Klunk, D. F. Wong *et al.*, "Longitudinal cerebral blood flow and amyloid deposition: an emerging pattern?" *Journal of Nuclear Medicine*, vol. 49, no. 9, pp. 1465–1471, 2008.

[263] Y. Zhou, C. J. Endres, J. R. Brašić, S.-C. Huang, and D. F. Wong, "Linear regression with spatial constraint to generate parametric images of ligand-receptor dynamic pet studies with a simplified reference tissue model," *Neuroimage*, vol. 18, no. 4, pp. 975–989, 2003.

[264] G. Wang and J. Qi, "Direct estimation of kinetic parametric images for dynamic pet," *Theranostics*, vol. 3, no. 10, p. 802, 2013.

[265] M. Conti, "Why is tof pet reconstruction a more robust method in the presence of inconsistent data?" *Physics in medicine and biology*, vol. 56, no. 1, p. 155, 2011.

Biographical Sketch

Hassan Mohy-ud-Din was born and raised in Lahore, Pakistan. He earned a BS in Electronics Engineering from Ghulam Ishaq Khan Institute of Engineering Sciences and Technology in June 2006. He pursued a career in teaching, serving as Lecturer at the University of Engineering and Technology Lahore ($2006 - 08$) and Development Engineer at the School of Science and Engineering, LUMS ($2008 - 09$).

Hassan joined the Department of Electrical and Computer Engineering (ECE), Johns Hopkins University in 2009 on an ECE fellowship to read for a PhD degree. His expected graduation is in February 2015. He also completed an MA (thesis) in Applied Mathematics and Statistics (2014) and an MSE in Electrical and Computer Engineering (2012). His research lies at the intersection of applied mathematics and medical imaging. His research work has won the 2014 Bradley-Alavi fellowship from SNMMI and 2014 SIAM Student Travel Award. He has presented his work at various conferences and universities and carries a teaching experience of over 9 years. He has also made academic trips to Canada, France, and Hong Kong.

Post PhD, Hassan is expected to join Yale University to pursue his postdoctoral studies.

Research Publications

- **Hassan Mohy-ud-Din**, Martin A. Lodge, and Arman Rahmim, "Quantitative Myocardial Perfusion PET Parametric Imaging at the Voxel-level", submitted to Physics in Medicine and Biology, 2015.

- **Hassan Mohy-ud-Din**, Martin A. Lodge, and Arman Rahmim, "Quantitative myocardial perfusion PET parametric imaging at the voxel-level", submitted to the Society of Nuclear Medicine Annual Meeting Abstracts, 2015.

- **Hassan Mohy-ud-Din**, Nicolas A. Karakatsanis, William Willis, Dean F. Wong, and Arman Rahmim, "Intra-frame Motion Compensation in Multi-frame Brain PET Imaging", submitted to the Frontiers in Biomedical Technologies, 2015.

- Arman Rahmim, **Hassan Mohy-ud-Din**, and Thomas Schindler, "Base-to-apex gradient abnormality detection task performance in myocardial perfusion PET imaging", Society of Nuclear Medicine Annual Meeting Abstracts, Vol. 55, No. Supplement 1, 2014.

- Saeed Ashrafinia, **Hassan Mohy-ud-Din**, Nikolaos Karakatsanis, Dan Kadrmas, and Arman Rahmim. "Enhanced quantitative PET imaging utilizing adaptive partial

resolution modeling", Society of Nuclear Medicine Annual Meeting Abstracts, Vol. 55, No. Supplement 1, 2014.

- Arman Rahmim, Jing Tang, and **Hassan Mohy-ud-Din**. "Direct 4-D parametric imaging in dynamic myocardial perfusion PET", Frontiers in Biomedical Technologies, Vol. 1, No. Supplement 1, 2014.

- Saeed Ashrafinia, Nicolas Karakatsanis, **Hassan Mohy-ud-Din**, and Arman Rahmim. "Towards continualized task-based resolution modeling in PET imaging", SPIE Medical Imaging, International Society for Optics and Photonics, 2014.

- **Hassan Mohy-ud-Din**, Nikolaos A. Karakatsanis, Martin A. Lodge, Jing Tang, and Arman Rahmim. "Parametric myocardial perfusion PET imaging using physiological clustering", SPIE Medical Imaging, International Society for Optics and Photonics, 2014.

- **Hassan Mohy-ud-Din**, Nikolaos A. Karakatsanis, Jim S. Goddard, Justin Baba, William Wills, Abdel K. Tahari, Dean F. Wong, and Arman Rahmim, "Generalized dynamic PET inter-frame and intra-frame motion correction-Phantom and human validation studies", Nuclear Science Symposium and Medical Imaging Conference, IEEE, 2012.

- **Hassan Mohy-ud-Din**, Nicolas A. Karakatsanis, Julie C. Price, Yun Zhou, Susan M. Resnick, Christopher J. Endres, William E. Klunk, Chester A. Mathis, Dean F. Wong, and Arman Rahmim, "Investigation of noise-induced correlations in dual-biomarker parametric imaging from dynamic ^{11}C PiB PET", Journal of Cerebral

Blood Flow and Metabolism, Vol. 32, Nature publishing group, 2012.

- Christopher J. Endres, Yun Zhou, **Hassan Mohy-Ud-Din**, and Arman Rahmim, "PETmodel: an SPM toolkit for parametric imaging of dynamic PET data", Journal of Cerebral Blood Flow and Metabolism, Vol. 32, Nature publishing group, 2012.

- Nicolas A. Karakatsanis, Martin A. Lodge, **Hassan Mohy-ud-Din**, Abdel K. Tahari, Yun Zhou, Richard L. Wahl, and Arman Rahmim, "Enhanced whole-body PET parametric imaging using hybrid regression and thresholding driven by kinetic correlations", Nuclear Science Symposium and Medical Imaging Conference, IEEE, 2012.

- **Hassan Mohy-ud-Din**, Nikolaos A. Karakatsanis, Mohammad R. Ay, Christopher J. Endres, Dean F. Wong, and Arman Rahmim, "Generalized inter-frame and intra-frame motion correction in PET imaging - A simulation study", Nuclear Science Symposium and Medical Imaging Conference, IEEE, 2011.

- Arman Rahmim, Jing Tang, **Hassan Mohy-ud-Din**, Mohammad R. Ay, and Martin A. Lodge, "Use of optimization transfer for enhanced direct 4-D parametric imaging in myocardial perfusion PET", Society of Nuclear Medicine Annual Meeting Abstracts, Vol. 52, No. Supplement 1, 2011.

- **Hassan Mohy-ud-Din**, Jing Tang, Dean Wong, and Arman Rahmim, "Comparison of ordered subset implementations for EM, preconditioned steepest ascent (PSA) and conjugate gradient (PCG) optimization tasks in PET image reconstruction", Society of Nuclear Medicine Annual Meeting Abstracts, Vol. 52, No. Supplement 1, 2011.